

Time-Frequency Domain Modelling for Ultrasonic
Nondestructive Testing

Katherine M. M. Tant

Department of Mathematics and Statistics

University of Strathclyde

Glasgow, UK

December 9, 2014

This thesis is submitted to the University of Strathclyde for the
degree of Doctor of Philosophy in the Faculty of Science.

This thesis is the result of the authors original research. It has been composed by the author and has not been previously submitted for examination which has led to the award of a degree.

The copyright of this thesis belongs to the author under the terms of the United Kingdom Copyright Acts as qualified by University of Strathclyde Regulation 3.50. Due acknowledgement must always be made of the use of any material contained in, or derived from, this thesis.

Signed:

Date:

Acknowledgements

I am grateful to my supervisor Dr Tony Mulholland for all of the help, support and advice he has provided me with throughout my time here at Strathclyde. It has been a pleasure.

I would also like to thank the staff at the Centre of Ultrasonic Engineering, my second supervisor Dr Matthias Langer, and everyone else in the department of Mathematics and Statistics at the University of Strathclyde. Not least, Laura Cunningham and Craig MacDonald, both of whom can always be counted on to brighten up a hard day.

Finally, I would like to thank my family for their continued support. My grandparents, John and Margaret, my brother, Daniel, my dad, Peter, and my mum, Joyce, all of whom I can rely on for guidance and good advice.

Abstract

This thesis endeavours to develop and implement new and improved methods for the characterisation of defects embedded in steel welds through the analysis of data collected by ultrasonic phased array inspections. A factor common to the existing imaging techniques used for flaw characterisation is the subjective thresholding required to estimate the size of the flaw. The work contained in this thesis uses the mathematics of inverse problems and scattering theory to extract information about such defects and puts forward an objective approach which employs a mathematical model. A relationship between the pulse-echo response curve of a scattering matrix and the size and orientation of a flaw is derived analytically via the Born approximation and results in a completely objective approach to crack sizing. Further expansion of these relationships allows for expressions to be formulated concerning the minimum resolvable crack length and the effects of array pitch and flaw depth on the accuracy of the algorithm. The methodology is then extended and tested on experimental data collected from welded austenitic steel plates containing a lack of fusion crack. In the latter part of this thesis, work focusses on the exploration of the fractional Fourier transform and coded excitations. The fractional Fourier transform allows for retention of both time and frequency domain information simultaneously and permits the in-

homogeneous wave equation (with a forcing function prescribed as a linear chirp modulated by a Gaussian envelope) to be solved in time-frequency space. This in turn facilitates a comparison between a gated continuous wave excitation and a Gaussian modulated linear chirp. It is observed that the Gaussian modulated linear chirp results in a marked increase in the scattering amplitude.

Contents

| | | |
|----------|------------------------------------------------------------------------------------------------------------------------|-----------|
| 1 | Introduction | 1 |
| 1.1 | Background and Motivation | 1 |
| 1.1.1 | Ultrasound | 2 |
| 1.1.2 | Nondestructive Evaluation | 3 |
| 1.1.3 | An Ultrasonic Testing System | 3 |
| 1.1.4 | Detection and Characterisation of Flaws using Ultrasonic Nondestructive Testing | 7 |
| 1.1.5 | The Inverse Scattering Problem | 10 |
| 1.1.6 | The Time-Frequency Domain | 10 |
| 1.1.7 | The Fractional Fourier Transform | 11 |
| 1.1.8 | Coded Excitations | 12 |
| 1.2 | Outline of Thesis | 12 |
| 2 | The Examination and Adaptation of Existing Techniques for the Detection and Imaging of Defects within Welds | 15 |
| 2.1 | Time Domain Methods for the Detection and Imaging of Flaws | 16 |
| 2.1.1 | The Total Focussing Method | 17 |
| 2.2 | Detection and Imaging Techniques in the Time-Frequency Domain | 20 |

| | | |
|---------|---------------------------------------------------------------------------------------------------|----|
| 2.2.1 | Detection in the Frequency Domain | 24 |
| 2.2.1.1 | Application of the Tiling Method to Experimental Data | 28 |
| 2.2.2 | The Factorisation Method | 32 |
| 2.2.2.1 | The Factorisation Method | 34 |
| 2.2.2.2 | The $F_{\#}$ Operator | 38 |
| 2.2.3 | Application of the Factorisation Method | 39 |
| 2.2.3.1 | Application to Data as Modelled by the Born Ap- proximation | 39 |
| 2.2.3.2 | Application of the Factorisation Method to Data as Modelled by Finite Element Simulated Data . | 41 |
| 2.2.3.3 | Application of the Factorisation Method to Exper- imental Data | 43 |
| 2.3 | Subjectivity of Methods | 45 |
| 2.4 | Conclusions | 46 |

**3 A Model Based Approach to Crack Sizing in the Frequency Do-
main** **50**

| | | |
|-------|------------------------------------------------|----|
| 3.1 | Introduction | 50 |
| 3.2 | The Born Approximation | 52 |
| 3.3 | Scattering Matrices | 56 |
| 3.3.1 | Aperture | 58 |
| 3.3.2 | Defect Shape | 59 |
| 3.3.3 | Defect Orientation | 60 |
| 3.3.4 | Distance of Defect from the Array | 63 |
| 3.4 | A Model-Based Crack Sizing Algorithm | 65 |

| | | |
|----------|---------------------------------------------------------------------------------------|------------|
| 3.4.1 | The Zero Degree Crack Case | 68 |
| 3.4.2 | The Effect of Crack Orientation on Crack Sizing | 75 |
| 3.5 | The Error Manifested in the Crack-Sizing Formulae due to the Array Pitch | 77 |
| 3.5.1 | The Zero Degree Crack Case | 79 |
| 3.5.2 | General Crack Orientation | 83 |
| 3.5.3 | Sensitivity | 88 |
| 3.6 | Application of the Model Based Crack Sizing Algorithm to Simulated Data | 92 |
| 3.6.1 | Effects of an Artificially Increasing Array Pitch | 94 |
| 3.6.2 | Effects of an Artificially Decreasing Array Length | 97 |
| 3.7 | Conclusions | 98 |
| 4 | Crack Sizing via Model Based Optimisation for Application to Experimental Data | 101 |
| 4.1 | Introduction | 101 |
| 4.2 | Optimisation Over Crack Length | 103 |
| 4.3 | Development of A Multi-Frequency Optimisation Method | 105 |
| 4.4 | Application to Experimental Data | 108 |
| 4.4.1 | Scattering Submatrices | 108 |
| 4.4.2 | Extending the Multi-Frequency Optimisation over the Scattering Matrix | 112 |
| 4.5 | Conclusions | 116 |
| 5 | Improved Signal to Noise Ratio by Using Chirp Excitations to Illuminate Flaws | 118 |

| | | |
|----------|---------------------------------------------------------------------------------------------------|------------|
| 5.1 | Coded Excitations | 118 |
| 5.2 | The Fractional Fourier Transform | 122 |
| 5.3 | The Wave Equation with Linear Chirp Forcing Function | 127 |
| 5.3.1 | The Homogeneous Solution | 130 |
| 5.3.2 | The Inhomogeneous Solution | 133 |
| 5.3.2.1 | Fractional Fourier Transform of Order $a = -1$ of a Gaussian Modulated Linear Chirp | 135 |
| 5.3.3 | The General Solution | 139 |
| 5.4 | Results | 139 |
| 5.4.1 | Choosing the Optimal Order a | 141 |
| 5.5 | Conclusions | 147 |
| 6 | Conclusions | 151 |
| 6.1 | Introduction | 151 |
| 6.2 | Results | 152 |
| 6.3 | Future Work | 155 |
| 6.4 | Concluding Remarks | 157 |
| A | Derivation of an Explicit Expression for the Scattered Wave via the Born Approximation | 158 |
| B | Finite Element Data as Simulated in the Software Package PZFlex | 165 |
| C | Experimentally Collected Data | 169 |

Chapter 1

Introduction

1.1 Background and Motivation

Many safety critical structures, such as those found in nuclear plants, oil pipelines and in the aerospace industry, rely on key components that are constructed from heterogeneous materials. Ultrasonic nondestructive testing (NDT) uses high frequency acoustic/elastic waves to inspect these parts, ensuring they operate reliably without compromising their integrity. Welds are of particular interest as they are subject to stress and, as with any type of bond, constitute the weak point of the structure. Austenitic steel welds are notoriously difficult to inspect [1, 2]. Due to thermal effects as the weld is forming, a spatially heterogeneous structure is formed by local fluctuations in the crystal orientation. This complex internal geometry is highly scattering and leads to the obscuration of defects. Recently, ultrasonic transducer arrays have been introduced to help address the issue [3, 4]. These arrays are an arrangement of small elements, each capable of firing and receiving ultrasound waves simultaneously. The potential of this technology will

only be fully realised when mathematical algorithms are developed to decipher the copious amounts of data produced by these devices.

1.1.1 Ultrasound

Ultrasound can be defined as an oscillating acoustic pressure wave with a frequency above 20kHz; the approximate upper boundary of the human hearing range. Animals and insects, who have the ability to hear ultrasound, use it to navigate and locate prey and/or predators [5, 6, 7]. This technique can be mimicked using ultrasonic transducers to transmit and then listen to ultrasound waves propagating through a medium, allowing the user of the transducer to measure distances and detect obstacles within an object without having to penetrate the surface. One widely known application is in obstetric sonography [8], where it is used to monitor the development and growth of foetuses. It has further applications throughout medical imaging, where it can be employed as a diagnostic tool [9, 10], allowing for visualisation of internal organs. These practices have been commonplace since the mid 20th century due to the low cost and portability of equipment. An even earlier application of ultrasound is in SONAR. The first recording of underwater echo location can be traced back to Leonardo Da Vinci in 1490, when he observed that objects could be detected underwater by placing one end of a tube in the water and the other end to your ear [11]. However, it wasn't until the sinking of the Titanic in 1912 that research into SONAR as we know today was prompted [12]. Its importance was then reinforced by the outbreak of World War One and the need to detect enemy submarines.

1.1.2 Nondestructive Evaluation

Nondestructive testing (NDT) is an umbrella term for a wide and varied group of analysis techniques used to evaluate and characterise materials and components non-invasively. These techniques include liquid penetrant testing [13], electromagnetic testing [14, 15], x-ray computed tomography (CT scan) [16] and infrared and thermal testing [17], amongst others. They are employed to detect defects, take thickness measurements and characterise the internal geometry of materials. Important applications include evaluating the integrity of wind turbine blades [18], pressure vessels [19], pipelines [20] and engine parts [21]. Some of the advantages and limitations of these techniques are listed in Table 1.1. Other considerations to be made are listed in Table 1.2, which displays the relative success of each technique in meeting the desirable criteria. Ultrasonic nondestructive testing (NDT) uses high frequency mechanical waves to inspect components, ensuring they operate reliably without compromising their integrity. It has grown in popularity within the NDT industry in recent years due to the relatively inexpensive and portable equipment it requires, and its potential for automation and real-time results (see Tables 1.1 and 1.2). However, difficulties can arise when the medium under inspection is of a highly heterogeneous nature and causes scattering of the ultrasound wave. Other physical processes such as mode conversion, transmission losses and material attenuation can also cause wave distortion and subsequently lead to the obscuration of defects.

1.1.3 An Ultrasonic Testing System

An ultrasonic testing (UT) system is constructed from several units. Figure 1.1 depicts a basic schematic of the experimental set up. A pulser produces a high

| Technique | Advantages | Limitations |
|--------------------------|-------------------------------------------------------------------|----------------------------------------------------------------------------------------|
| Ultrasonic Testing | Can penetrate thick samples. Immediate results. Can be automated. | Usually requires coupling. Highly dependent on media under inspection. |
| Liquid Penetrant Testing | Inexpensive. Easy to use. | Flaw must be open to the surface. Not suitable for porous materials or rough surfaces. |
| X-Ray | Suitable for inspection of a wide range of materials | Expensive. Radiation requires safety precautions. |
| Electromagnetic Testing | Readily automated | Limited to electrically conductive media |
| Thermal Imaging | Safe. Non-contact. | Poor resolution on thick sections. Composite materials have low thermal conductivity. |

Table 1.1: The main advantages and limitations of different NDT techniques.

| Technique | Capital Cost | Consumable Cost | Portability of Equipment | Time of Results | Dependent on Material Composition | Ability to Automate | Type of Defect |
|------------------------------|--------------|-----------------|--------------------------|-----------------|-----------------------------------|---------------------|----------------------|
| Ultrasonic Testing | Medium | Very low | High | Instant | Very | Good | Internal |
| Liquid Penetrant Testing | Low | Medium | High | Short delay | Little | Fair | Surface breaking |
| X-Ray | High | High | Low | Delayed | Quite | Fair | Most |
| Electromagnetic Testing | Medium | Low | High | Instant | Very | Good | External |
| Infrared and Thermal Testing | High | Low | High | Instant | Very | Good | Shallow, sub-surface |

Table 1.2: Comparison of different NDT considerations for different techniques.

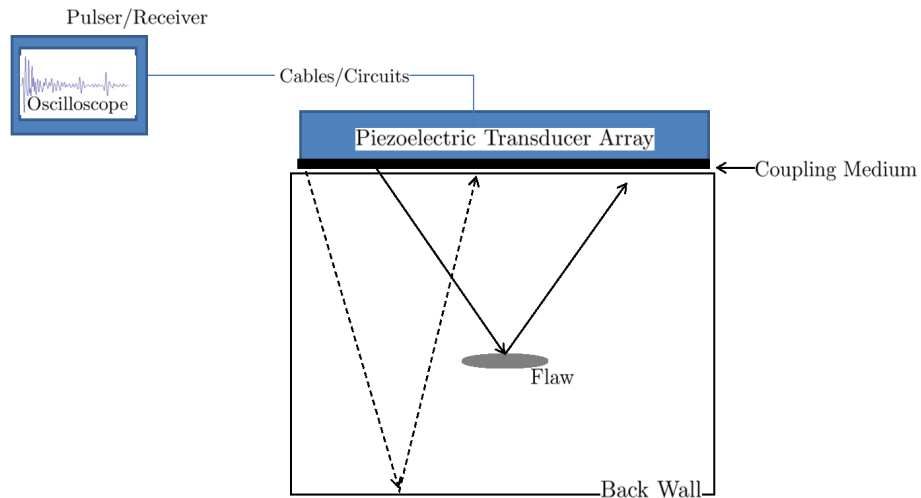


Figure 1.1: An ultrasonic testing set up. The pulser receiver sends an electrical pulse to the phased array transducer which in turn converts it into a mechanical wave. This wave propagates through the medium to be inspected and is reflected back when it comes in contact with an interface. The received wave is converted back into an electrical signal and can be displayed on an oscilloscope.

voltage electrical pulse which is in turn converted into high frequency ultrasound by a piezoelectric transducer. The transducer is usually paired with some sort of acoustic coupling medium, such as water (immersion testing) or gels with high acoustic impedance properties, minimising the inefficiency caused by the wave travelling through air. The ultrasound then propagates through the medium to be inspected and the waves are reflected back when they come into contact with an interface, for example a flaw or the back wall of the object. The reflected wave is then converted back into an electrical signal by the transducer which can then be displayed on an oscilloscope. Piezoelectric crystals have the ability to convert electrical signals into mechanical energy and back again [22, 23], allowing the transducer to act as both a transmitter and receiver. This is known as a pulse-echo set up. Alternatively, two transducers can be employed (one to transmit and one to receive), either at opposite ends of the component (through-transmission

set up) or along the same edge of the component (pitch-catch set up). The production and implementation of phased array transducers which are capable of simultaneously transmitting and receiving ultrasound signals, has surged in the last ten years [3]. These multi-element transducers allow for greater coverage (hence faster inspection times) and provide the possibility of performing inspections with ultrasonic beams of various angles and focal lengths, giving rise to a richer set of data. The N^2 time traces arising from each transmit/receive pair of elements (N being the number of elements, usually between 64 and 256) can be processed and stored in a 3D matrix, usually termed the Full Matrix Capture (FMC) [24].

1.1.4 Detection and Characterisation of Flaws using Ultrasonic Nondestructive Testing

Within the field of ultrasonic nondestructive testing, considerable effort has been expended in exploiting the FMC data captured by phased array inspections, in hopes of improving the methods currently used for the detection and characterisation of defects. The current industry benchmark for interpreting the FMC is the Total Focussing Method (TFM), a delay and sum imaging technique where the area of inspection is discretised into a grid and the signals from every transmit/receive pair are subsequently focussed at each pixel and summed [24, 25, 26]. In its most basic form, the TFM can struggle with the detection and characterisation of flaws embedded in highly heterogeneous media. However, researchers at the University of Bristol have made efforts to improve the algorithm so as it can handle such environments. Modifications include the implementation of frequency filtering, the incorporation of the directional dependence of the ultrasonic velocity

(caused by anisotropy) [27], and the consideration of multiple wave modes [28]. In a similar vein, coherent interferometry (CINT) is another imaging technique, first introduced by Borcea et al [29, 30, 31, 32, 33], which produces statistically stable images of flaws within the highly heterogeneous environments in which the TFM struggles. It involves the correlation of back propagated waves in conjunction with application of the TFM algorithm (often referred to as Kirchhoff Migration when applied in the geophysical context in which CINT was developed). However, due to its basis in multiple local cross correlations, the method is computationally expensive and hence not in line with the real time imaging goals of the NDT industry. Another imaging algorithm, first introduced in [34], is Phase Coherence Imaging (PCI), a method developed for grating and side lobe suppression, artefacts inherent to time of flight imaging methods. PCI uses the phase coherent factor and the sign coherent factor to weight the coherent sum output and correct the image. It is shown in [35] that although PCI improves signal to noise ratio (SNR) levels, it is a less robust algorithm than the TFM when tested over a wide range of flaws. An alternative approach to improving SNR levels can be found within the mathematical community, where the inverse problem of shape reconstruction has received large amounts of attention in recent decades. Sampling methods such as the Factorisation Method [36], the Linear Sampling Method [37], the Probe Method [38] and the Singular Sources Method [39] have yet to become common practice within the NDT industry but do offer a more precise approach to the imaging of flaws. Outside of imaging, a different perspective to the characterisation of crack like scatterers is taken by Zhang et al in [40, 41], where the empirical analysis of scattering matrices allows for an objective crack size estimation. It is shown that there exists a relationship between the crack length and

the half-width, half-maximum (HWHM) of the pulse-echo response (the diagonal of the frequency domain scattering matrix). However, the method relies on the experimental data exhibiting a high signal to noise ratio and hence is not of use when the sample under inspection is of a heterogeneous nature.

Image correction is another area of interest within the ultrasonic NDT community and can be achieved with the inclusion of the directional dependence of the ultrasonic velocity due to anisotropy [42]. To do so, the internal geometry of the sample under inspection must be known *a priori*. Spatially resolved acoustic spectroscopy (SRAS) is a laser ultrasonic technique developed at the University of Nottingham [43, 44] which, when coupled with a numerical surface acoustic wave (SAW) velocity model, can determine the crystal orientation of the material under inspection. Although it can be argued that the method is not strictly non-destructive (the material under inspection must be highly polished), the technique provides a useful insight to the internal geometry of a sample, thus allowing for improved image correction. Similar information can also be extracted via electron backscatter diffraction (EBSD) [45]. An alternative, entirely nondestructive approach can be taken in the form of ray tracing, where the wave path in a medium with varying local wave velocities is calculated using local derivatives to correct the wave direction. Ray tracing can be used as part of an inversion methodology to deduce the anisotropic characteristics from measured time of flight data. It has recently been combined with path finding algorithms (such as Dijkstra's algorithm and the A* algorithm [46, 47]) to reduce computational cost.

1.1.5 The Inverse Scattering Problem

This thesis aims to contribute towards improved characterisation of defects embedded in heterogeneous media via the application of mathematical modelling and analysis. Synonymous with the reconstruction of defects from collected experimental data is the mathematical concept of an inverse problem [48, 49]. The inverse scattering problem is concerned with using measured observations, u^s , to reconstruct an object D [50, 51, 52, 53]. In the context of ultrasonic nondestructive testing, a rich experimental dataset is collected by the ultrasonic phased array transducer and the objective is to discover what gave rise to the received signals via analysis and signal processing. Although inverse scattering problems are the subject of much current activity, the development of a solid mathematical basis has been hampered by the ill-posedness of the problem [54]. In the case of well posed problems, it is known that a unique solution exists for which the solution depends continuously on the data and parameters from which it arises. Typically, in inverse problems, measured data fails to be exact and the smallest of errors in the collected data can give rise to much larger errors in the solution, thus violating the conditions of well-posedness. Hence, an exact solution to the inverse scattering problem does not exist and an approximate solution to the stabilized problem must be sought instead [55]. This can be done via regularisation techniques which usually involve the inclusion of additional information or assumptions.

1.1.6 The Time-Frequency Domain

In an ideal case, a received ultrasound signal should exhibit signs of scattering at the time interval pertaining to the location of the flaw, allowing for detection and subsequent characterisation. However, in practice, scattering by the

microstructure of the host media can dominate the signal. It is difficult to distinguish whether a delay in the time of flight has been caused by a heterogeneity or a defect. To improve distinction between the two it is suggested that the scattered signals are analysed by their frequency content [56, 57]; the sound of a flaw should be different from the sound of a heterogeneity. However, the time information must be retained in order to locate the flaw. This can be achieved via (a) the time windowed Fourier transform [58], where the discrete Fourier transform is applied to short time intervals allowing for the frequency content at that specific time to be analysed independently of the rest of the signal, or (b) the fractional Fourier transform [59], which enables continuous movement between the time and frequency domains, allowing the retention of both frequency and time domain information.

1.1.7 The Fractional Fourier Transform

The theory of fractional powers of the Fourier transform was originally presented by V. Namias in 1980 [60], and later given a rigorous mathematical framework by McBride and Kerr in [61, 62]. The analysis and applications of the fractional Fourier transform (FrFT) have since been developed and it has now become a standard concept within the areas of signal processing and optics [59, 63]. As a generalisation of the ordinary Fourier transform, the FrFT is more flexible in its applications and hence of potential interest to any area in which the Fourier transform is frequently implemented.

1.1.8 Coded Excitations

To further enhance detection and characterisation within the time-frequency domain, coded excitations can be introduced. The use of coded excitations in signal processing has been shown to improve signal to noise ratio (SNR) and lessen trade-offs between sample penetration and image resolution [64, 65]. One example of coded excitation is the chirp, often referred to as linear frequency modulation. Chirps have previously been applied in the fields of medical imaging [66], sonar [67, 68] and radar [69, 70], however, it is only recently that they have gained wide recognition in the NDT industry as a method of delivering a large amount of energy using a relatively low acoustic pressure amplitude [71, 72]. Additionally, due to the multi-frequency nature of a chirp, the wavelength resonant with the defect size is more likely to be included in the transmitted signal, thus causing stronger vibrations and facilitating detection. As a change of frequency in time is inherent to the nature of chirps, use of the FrFT is a complementary choice for the analytical study of these coded excitations [73, 74, 75, 76].

1.2 Outline of Thesis

The overall aim of this thesis is to develop new methods for the improved characterisation of defects embedded in steel welds. To do so, it begins with the examination and implementation of existing detection and characterisation techniques, taken from both within and outwith the ultrasonic nondestructive testing industry. A common feature of these algorithms is the need for a subjective choice of dynamic threshold at which to estimate the defect size, the consequence being varying flaw characterisations. Thus the need for objective defect sizing was re-

alised. Steps to achieving this are developed in Chapters 3 and 4 where the Born approximation is used to formulate an explicit expression for the length of a crack given the roots of the pulse-echo response curve, the flaw depth and the wavelength. The model is then used as a basis for an optimisation technique in which experimental scattering matrices are compared to a library of scattering matrices generated by the Born approximation. The initial results are promising. The final chapter of this thesis combines the fractional Fourier transform and coded excitations to solve an inhomogeneous wave equation in time-frequency space, subsequently allowing for comparisons to be drawn between the transmission of Gaussian modulated linear chirps and gated continuous waves.

The original work in the thesis is stated below

1. In Chapter 2 a detection method based in the time-frequency domain has been developed based on the visual recognition of flaw scattering profiles. The Factorisation Method is applied to experimental data arising from the phased array inspection of steel welds.
2. Chapter 3 utilises the Born approximation to develop an objective, analytical crack sizing formulation based on the roots of the pulse-echo response curve. It is first developed for the case where a crack lies parallel to the array and is then extended to extract the orientation and size of cracks which do not meet this criteria. As a result of the analytical formulation, conclusions are drawn on the minimum resolvable crack length and the minimum array length required to capture the full scattering profile of the flaw. An analytical expression for the upper error bound is achieved via a Taylor expansion and allows for comment on the effects of array pitch and flaw depth on the accuracy of the algorithm. Finally, these conclusions are strengthened by

application to scattering matrices arising from a finite element simulation of the scattering of an ultrasound wave by a crack.

3. The model based crack sizing approach is further developed in Chapter 4 to allow for application to experimental data. The Objective Sizing Matrix (OSM) is produced by assessing the similarity between the scattering matrices arising from experimentally collected data with those arising from the Born approximation over a range of crack lengths and frequencies. The global minimum of the OSM is taken as the objective estimation of the crack size. This is then improved upon by the adoption of a multi-frequency averaging approach.
4. Chapter 5 examines the benefits of coded excitations via the comparison of a Gaussian modulated linear chirp with a gated continuous wave and the application of the fractional Fourier transform (FrFT). This is achieved by solving the wave equation with a linear chirp forcing function in time-frequency space.

Chapter 2

The Examination and Adaptation of Existing Techniques for the Detection and Imaging of Defects within Welds

Ultrasonic phased array systems have become increasingly popular in the last 10 years as tools for flaw detection and characterisation within the nondestructive testing industry. They provide improved sensitivity and coverage by transmitting and receiving over multiple elements, which, when fired in predefined sequences, can provide increased control of beam directivity [77]. The existence and location of flaws can often be deduced via images generated from the data captured by these arrays [3, 24, 35]. The time domain signals from every transmit-receive pair of elements are captured and stored in a large 3D matrix, usually termed the Full Matrix Capture (FMC) [24]. This chapter is intended as an exploration of existing tech-

niques for the detection and characterisation of flaws via the analysis of the FMC. The algorithms studied below have been taken from both within and outwith the NDT industry, and are based on the decipherment of the scattered acoustic signals captured by linear ultrasonic phased array transducers. The first section explores the advantages and limitations of the Total Focussing Method (TFM). The second section is concerned with algorithms based in the time-frequency domain. Here, it is suggested that the application of time-frequency domain algorithms may be beneficial over those approaches based solely in the time domain; a flaw should give way to a different sound than that produced by heterogeneities allowing for improved distinction between the two. Some novelty is introduced through the development of the Tiling Method in Section 2.2.1, a time-frequency domain detection method based on the visual recognition of defect scattering profiles. Section 2.2.2 delves further into this time-frequency domain with the examination (and subsequent implementation) of the mathematical framework for the Factorisation Method; a sampling method concerned with the inverse problem of shape identification.

2.1 Time Domain Methods for the Detection and Imaging of Flaws

In this section, an existing technique for the processing and analysis of data collected by ultrasonic phased array transducers is examined and implemented. The advantages and limitations of the Total Focussing Method (TFM) [24, 35, 28, 78] are explored and demonstrated and it is shown that although this time domain method proves effective in the locating of flaws, there are limitations to its char-

acterising abilities, most notably when the medium under inspection is of a highly heterogeneous nature.

2.1.1 The Total Focussing Method

The current industry benchmark for interpreting the FMC is the Total Focussing Method (TFM). Although other algorithms (such as Phase Coherence Imaging (PCI) [34]) can yield higher image resolution and signal-to-noise ratio (SNR), the TFM has proved most robust over a range of different flaws [35]. We begin by taking the Hilbert transform of the time domain signals to generate the analytic time traces $F_{s,r}^H(t)$ for each (transmit, receive) pair (s, r) . It must be noted that other frequency filtering techniques can be applied at this point to increase the TFM's imaging abilities within heterogeneous media [27], but for the purposes of this thesis, it will be implemented in its most basic form. The area of inspection is discretised into a grid in the x, z plane (see Figure 2.1). For each point in the grid, the signals from every transmit/receive pair are focussed at that point and summed [24]

$$I(x, z) = \left| \sum_{s,r=1}^N F_{s,r}^H \left(\frac{\sqrt{(x_s - x)^2 + z^2} + \sqrt{(x_r - x)^2 + z^2}}{c_1} \right) \right| \quad (2.1)$$

where c_1 is the wave speed in the host material, $(x_i, 0)$ are the coordinates of the array elements which are indexed $i = 1, \dots, N$, (where N is the total number of array elements) and $I(x, z)$ is the intensity of the image at (x, z) . A typical image generated using this technique is shown in Figure 2.2. Here, an ultrasound wave scattered by a 5mm crack lying at an angle of 40° with respect to the x -axis, embedded within a homogeneous medium, has been simulated within the

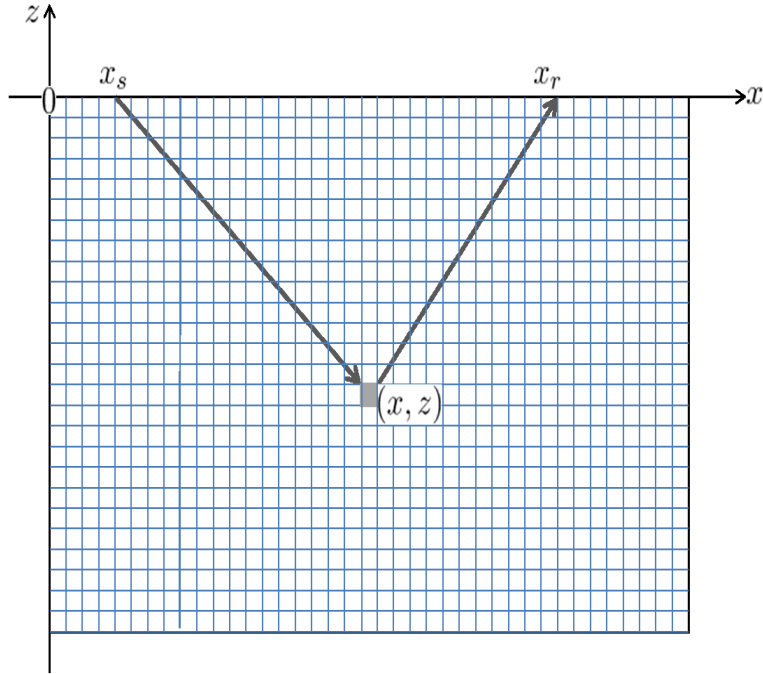


Figure 2.1: Illustration of the TFM imaging domain and the focussing of the signals at a single point.

finite-element package, PZFlex (see Appendix B, Table B.1). Image (a) depicts the full imaging domain whilst image (b) is cropped locally around the flaw to allow closer inspection. Both images have been plotted with a dynamic range of 20dB and the arrow depicts the actual size and location of the crack. A reasonable correspondance between the two can be observed in regards to size and orientation. Note that the side lobes exhibited here are intrinsic to this method of imaging if the scatterer is a line rather than a point - i.e. if the wavelength is roughly equal to or smaller than the size of the crack. Another example of the TFM's imaging abilities is shown in Figure 2.3 where it has been applied to experimental data collected from a stainless steel sample containing a lack of fusion crack of length 6mm and 40° orientation (see Appendix C, Table C.2). The pressure wave speed used has been optimised using the correct placement of the back wall (22mm) as

a guide. Image (a) depicts the full imaging domain, plotted at a dynamic range of 20dB whilst image (b) has been cropped to show the imaging domain local to the flaw. Once again, the TFM has successfully located the crack and provided a basic characterisation. As a measure of the algorithm's success and as a tool for future, quantitative comparisons, the signal-to-noise ratio [79] in decibels (SNR_{dB}) is computed

$$\text{SNR}_{dB} = 20 \log_{10} \frac{A_m}{A_{rms}}, \quad (2.2)$$

where A_m is the peak amplitude at the flaw location and A_{rms} is the root mean square (RMS) amplitude,

$$A_{rms} = \sqrt{\frac{1}{n}(A_1^2 + A_2^2 + \dots + A_n^2)}, \quad (2.3)$$

of n imaging points taken from a selected area of the image which fairly represents the noise arising from the microstructure of the host medium (this area should not include artefacts from the back wall or other flaws). In this case, the RMS amplitude is taken from the area marked by the white box in image (a) and the SNR level is calculated to be approximately 16.8dB.

Although this standard TFM approach can be very successful, factors such as the orientation, location and size of the flaw, along with the heterogeneity of the host medium, can all have detrimental effects in its ability to detect and characterise. Figure 2.4 depicts a TFM image generated by experimental data collected from an austenitic steel weld with a 12mm crack at 90° orientation placed 35mm below a linear array (see Appendix C, Table C.1). Once again, image (a) depicts the full imaging domain (minus the initial near-field backscatter in an attempt to accentuate the flaw and back wall). The actual location of the flaw

lies within the larger box marked on the image. The back wall is reasonably clear and a shadow caused by the diffraction at the crack tip is also visible. In image (b) the area around the crack has been enlarged for a higher definition characterisation and the arrow depicts the actual size and position of the crack. Aside from the location of the crack tip, all other characteristics of the defect are obscured by the heterogeneous microstructure and there is a low SNR level of 13.4dB. Note that for the results discussed above, the ultrasonic longitudinal wave velocity has been estimated with no corrections for anisotropy, however image quality can potentially be enhanced by including these measurements. Assuming the facets of the microstructure are relatively small compared to the wavelength (so that the medium can be considered as homogeneous), this can be measured experimentally via the Back wall Reflection Method (BRM) or the Through Transmission Method (TTM) [27].

2.2 Detection and Imaging Techniques in the Time-Frequency Domain

Time domain imaging algorithms are commonplace tools within the NDT industry and are typically used for both the detection and characterisation of defects. The Total Focussing Method (TFM) [24, 28, 78] is perhaps the most favoured algorithm due to the simplicity of its ‘delay and sum’ formulation and its success in detecting flaws. However, as seen in Section 2.1.1, the method has its limitations, particularly when the medium under inspection is of a highly heterogeneous nature. In the remainder of this chapter, it is suggested that the application of time-frequency domain detection and imaging algorithms may be beneficial over

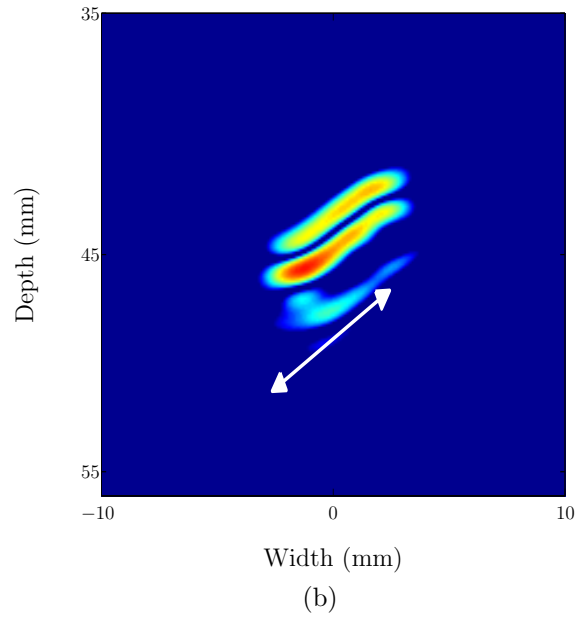
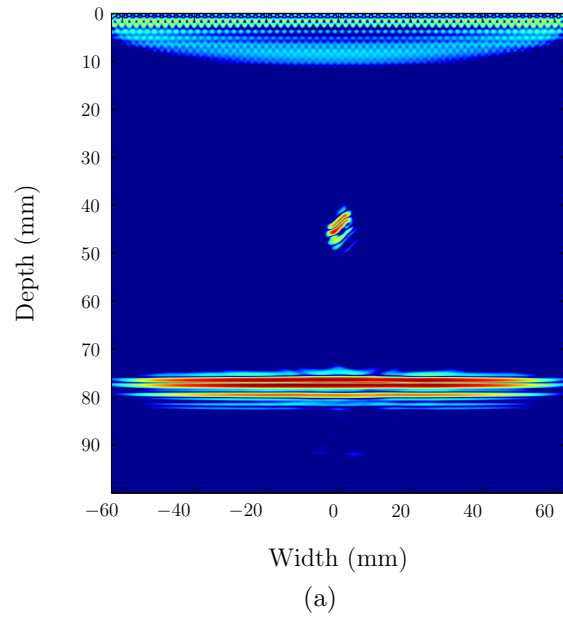
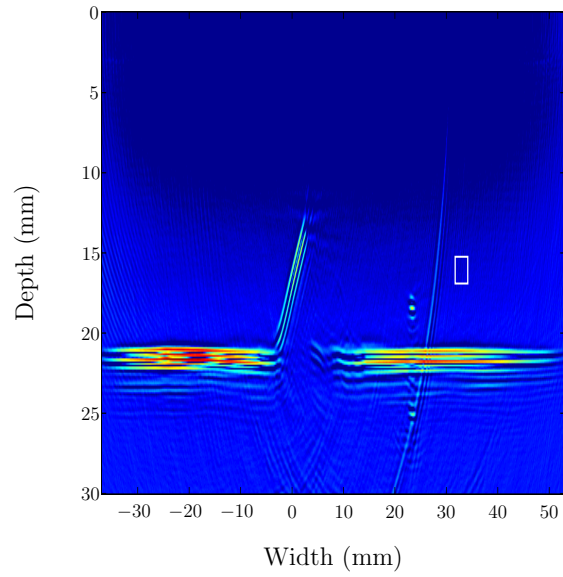
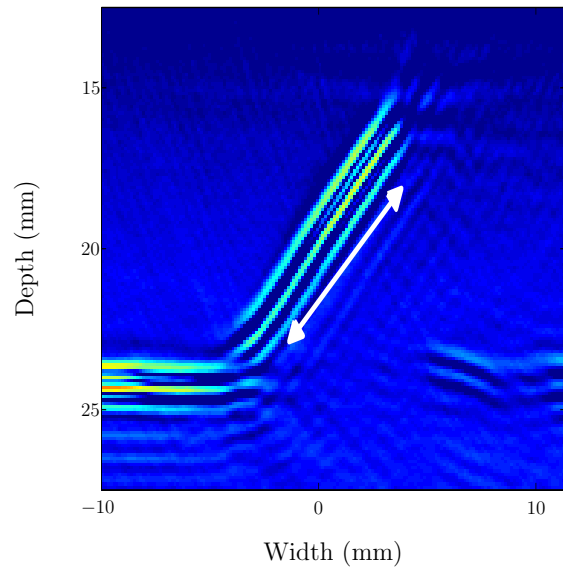


Figure 2.2: TFM image of 5mm crack at 40° orientation, 50mm below the array in a homogeneous medium (see Appendix B, Table B.1). Image (a) depicts the full imaging domain whilst image (b) is cropped locally around the crack for a higher definition characterisation. The arrow depicts the actual size and location of the crack.



(a)



(b)

Figure 2.3: TFM image of 6mm crack at 40° orientation, approximately 15mm below the array in a homogeneous medium (see Appendix C, Table C.2). Image (a) depicts the full imaging domain and the white box marks the area used to calculate signal to noise ratio. Image (b) is of the area local to the crack, allowing for closer inspection of the imaged defect. The arrow depicts the actual size and location of the crack.

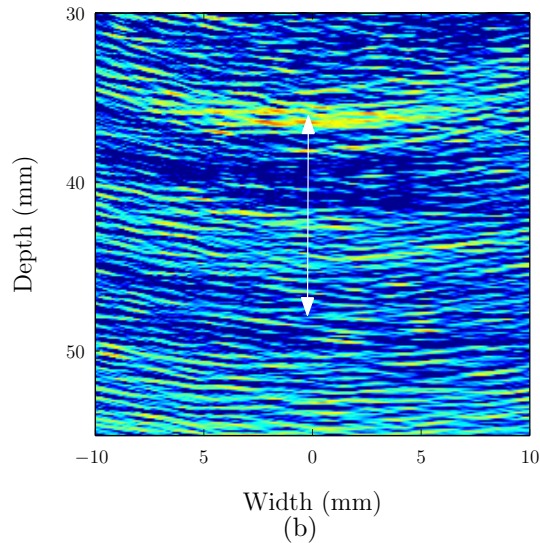
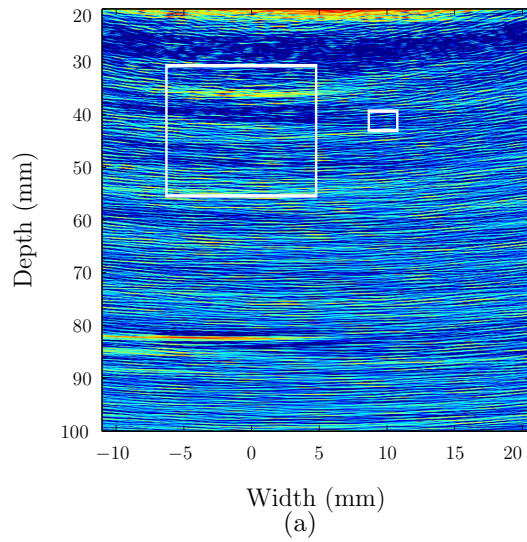


Figure 2.4: TFM image generated by experimental data from an austenitic steel weld with a 12mm crack at 90° orientation placed 35mm below a 45 element linear array (see Appendix C, Table C.1). The initial near-field backscatter has been trimmed to further highlight the flaw and back wall. Image (a) depicts the full imaging domain where the large box signifies the location of the flaw and the smaller box is the area used for the SNR calculation. Image (b) depicts the area local to the crack to allow for closer inspection where the arrow illustrates the actual size and location of the crack. Aside from the location of the crack tip, all other characteristics of the defect are obscured by the heterogeneous microstructure.

those approaches based solely in the time domain. Theoretically, a flaw should give way to a different sound than that produced by heterogeneities, allowing for improved distinction between the two. In Section 2.2.1, the possibility of detecting flaws via time-frequency domain data is examined. Several techniques for the characterisation of flaws in the time-frequency domain have been developed in recent years [36, 80], however, detection in this domain has yet to be explored. Work in Section 2.2.1 focusses on a novel detection method which we will, for the purposes of this chapter, refer to as the Tiling Method. An advantage of this method is that the output is in the form of a frequency domain scattering matrix. Not only does this link directly into our choice of imaging algorithm (see the Factorisation Method in Section 2.2.2) but it expresses the data in a manner which has the potential to be analytically studied through the application of scattering theory via the Born approximation (see Chapter 3). A derivation of the Factorisation Method, which exploits the data contained within the frequency domain scattering matrices, is provided in Section 2.2.2. To further improve the efficacy and applicability of the Factorisation Method in the reconstruction of flaws from data collected by a linear array (hence incorporating a limited angle of inspection), the $F_{\#}$ operator is introduced. The final section presents the results of the method's application to data arising from model based scattering matrices, finite element simulations and experimentally collected data.

2.2.1 Detection in the Frequency Domain

As mentioned above, detection of flaws is typically carried out in the time domain. However, scatterers exhibit their own distinctive scattering profiles in the frequency domain and it seems natural to explore whether these can be used to

indicate the presence of defects. With this in mind, a method which assigns scattering matrices (see Section 3.3) to spatial coordinates has been developed, which we will refer to as the Tiling Method. The Tiling Method begins with the construction of a grid of equally sized tiles over the area to be inspected (see Figure 2.5). The time of flight to the centre point of each tile from every transmit/receive pair of array elements is calculated. These times are then used as midpoints for a time window over each corresponding time trace in the Full Matrix Capture (FMC). The size of this time window is equal to the number of time steps taken to travel the diagonal length of the tile. A discrete Fourier transform over these windows is taken and a scattering matrix (see Section 3.3) is plotted at a specified frequency. The process is repeated for each tile in the spatial domain to build up the tiling shown in Figure 2.6. The results in Figure 2.6 have been produced

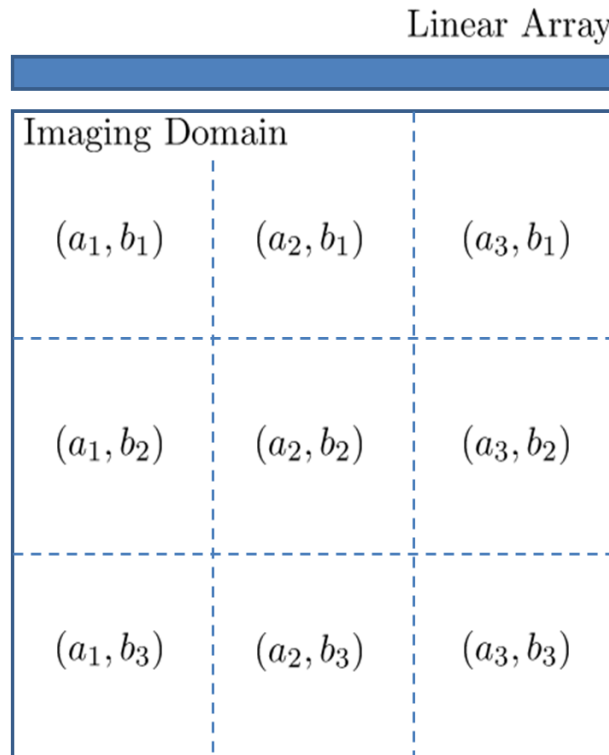


Figure 2.5: A grid is constructed over the vertical plane beneath the linear array.

by applying the algorithm to the data as described in Table B.1 (Appendix B), which has been generated by a finite element simulation of an ultrasound wave probing a homogeneous medium containing a 5mm crack of 0° orientation. The scattering matrices seen are plotted at the centre frequency of the sinusoidal driving function (1.5MHz), however, similar results can be observed over a range of frequencies (1MHz - 5MHz). In this case, square tiles of length 10mm were taken over the entire region, however only the central tiles have been displayed as these contain the interesting features. The central tile bears an obvious resemblance to the scattering matrix of a crack-like scatterer lying parallel to the array as generated by the Born approximation (see Section 3.3). Due to the overlapping of time windows, some remnants of the flaw can also be seen in its neighbouring tiles however, the tile most centred on the flaw should always appear to be the most focussed. Note that the high amplitude corners of the scattering matrices which correspond to tiles at a greater depth from the array, can be attributed to scattering by the back wall. The results in Figure 2.7 have been produced by applying the algorithm to the data as described in Table B.2 (Appendix B), which has also been generated by a finite element simulation, but which now incorporates a heterogeneous microstructure. The scattering matrices in Figure 2.7 are again plotted at the centre frequency of the sinusoidal driving function (1.5MHz). In this case, as the frequency increases, the noise becomes more dominant due to the resonance of the wave with the smaller heterogeneities. Hence, sticking to the lower frequency range of 1 – 2MHz proves beneficial. Again, square tiles of length 10mm were taken over the entire region and only the most central tiles have been displayed. Remnants of the back wall are still apparent in the scattering matrices corresponding to tiles at a greater depth from the array. Due to the heterogeneous

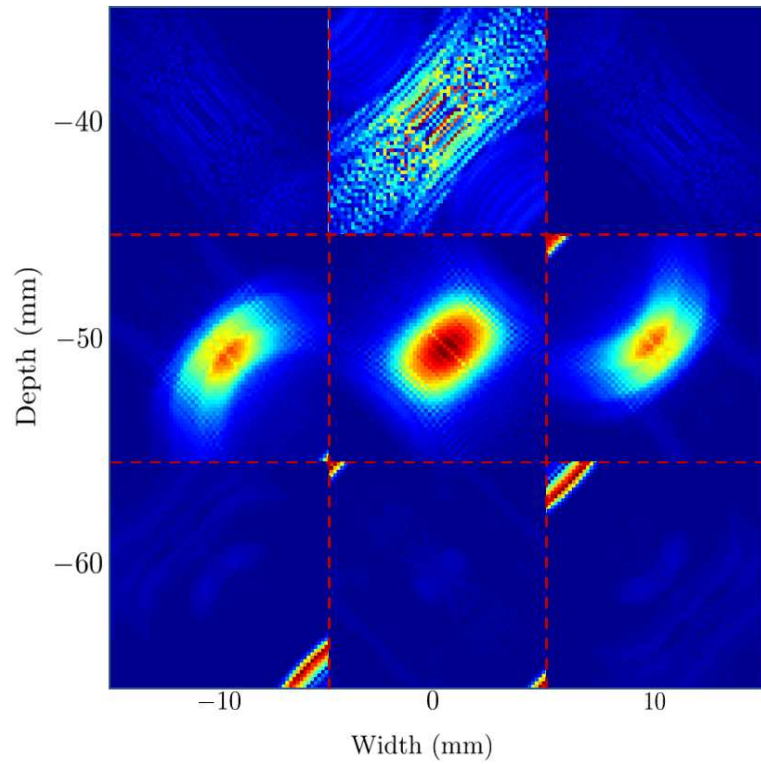


Figure 2.6: Once the grid over the imaging domain has been constructed as in Figure 2.5, it can be filled in with scattering matrices. This tiling has been generated by the data given by Table B.1, Appendix B. The scattering matrices are plotted at 1.5MHz. This example results from taking square tiles of length 10mm.

nature of the medium, a scattering matrix comparable to that as generated by the Born approximation was not anticipated. However, the central tile does exhibit higher amplitudes and more clustering than its neighbouring tiles, suggesting it has detected the crack-like scatterer that lies there.

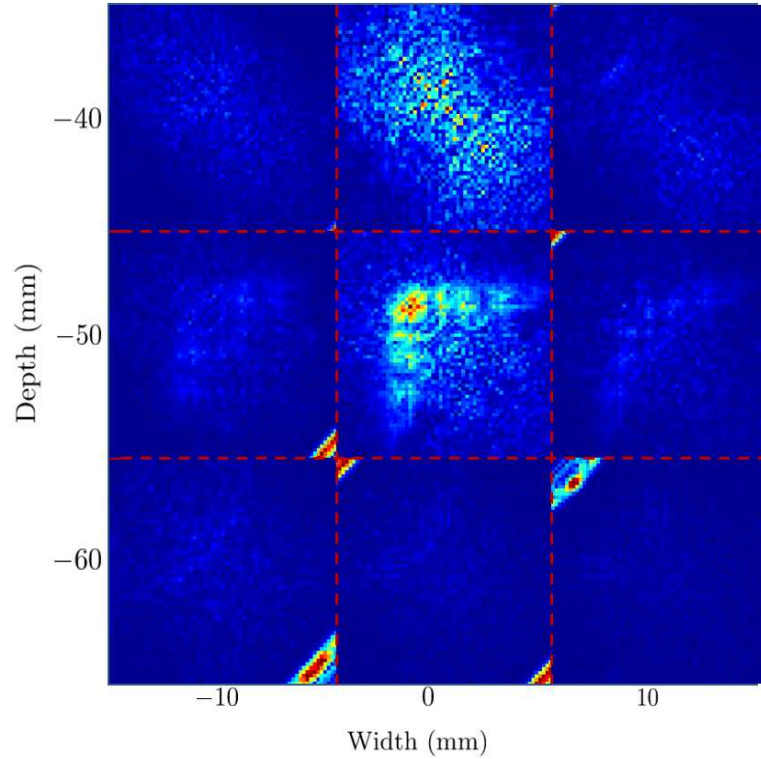


Figure 2.7: Once the grid over the imaging domain has been constructed as in Figure 2.5, it can be filled in with scattering matrices. This tiling has been generated by the data given by Table B.2, Appendix B and the scattering matrices are plotted at 1.5MHz. This example results from taking square tiles of length 10mm.

2.2.1.1 Application of the Tiling Method to Experimental Data

The Tiling Method was developed in the hope of providing an alternative approach to detection, with the potential to improve upon the distinction between defects and facets of a heterogeneous microstructure due to its application within the

time-frequency domain. The above examples have shown that, in simple cases, the location of the flaw can be extracted by visual inspection of the tiled domain. A final assessment of the algorithm’s potential will now be carried out in its application to the data as given by Table C.1. This data has been experimentally collected from a highly heterogeneous sample where a crack lies perpendicular to the array at a depth of 35mm. As seen in Section 2.1.1, the flaw is barely detectable via the TFM and alludes characterisation completely. The results of the application of the Tiling Method can be seen in Figure 2.8. The scattering matrices have been plotted at a frequency of 1MHz in the hope of avoiding excitation of the heterogeneities. The imaging domain covers a 30mm×30mm section of the sample, centred over the known location of the flaw at 35mm depth. As the sample is of 85mm depth, scattering from the back wall is likely to be attenuated by the heterogeneities and hence should not interfere with the flaw scattering. Studying Figure 2.8, high amplitude pulse-echo responses (the main diagonal of the tile) can be observed in the upper three tiles. This can be attributed to the *ring down* of the array elements (where the simultaneous transmission and reception of a wave by an element can interfere with the received signal, see Figure 2.9). The bottom three tiles display no defining features and represent scattering by the microstructure. However, some patterns and high amplitude features start to appear in the central three tiles. Although far from the neat scattering matrices as generated by the data arising from the finite element simulation of scattering within a homogeneous medium (see Figure 2.6), the central tiles do provide an indication of a defect at a depth of 35mm. To further develop the Tiling Method, some effort was made to improve upon the visual recognition technique. Focus turned to the singular values of each matrix. It has been shown that in a weakly scattering media,

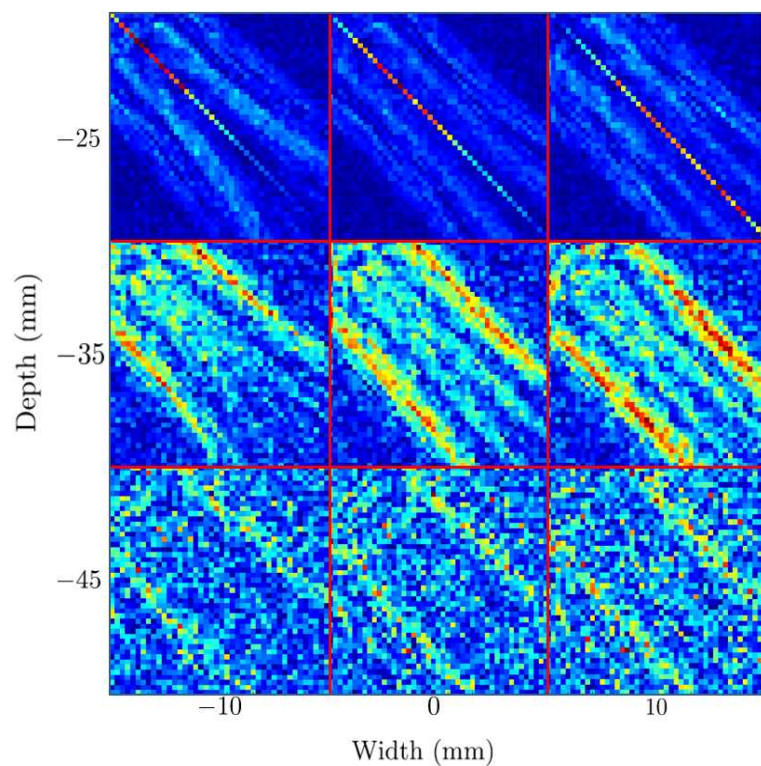


Figure 2.8: This tiling has been generated by the data given by Table C.1, Appendix C. with a tile length of 10mm. The scattering matrices are plotted at 1MHz so as to excite the heterogeneities as little as possible.

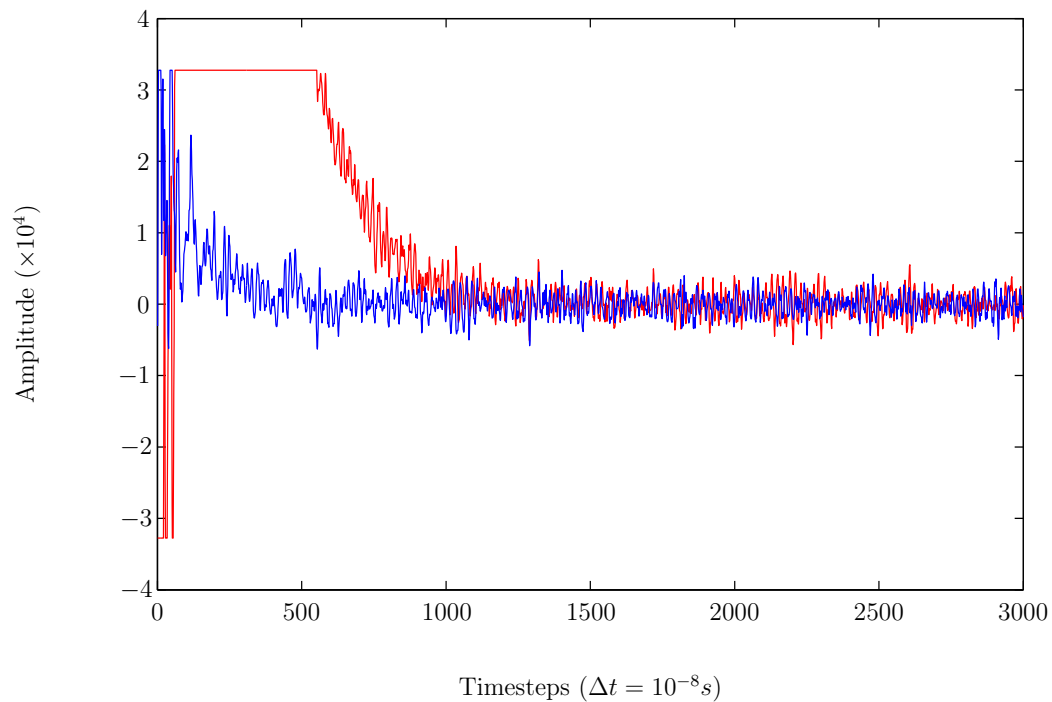


Figure 2.9: The first 3000 timesteps of the experimental data as described in Table C.1, Appendix C. The red signal is the result of transmitting and receiving on element 12 of the array. The blue signal is the result of transmitting on element 12 and receiving on element 13. It can be seen that the simultaneous transmission and reception at element 12 results in high amplitude interference for the first part of the signal. This is manifested in the scattering matrices by a dominating pulse-echo response.

the strongest scatterer can be associated to the largest singular value [81]. Hence, plotting the maximum singular value of each scattering matrix in the tiled domain, it was hoped that the global maximum of the curve would indicate the presence of a defect. The results for the three cases above are displayed in Figure 2.10, where the normalised maximum singular value of each matrix is plotted. In the case of the homogeneous media (the blue curve) the maximum occurs at tile index 5, which relates to the central matrix of the tiled domain and hence the flaw. However, once a multi-scattering media is introduced via the finite element simulation as discussed in Appendix B (green curve), the maximum singular values appear to relate to the backwall. In the experimental case (as described in Appendix C and depicted here by the red curve) the scattering matrices containing the high amplitude ring down dominate. However, it can be noted that the singular values relative to the flaw location are much larger than those associated with scattering by the microstructure. The work by Aubry and Derode in [82], which studies the varying behaviour of the singular value decomposition relating to matrices arising from single scatterers and multiple scatterers, could potentially be used to improve upon the extraction of the relevant singular values associated with large scatterers, and build upon the currently empirical nature of the Tiling Method.

2.2.2 The Factorisation Method

The Factorisation Method is the continuous analogue of the MUSIC algorithm [83, 84, 85] and belongs to a class of non-iterative methods known as sampling methods, which deal with the inverse problem of shape identification. Other such methods include the Linear Sampling Method [36, 37, 80], the Probe Method [36, 38, 80] and the Singular Sources Method [36, 39, 80]. These sampling meth-

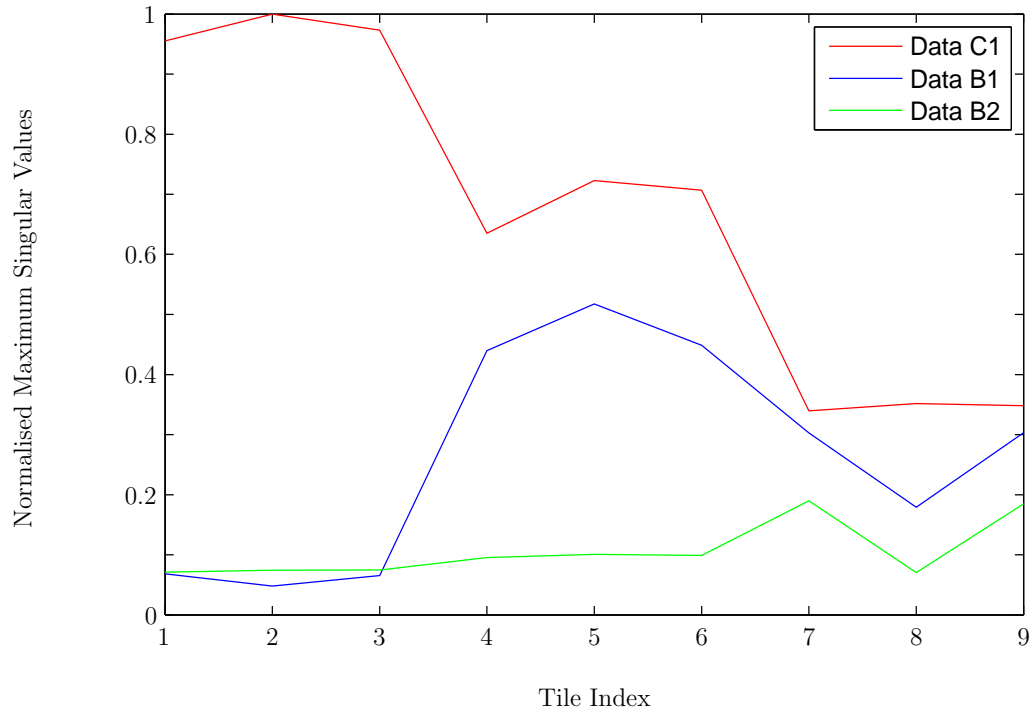


Figure 2.10: Plots of the maximum singular value for each tile. The blue curve corresponds to the tiling in Figure 2.6 as generated by the data in Table B.1, Appendix B, the green corresponds to Figure 2.7 as generated by the data in Table B.2, Appendix B and the red to Figure 2.8 as generated by the data in Table C.1, Appendix C.

ods are so named since they work on the basis of determining whether sampled points within an imaging domain meet some criteria which determines whether they fall within the support of the flaw domain D . The advantage of the Factorisation Method over other sampling methods is that its criteria is both sufficient and necessary. Below, a brief derivation of the method with Dirichlet boundary conditions is shown, however it can be derived similarly for Neumann boundary conditions [36, 86].

2.2.2.1 The Factorisation Method

The forward scattering problem states that there is an incident plane wave, $u^i(x, \theta) = e^{ikx \cdot \theta}$, $x \in \mathbb{R}^3$, travelling in direction $\theta \in S^2$, where $S^2 = \{x \in \mathbb{R}^3 : |x| = 1\}$ is the unit sphere in \mathbb{R}^3 . On encountering a defect, in this case the region D with boundary Γ , the wave scatters, giving the scattered field u^s . The sum of the incident and scattered fields results in the total field u , which satisfies the Helmholtz equation

$$\begin{aligned} \Delta u + k^2 u &= 0 && \text{outside } D, \\ \text{subject to } u &= f && \text{on } \Gamma \end{aligned} \tag{2.4}$$

and the Sommerfeld radiation condition

$$\frac{\partial u}{\partial r} - iku = \mathcal{O}(r^{-2}) \quad \text{for } r = |x| \rightarrow \infty \tag{2.5}$$

which ensures the wave is radiating outwards and decays sufficiently fast so that there are no sources at infinity. The Factorisation Method attempts to solve the inverse problem of determining the shape of D from the scattered field u^s . To do

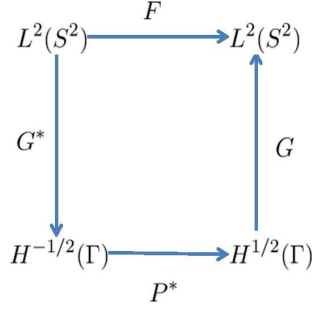


Figure 2.11: Factorisation of F .

so, it exploits the relationship of the data-to-pattern operator G with the shape of the scatterer. To begin the derivation, let Φ be the fundamental solution to the Helmholtz equation; a spherical wave generated at a point source z and measured at point x

$$\Phi(x, z) = \frac{e^{ik|x-z|}}{4\pi|x-z|}, \quad x \notin D. \quad (2.6)$$

As the distance between x and z approaches infinity, the spherical wave begins to resemble a plane wave at point x . This can be approximated by

$$u^\infty(\hat{x}) = e^{-ik\hat{x}\cdot z}, \quad \hat{x} \in S^2. \quad (2.7)$$

where $u^\infty(\hat{x}, \theta)$ is called the far field pattern of u^s (that is, the responses observed at a distance which is significantly larger than the wavelength). The far-field operator F is defined by

$$Fg(\hat{x}) = \int_{S^2} u^\infty(\hat{x}, \theta)g(\theta)ds(\theta) \quad \text{for} \quad \hat{x} \in S^2. \quad (2.8)$$

Deriving the following factorisation of the operator F

$$F = -GP^*G^*, \quad (2.9)$$

is the basis for the Factorisation Method (see Figure 2.11). Here $P^* : H^{-1/2}(\Gamma) \rightarrow H^{1/2}(\Gamma)$ is the L^2 adjoint of the single layer boundary operator $P : H^{-1/2}(\Gamma) \rightarrow H^{1/2}(\Gamma)$

$$P\varphi(x) = \int_{\Gamma} \Phi(x, y)\varphi(y)ds(y), \quad x \in \Gamma, \quad (2.10)$$

which converts the incoming wave to an outgoing wave on the boundary. $G^* : L^2(S^2) \rightarrow H^{-1/2}(\Gamma)$ is the L^2 adjoint of $G : H^{1/2}(\Gamma) \rightarrow L^2(S^2)$, the data-to-pattern operator, defined by

$$Gf = u^\infty, \quad (2.11)$$

where $u^\infty \in L^2(S^2)$ is the far field pattern of u ; a solution satisfying equations (2.4) and (2.5). Critically, the range of the operator G has a direct relationship to the shape of the domain D . For $z \in \mathbb{R}^3$ define $\phi_z \in L^2(S^2)$ by [36, equation (1.41)]

$$\phi_z(\hat{x}) = e^{-ik\hat{x}\cdot z}, \quad \hat{x} \in S^2. \quad (2.12)$$

Now if $u(x) = \Phi(x, z)$ is the fundamental solution of the Helmholtz equation and $z \in D$, then, from equations (2.7) and (2.12), $\phi_z = u^\infty$ and so, from equation (2.11), $\phi_z \in R(G)$ when $z \in D$. The converse is also true according to [36, Theorem 1.12]. To gain an exact characterisation of $R(G)$ in terms of the known operator F , we can relate G to F by equation (2.9). It is assumed that F , for the Dirichlet boundary conditions (equation (2.4)), is normal, the operator $I + ikF/8\pi^2$ is unitary and k^2 is not a Dirichlet eigenvalue (these conditions are justified in [36]). It then holds that the range of $(F^*F)^{1/4}$ coincides with that of G (as stated in [36, Theorem 1.24]). Hence, the sampling point $z \in \mathbb{R}^3$ lies in D

if and only if

$$(F^*F)^{1/4}g = \phi_z \quad (2.13)$$

for some $g \in L^2(S^2)$. By Picard's criterion, equation (2.13) is solvable if and only if the condition $\phi_z \in R((F^*F)^{1/4})$ is satisfied (this is shown to hold by equations (2.7)-(2.11) and [36, Theorem 1.24]) and the condition

$$\sum_{j=1}^{\infty} \frac{|(\phi_z, \psi_j)_{L^2(S^2)}|^2}{|\lambda_j|} < \infty, \quad (2.14)$$

holds, where $\{\lambda_j, \psi_j\}$ forms an eigensystem of the normal operator F (that is to say, the Fourier coefficients must decay to zero faster than the eigenvalues). Using the spectral theory of a normal operator, [36, equation 1.74] it is observed

$$(F^*F)^{-1/4}\phi_z = \sum_{j=1}^{\infty} \frac{1}{\sqrt{|\lambda_j|}} (\phi_z, \psi_j) \psi_j \quad (2.15)$$

$$\iff \sum_{j=1}^{\infty} \left| \frac{1}{\sqrt{|\lambda_j|}} (\phi_z, \psi_j) \right|^2 < \infty, \quad (2.16)$$

and so equation (2.14) does indeed hold. From equations (2.13) and (2.15), the solution g is given by

$$g = \sum_j \frac{(\phi_z, \psi_j)_{L^2(S^2)}}{\sqrt{|\lambda_j|}} \psi_j \quad (2.17)$$

and the following result is obtained

$$\begin{aligned} z \in D &\iff \phi_z \in R((F^*F)^{1/4}) \\ &\iff W(z) = \left[\sum_j \frac{|(\phi_z, \psi_j)_{L^2(S^2)}|^2}{|\lambda_j|} \right]^{-1} > 0. \end{aligned} \quad (2.18)$$

Using a discrete array this can be truncated

$$w(z) = \left[\sum_{j=1}^N \frac{|(\phi_z, \psi_j)_{L^2(S^2)}|^2}{|\lambda_j|} \right]^{-1} > \varepsilon, \quad z \in D, \quad (2.19)$$

where N is the number of array elements and $\varepsilon > 0$. By plotting $w(z)$ for all sampling points, z , it is possible to recover the shape and size of the defect.

2.2.2.2 The $F_{\#}$ Operator

It was shown above that a sampling point z lies within the domain D of the scatterer if and only if there exists a solution in $L^2(S^2)$ to equation (2.13). However, this criterion only holds if the far-field operator F is normal, which is not always the case when limited angles of inspection or heterogeneous host materials are present. To amend this, the $F_{\#}$ operator is introduced [36, 87]

$$F_{\#} = |Re(F)| + |Im(F)| \quad (2.20)$$

where

$$Re(F) = \frac{1}{2}(F + F^*) \quad \text{and} \quad Im(F) = \frac{1}{2i}(F - F^*). \quad (2.21)$$

It can be subsequently shown that a sample point z belongs to the domain D if and only if the integral equation

$$F_{\#}^{1/2} \psi = \phi \quad (2.22)$$

has a solution in $L^2(S^2)$ [36]. It follows that, by plotting

$$W(z) = \left[\sum_{j=1}^N \frac{|(\phi_z, \psi_j)_{L^2(S^2)}|^2}{\lambda_j} \right]^{-1}, \quad z \in \mathbb{R}^2 \quad (2.23)$$

where $\{\lambda_j, \psi_j\}_{j \in \mathbb{N}}$ is an eigensystem of the self-adjoint operator $F_{\#}$, an image of the scatterer can be reconstructed.

2.2.3 Application of the Factorisation Method

In applications, where a discrete set of transmit-receive positions are used, the far-field operator F is given by a scattering matrix $F(\theta_j, \theta_l, k)$, where θ_j is the incident wave direction, θ_l is the scattered wave direction and k is the wave number. Below, the Factorisation method is first applied to the ideal case where a scattering matrix $F(\theta_j, \theta_l, k)$ has been generated by the Born Approximation with a full aperture array and homogeneous host medium. A limited angle of inspection is then introduced before application to non-normal scattering matrices arising from FMC data which has been (a) generated by finite element simulations and (b) experimentally collected.

2.2.3.1 Application to Data as Modelled by the Born Approximation

Figure 2.12, images (a) and (b), depict schematics of two different flaws. Their dimensions were input into the Born approximation and the corresponding full aperture scattering matrices (see Section 3.3) were generated. The Factorisation Method was applied to these scattering matrices and the resulting reconstructions can be seen in images (c) and (d). Image (c) shows a near perfect reconstruction of the disc with radius 2.5mm as shown in image (a). Image (b) depicts an ellipse of

dimensions $5\text{mm} \times 1\text{mm}$ and 40° orientation. The Factorisation Method produces the accurate reconstruction shown in image (d), which captures the length and orientation of the ellipse. The strong scattering at the specular reflection causes some shadowing across its width but this can be overcome with image thresholding if desired. In Section 2.2.2.2, the $F_{\#}$ operator was discussed to allow for

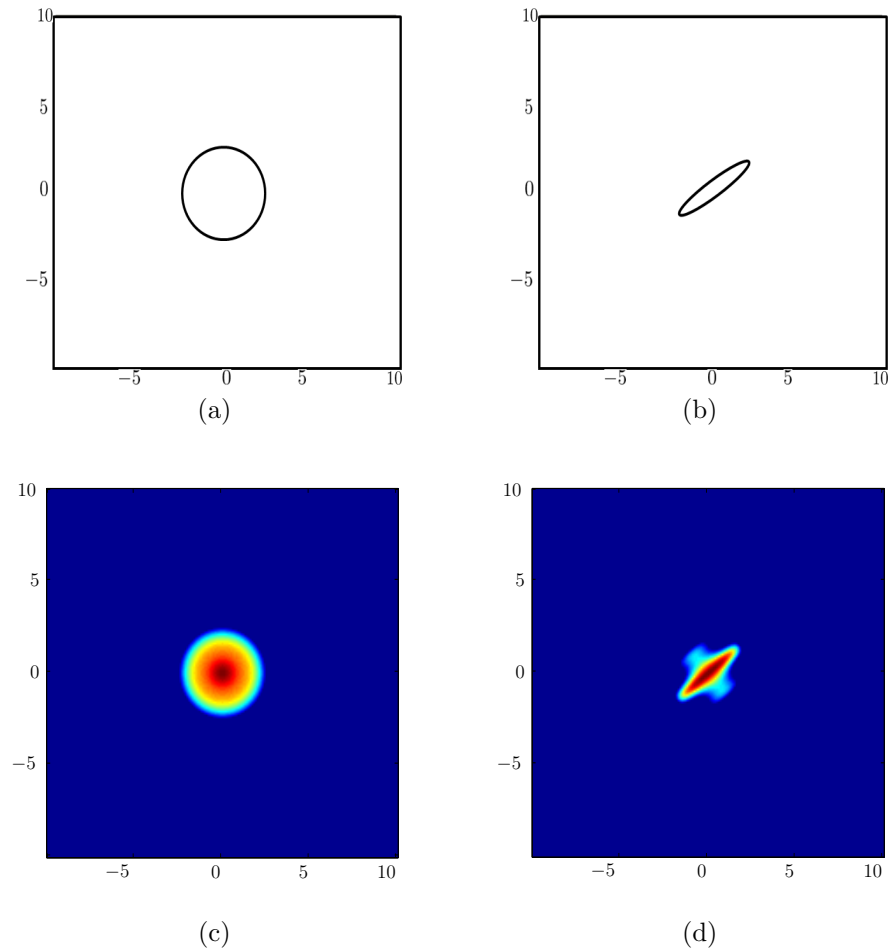
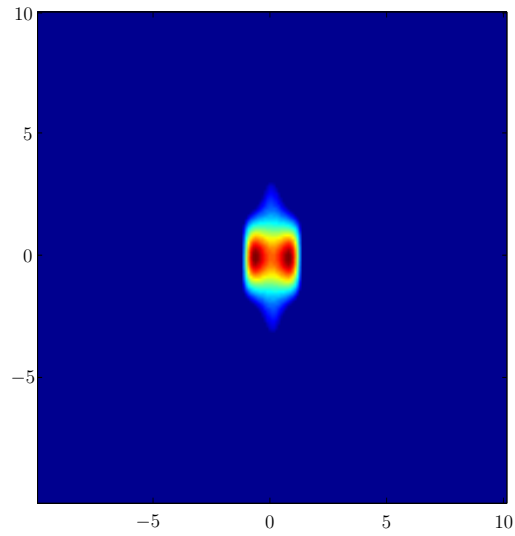


Figure 2.12: Images (a) and (b) depict the actual shape of the flaws as modelled by the Born approximation, where a 180 element, circular array was simulated to encircle the flaws at a distance of 50mm. Images (c) and (d) are the resulting reconstructions by the Factorisation method. The imaging domains have been cropped to allow for closer inspection and the axes represent the local axes, measured in millimetres.

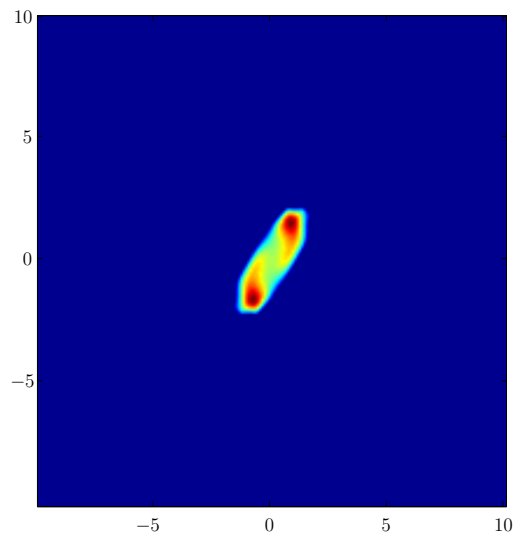
application of the Factorisation method to non-normal, far-field operators. In [36] it is indicated that in the case of *limited data*, where the far field pattern $u^\infty(\hat{x}, \theta)$ is known only for $\hat{x}, \theta \in U$, $U \subset S^2$ (that is, where there is a limited angle of inspection), the far field operator F is not normal. However, in our discrete, numerical implementations, the scattering matrix $F(\theta_j, \theta_l, k)$ arising from the Born approximation, where a linear array is placed centrally above the flaw, is normal. Hence, the $F_\#$ operator is not yet needed. Figure 2.13 depicts reconstructions of the flaws as depicted in images (a) and (b) of Figure 2.12, where the scattering of the ultrasound wave is modelled by the Born approximation, incorporating a 64 element linear array placed 50mm above the flaws. The reconstruction of the the 2.5mm radius disc depicts an ellipse of approximately 3mm \times 5mm, although this is dependent on thresholding (here the image is plotted with a dynamic range of 10dB and measurements are taken along the x and y axes). Image (b) shows the reconstruction of the 5mm \times 1mm ellipse at 40° orientation (also plotted at a dynamic range of 10dB with measurements taken along the main axes of the flaw). The resulting image depicts an ellipse-like scatterer of approximately 6mm \times 1.5mm and 50° orientation.

2.2.3.2 Application of the Factorisation Method to Data as Modelled by Finite Element Simulated Data

To further explore the Factorisation Method’s abilities in imaging, specifically for application to nondestructive evaluation, a simulation of a sinusoidal wave travelling through a homogeneous medium has been generated by the the software package PZFlex (see Appendix B). Cracks of length 5mm at 0° and 40° have been inserted 50mm below the simulated ultrasonic transducer array. The



(a)



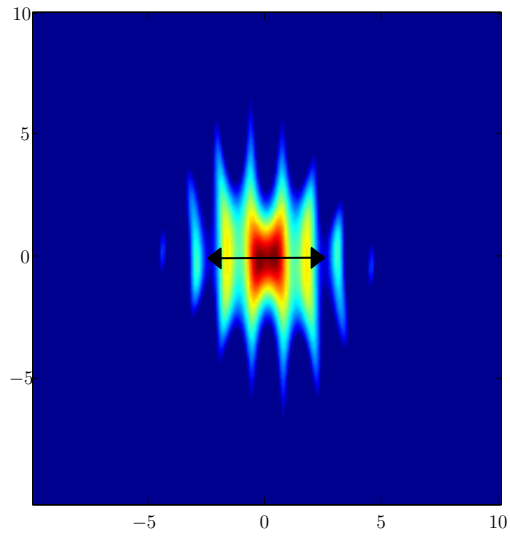
(b)

Figure 2.13: Reconstructions of the flaws as depicted in images (a) and (b) in Figure 2.12 via the Factorisation method. The scattering of the ultrasound wave by these flaws was modelled by the Born approximation, incorporating a 64 element, limited aperture, linear array placed centrally 50mm above the flaws.

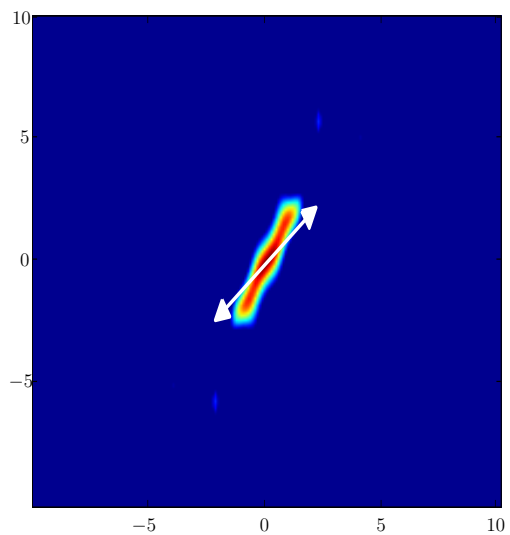
resulting non-normal scattering matrices have led to the reconstructions, by the Factorisation Method in conjunction with the $F_{\#}$ operator, as depicted in Figure 2.14. Image (a) corresponds to the 0° orientated crack. Although the length and primary orientation of the reconstructed flaw are comparable to the actual crack size and orientation, the crack like form is not well characterised. However, it can be observed that background noise is no longer an issue due to the binary criteria on which the Factorisation Method is based on. Image (b) depicts an excellent reconstruction of the 5mm crack at 40° orientation. This leads to the conclusion that the high amplitude specular reflections present in the 0° case can overshadow smaller facets of the flaw and lead to a distorted image.

2.2.3.3 Application of the Factorisation Method to Experimental Data

The final test for the algorithm was in its application to the experimental data as described by Table C.2 in Appendix C. The resulting reconstruction is shown in Figure 2.15. The Factorisation Method has successfully detected the crack-like form and 40° orientation of the defect, however the high amplitude pixels in the centre of the image indicate a smaller crack length than the expected 6mm. Despite this error in sizing, the image remains impressive due to the high SNR of 35.4dB, which is more than double the value achieved via the TFM for the same dataset (see Section 2.1.1, Figure 2.3). It must be noted that this particular reconstruction was generated by the scattering matrix plotted at 4.5MHz and was chosen due to its crack-like representation and accurate orientation. However, at other frequencies these aspects were sometimes lost. For further, practical implementation, an algorithm for choosing the optimal frequency must be constructed or a multi-frequency approach developed [88].

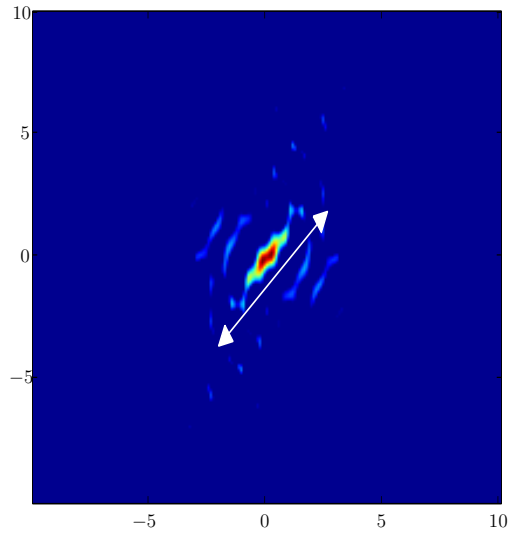


(a)



(b)

Figure 2.14: Reconstructions by the Factorisation Method of a 5mm crack at orientations (a) 0° and (b) 40° generated by PZFlex simulations as described in Appendix B, Table B.1.



(a)

Figure 2.15: Reconstruction by the Factorisation Method of a 6mm lack of fusion crack from experimental data as detailed in Table C.2 in Appendix C. The arrow depicts the actual size and orientation of the flaw.

2.3 Subjectivity of Methods

The above sections have examined existing techniques for the detection and characterisation of defects via the exploitation of FMC data arising from ultrasonic phased array inspections. A common factor for each technique is the subjective thresholding needed to estimate the size of the flaw. An example of the effects of using varying dynamic ranges to plot TFM results is shown in Figure 2.16. Image (a) has been plotted at a dynamic range of 10dB and image (b) is plotted at 40db. Although image (a) minimises the effects of noise, the flaw characterisation is weak and looks much smaller than that plotted in image (b). Figure 2.17 depicts a similar study of results obtained via the Factorisation Method for the same dataset where the effect seems to be even more extreme. Plotting at 10db, it appears the

Factorisation Method has managed to distinguish between the signal and noise with its in/out criteria. However, plotting at 40dB, the impressive signal to noise ratio has drastically decreased. The subjective nature of these results could

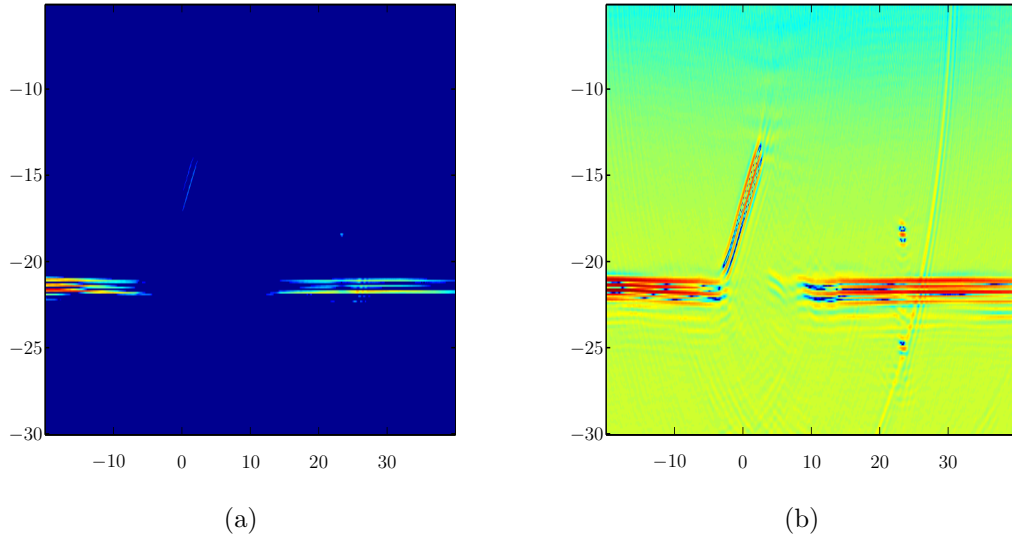


Figure 2.16: TFM images arising from FMC data collected experimentally from the sample as described in Table C.2. Image (a) is plotted at a dynamic range of 10dB and image (b) is plotted with a dynamic range of 40dB.

potentially lead to differing characterisations between operators and companies. Although guidelines can be drawn up to allow for standardisation, an alternative, and arguably more reliable approach, is to create a completely objective method for flaw sizing.

2.4 Conclusions

The Total Focussing Method has dominated the nondestructive testing industry as the imaging algorithm of choice due to its simplicity and effectiveness. However, in its standard form, it can struggle with the characterisation of defects, and, in

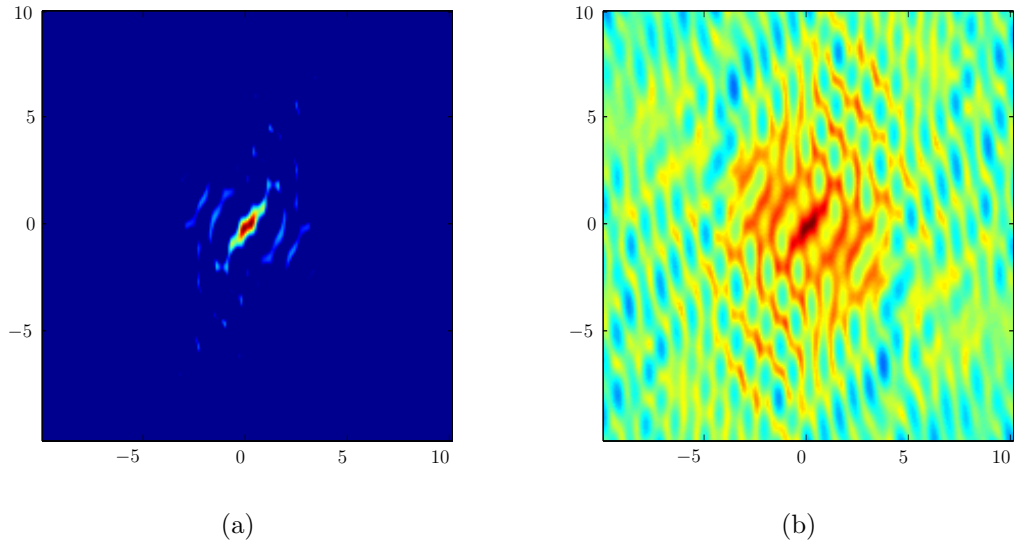


Figure 2.17: Images arising from application of the Factorisation Method to scattering matrices generated by the FMC data collected experimentally from the sample as described in Table C.2. Image (a) is plotted at a dynamic range of 10dB and image (b) is plotted with a dynamic range of 40dB.

particularly difficult cases, where the sample in question is a highly heterogeneous material, it can sometimes fail to detect flaws all together. It is suggested that the obscuring effect of host material heterogeneities can be diminished by operating in the time-frequency domain instead, where the frequency spectrum of a wave scattered by a flaw can be distinguished from that arising from scattering by the microstructure.

Operating under this assumption, an element of novelty was introduced in Section 2.2.1 with the development of a time-frequency domain detection algorithm; the Tiling Method. Although characterisation in the time-frequency domain has been explored [36], detection in the time-frequency domain appears to be uncharted territory. The Tiling Method simply constructs a sparse grid in the imaging domain which is then filled by scattering matrices generated by taking a discrete

Fourier transform over the time taken to reach the centre point of each tile. It was initially applied to data arising from finite element simulations and the results proved promising. However, the argument for working in the time-frequency domain lies in the potential for better distinction between flaws and heterogeneities. Hence the algorithm's real test was in its application to data in which the TFM struggled to detect a large crack lying perpendicular to the array, in a highly heterogeneous medium. Although the results were not as clear as in its previous applications, it did give an indication of a defect at the correct depth. It must be noted that further work is required to improve upon the empirical nature of the algorithm and it is suggested that this could be achieved by further examination of the singular value decomposition of the matrices. The final section of this chapter examined, adapted and implemented the Factorisation Method, applying it to increasingly difficult situations. When applied to the ideal, full aperture, homogeneous dataset as modelled by the Born approximation, a near perfect reconstruction of the flaw was obtained. Introducing a limited angle of inspection required the use of the $F_{\#}$ operator to ensure the scattering matrix was normal. In its final stage the algorithm was applied to experimental data. It successfully characterised the form (crack-like) and orientation of the defect but the subjective crack length measurement exhibited an error. It was also noted that for further, practical implementation, some sort of criteria must be developed for choosing the optimum frequency at which to operate at or a multi-frequency approach adopted.

A final comment was made on the subjectivity of the existing methods examined in this chapter. The need for thresholding can potentially lead to varying characterisations between operators and companies. Although guidelines for standardisation can minimise the problem, the final estimation is still prone to human

error. The following two chapters of this thesis aim to create a completely objective approach to flaw sizing to combat these problems.

Chapter 3

A Model Based Approach to Crack Sizing in the Frequency Domain

3.1 Introduction

In this chapter, a model-based crack sizing algorithm for zero-volume flaws is proposed so as to remove the subjectivity (inherent to the methods described in Chapter 2) from crack size and orientation estimations. Two explicit expressions for the crack length are derived from the approximation of the scattering amplitude arising from a volumetric flaw in an elastic medium, as formulated by the Born approximation (Section 3.4). The first corresponds to the simplified case where the flaw lies parallel to the ultrasonic array, and the second extends this to the case where the crack orientation can also be extracted. Section 3.5 is dedicated to the error analysis of both models.

Work on objective crack sizing has previously been explored in [41], where both the maximum scattering amplitude and the half-width, half-maximum (HWHM) measurement of the pulse-echo response of a scattering matrix, were shown to correlate with the crack length. The method presented here is similar only in its exploitation of the frequency domain scattering matrices that arise when an incident pressure wave is scattered by a flaw. Favouring the roots of the pulse-echo response plot over the HWHM, the proposed crack-sizing algorithm is immune to the effects of the transducer transfer function. It is based on a mathematical model rather than empirical analysis and improves upon current imaging protocols as its determination of the crack size and orientation is objective and does not rely on a subjective choice of point spread function thresholding. Similar work on the extraction of properties of small volume scatterers from boundary measurements has previously been undertaken by Ammari et al in Paris [89]. Here, an approximation of the location and polarization tensor [90] of a conductivity anomaly is made from measurements of the electromagnetic field at the boundary. It must be noted that the polarisation tensor contains information on both the conductivity and the volume of the inhomogeneity. Hence, a small inhomogeneity with a high conductivity can potentially exhibit the same polarisation tensor as a large inhomogeneity with a low conductivity and it is not possible to determine these characteristics independently of each other [91]. In contrast, the method presented below can produce an explicit estimate of the flaw dimensions from boundary measurements but conversely requires *a priori* knowledge of the location of the flaw to do so.

3.2 The Born Approximation

To develop an understanding of the scattering of an ultrasound wave by a crack [92], and to facilitate work on model based crack-sizing, an analytic mathematical model has been investigated. The Born approximation [93, 94, 95] is a low-frequency, weak scattering approximation for volumetric flaws which is used to relate the flaw response directly to the flaw geometry. It is a widely accepted scattering model taken originally from quantum mechanics and is based on the assumption that, within the scatterer, the scattered field is comparatively small to the incident field, which hence allows the total field to be approximated by the incident field only. Thus it is a single scattering approximation which assumes the wave passes through the flaw undisturbed (it neglects interactions between multiple flaws and between any two parts of the same flaw) and relies on the flaw medium having similar material properties to that of the host medium. A low-frequency assumption is also required so as that the phase change on interaction with the flaw is sufficiently small.

These restrictions at first appear incompatible with our objective which is to study scattering by a crack where there exists a high contrast between the flaw and host media. For example, assuming a large change in velocity as a consequence of the contrasting media, refraction would alter the forward direction of the wave within the flaw and the direction of the incident wave would not be preserved, thus rendering the Born approximation invalid (see Figure 3.1). However, as we are primarily concerned with the wave in the backscattered direction (due to the limited angles of inspection typically available within an NDT setting), the discordant effects of the scattering as the wave passes through the flaw can be neglected. Hence, the geometry of the scattering matrix arising from the limited aperture

inspection of a flaw is dependent only on the direction of the reflected waves at the boundary. These should remain consistent despite the contrast between the flaw and host media (the angles of reflection are dependent on the shape of the scatterer, only the amplitudes of the reflected waves are affected by the material properties). Work by Gubernatis et al in [96] shows good agreement between the Born approximation and the exact solution for scattering by a spherical void in Titanium when the forward directions are excluded. Further application of the Born approximation in the context of elastic wave scattering by voids and cracks is demonstrated in [97, 98]. In this chapter, the Born approximation is used to estimate the scattering amplitude arising from an incident wave of given direction coming into contact with a known domain, D , which is set as an ellipse with a high aspect ratio to mimic a crack-like scatterer (note that the forward scattering problem is described in Section 2.2.2). The amplitudes are then normalised and the geometry of the scattering matrix is used to extract information on the flaw size.

The Born approximation estimates the scattered field and provides an explicit expression in the frequency domain for the scattering amplitude, $A_n^{\alpha;\beta}(\mathbf{e}_i^\beta, \mathbf{e}_s^\alpha)$, for a homogeneous, volumetric inclusion with a wave transmitted in direction \mathbf{e}_i and received in direction \mathbf{e}_s . The superscripts α and β dictate the type (pressure, shear vertical or shear horizontal) of incident and scattered wave, respectively, and n is the component of A being calculated. The derivation of the Born approximation for the fluid case is shown in Appendix A but for the purposes of this chapter, we consider the scattering by an ellipsoidal inclusion in an elastic medium. Restricting attention to the two dimensional plane below the linear array this is given by [94,

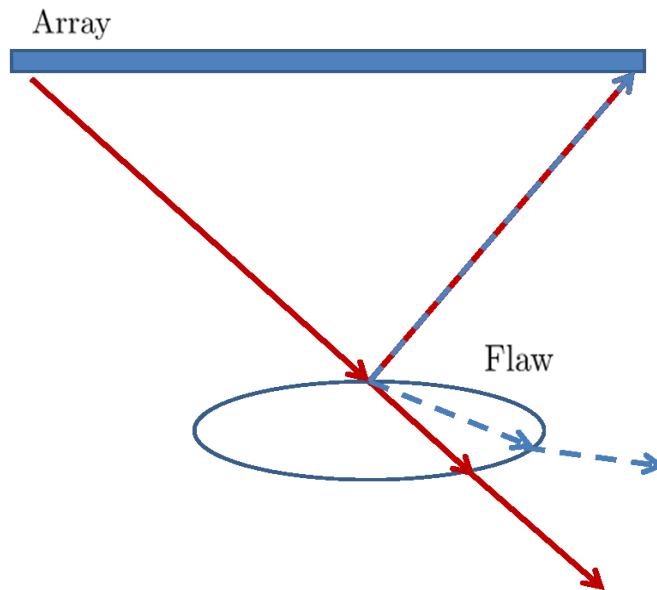


Figure 3.1: The Born approximation is a single scattering approximation based on the assumption that the total field can be approximated by the incident field within the scatterer, thus ignoring the scattered field and allowing the wave to pass through the flaw undisturbed. This assumption is accurate when the flaw and host media exhibit similar material properties and the direction of the incident wave is not altered by refraction (red arrows). If there exists a high contrast between the flaw and host medium, the incident wave direction is not preserved (blue arrows) and using it to estimate the total field would lead to an invalid approximation for the scattering in the forward direction. However, as we are solely concerned with backscattered waves and the angles of reflection (which should remain consistent despite the contrasting media) and not the amplitudes of the reflected waves, the Born approximation is suitable for our purposes.

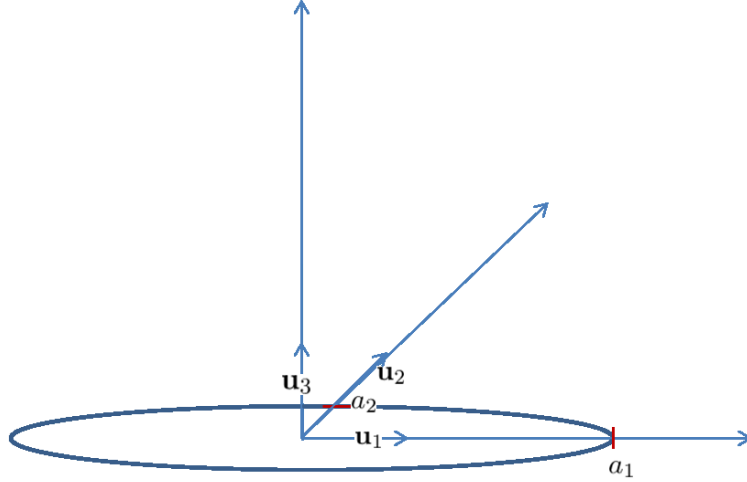


Figure 3.2: The flaw is approximated by an ellipsoid with $a_3 = 0$. The defect length is equal to $2a_1$ and its width is $2a_2$. To simulate a crack, $a_1 \gg a_2$.

equation 10.220]

$$A_n^{\alpha;\beta}(\mathbf{e}_i^\beta, \mathbf{e}_s^\alpha) = -\frac{a_1 a_2 B_{ln}^\alpha f_l(\mathbf{e}_i^\beta, \mathbf{e}_s^\alpha)}{|\mathbf{g}^{\alpha;\beta}|^2 (r_e^{\alpha;\beta})^2} \left(\frac{\sin(k_{\alpha 0} |\mathbf{g}^{\alpha;\beta}| r_e^{\alpha;\beta}) - k_{\alpha 0} |\mathbf{g}^{\alpha;\beta}| r_e^{\alpha;\beta} \cos(k_{\alpha 0} |\mathbf{g}^{\alpha;\beta}| r_e^{\alpha;\beta})}{k_{\alpha 0} |\mathbf{g}^{\alpha;\beta}| r_e^{\alpha;\beta}} \right) \quad (3.1)$$

where a_1 and a_2 represent the flaw dimensions, $k_{\alpha 0}$ is the wavenumber in the host material, $\mathbf{g}^{\alpha;\beta} = \mathbf{e}_i^\beta - \mathbf{e}_s^\alpha$ and $r_e^{\alpha;\beta}$ is the effective radius of the flaw, given by

$$r_e^{\alpha;\beta} = \sqrt{a_1^2 (\mathbf{e}_q \cdot \mathbf{u}_1)^2 + a_2^2 (\mathbf{e}_q \cdot \mathbf{u}_2)^2} \quad (3.2)$$

with

$$\mathbf{e}_q = \frac{\mathbf{g}^{\alpha;\beta}}{|\mathbf{g}^{\alpha;\beta}|}. \quad (3.3)$$

Unit vectors \mathbf{u}_1 and \mathbf{u}_2 lie in the vertical plane along the major and minor axes of the flaw. A schematic of the crack and its parameters can be seen in Figure 3.3. Considering the case where only pressure waves are being transmitted and received

($\alpha = \beta = P$) the coefficient $B_{ln}^\alpha f_l(\mathbf{e}_i^\beta, \mathbf{e}_s^\alpha)$ can be expressed as [94, equation 10.218]

$$B_{ln}^P f_l(\mathbf{e}_i^P, \mathbf{e}_s^P) = \left(\frac{\Delta\rho}{\rho_0} (\mathbf{e}_i^P \cdot \mathbf{e}_s^P) - \frac{(\Delta\Lambda + 2\Delta\mu)(\mathbf{e}_i^P \cdot \mathbf{e}_s^P)^2}{\rho_0 c_{p0}^2} \right) e_{sn}^P \quad (3.4)$$

where $\Delta\Lambda$ and $\Delta\mu$ are the differences between the Lamé co-efficients in the host material and flaw material, $\Delta\rho$ is the difference in their densities, and ρ_0 and c_{p0} are the density and pressure wave speed, respectively, in the host material. By changing the range of angles that the transmission and reception directions (\mathbf{e}_i and \mathbf{e}_s) can take, different array apertures can be simulated. The size, shape and location of the defect and the material properties can also be varied and hence allow closer comparison of the model to experimental data. For the method presented in this chapter, the focus will be on crack-like flaws where the crack is approximated as a two dimensional ellipsoid with a high aspect ratio, as depicted in Figure 3.2, where the flaw dimensions are set so that $a_1 \gg a_2$. The flaw orientation refers to the angle that \mathbf{u}_1 makes with the x -axis.

3.3 Scattering Matrices

The Born Approximation, as formulated in Section 3.2, provides an explicit expression for the scattering amplitude, $A_n^{P;P}(\mathbf{e}_i^P, \mathbf{e}_s^P)$, of an incident and scattered pressure wave between a pair of transmit/receive array elements at a specified frequency. Plotting the magnitude of this amplitude for every pair of array elements produces a scattering matrix. This matrix contains information on the size, form and orientation of the defect [40]. By plotting these matrices, patterns can be observed and later exploited to objectively characterise flaws (see Section 3.4). In this section, the effects of aperture, defect shape, orientation and depth on the

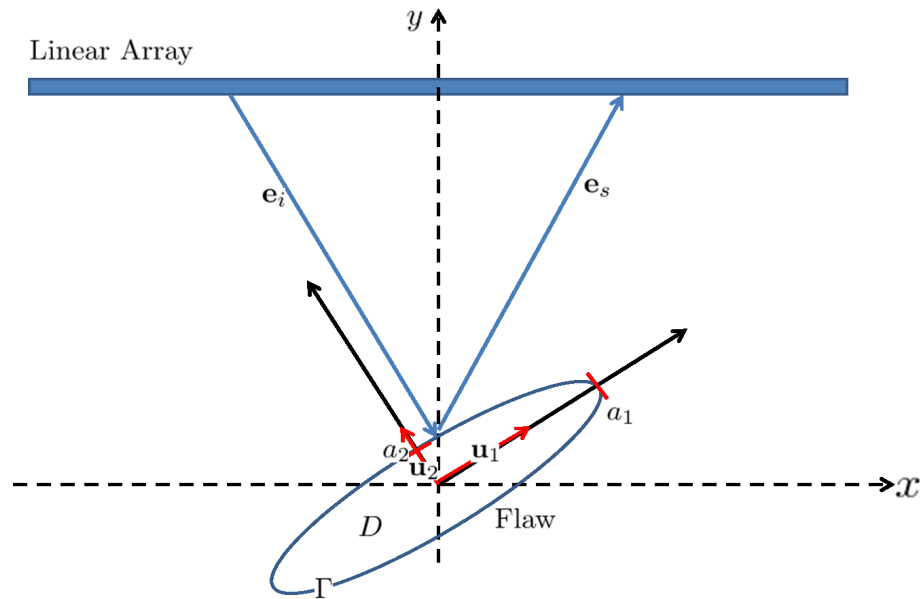


Figure 3.3: Schematic of an ellipsoidal flaw in relation to a linear array. D represents the domain of the flaw and Γ is the flaw boundary. The unit vectors \mathbf{e}_i and \mathbf{e}_s denote the transmission and reception directions, respectively. Unit vectors \mathbf{u}_1 and \mathbf{u}_2 lie in the vertical plane along the major and minor axes of the flaw and a_1 and a_2 are the flaw dimensions in directions \mathbf{u}_1 and \mathbf{u}_2 .

form of the scattering matrix will be demonstrated.

3.3.1 Aperture

Throughout this section, both circular and linear arrays are simulated with respect to the parameters in Table 3.1. The term full aperture will sometimes be used and refers to the case where a circular array has been simulated to encircle a defect, providing a 360° view. Limited aperture will be used in the case where a linear array is simulated directly above the flaw (hence limiting the angle of inspection) as shown in Figure 3.4. Scattering matrices corresponding to both set-ups can be seen in Figure 3.5. These have been generated according to the values given in Table 3.1. Plot (a) is generated by the simulation of a full aperture circular array inspecting a crack-like flaw of 0° orientation, with $a/\lambda = 1.4$ (where $a = 2a_1$ is the crack length and λ is the wavelength). The effects of changing this ratio are further explored in Section 3.4.1. The high amplitude lobes along the diagonal of the matrix correspond to the specular reflections (where the incident wave is perpendicular to the crack), that arise from transmitting and receiving at the same element (that is, the pulse-echo response at either element 45 or 135 in the schematic shown in Figure 3.4). The low amplitude troughs arise from the pulse-echo response at elements 1 and 90. This occurs due to the wave passing straight through the crack to the opposite side of the array (accounting for the high amplitude diagonal lines in the scattering matrix), with very little scattering reflecting back to the transmitting element and its neighbours, and almost no scattering being reflected at an angle of 90° to the incident direction. Plot (b) depicts a scattering matrix produced by the simulation of a linear array (with parameters as in Table 3.1), inspecting the same flaw. This matrix resembles the

submatrix of the full aperture scattering matrix in (a) corresponding to the 64 elements located approximately between elements 13 and 77.

| | Linear Array | Circular Array |
|------------------------------------------------------|-----------------------|-----------------------|
| Number of Array Elements | 64 | 180 |
| Pitch | 2mm | 2° (angular spacing) |
| Pressure Wave Velocity in Host Material (c_{P0}) | 6420m/s | 6420m/s |
| Shear Wave Velocity in Host Material (c_{s0}) | 3040m/s | 3040m/s |
| Density of Host Material (ρ_0) | 2700kg/m ³ | 2700kg/m ³ |
| Distance of Flaw from Array | 50mm | 50mm |

Table 3.1: Typical experimental parameters which have been input into the Born approximation to generate the scattering matrices as seen in this Section.

3.3.2 Defect Shape

The form of a defect can be categorised in two ways: volumetric (where the flaw occupies a finite region in space) or zero-volume (where the flaw is a discontinuity between the materials on either side). The model based algorithm discussed below in Section 3.4 is concerned solely with cracks (zero volume flaws) and it is therefore important to be able to distinguish between the two types of scattering matrix so as to know when the algorithm is applicable. Figure 3.6 shows these two types of scattering matrix. Plot (a) displays the scattering amplitudes generated by a circular flaw with dimensions $a_1 = a_2 = 2.5\text{mm}$ (here $a/\lambda \approx 1.4$, where $a = 2a_1$ is the diameter of the circular defect and λ is the wavelength),

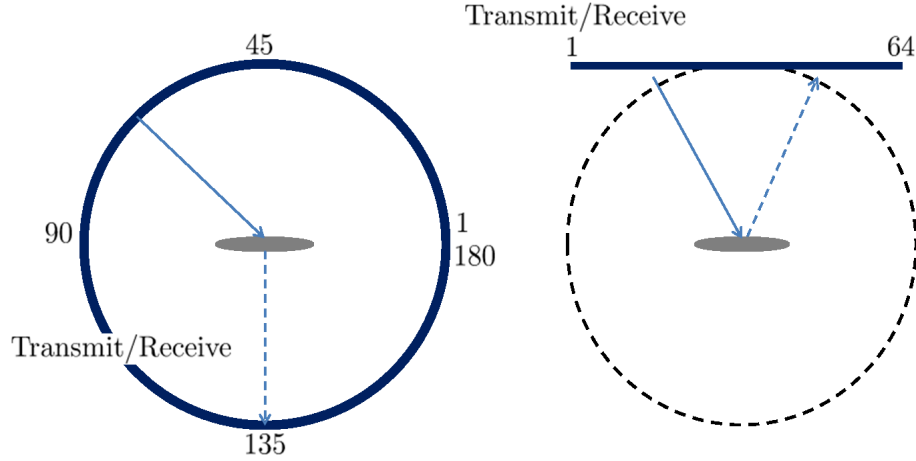


Figure 3.4: Schematic of a *Full Aperture* array simulation and a *Limited Aperture* array simulation. The bold lines indicate placement of array elements, the grey ellipsoid is a defect, the blue arrow is a transmitted wave and the dashed arrow is a corresponding received wave. The numbers corresponds to the array element labelling.

embedded in a homogeneous medium and inspected by a linear array with properties as described in Table 3.1. Plot (b) was produced by a crack-like defect with dimensions $a_1 = 2.5\text{mm}$ and $a_2 \approx 0$ (here $a/\lambda \approx 1.4$, where $a = 2a_1$ is the crack length), with 0° orientation (lying parallel to the array) in the same setting. There is a clear qualitative (and quantitative) difference between these two cases and by recognising that the striped scattering matrix arises from a disc and that the elliptical lobe scattering matrix is characteristic of a crack, it suggests that it should be possible to work backwards from the scattering matrices to extract information about the flaw shape and size.

3.3.3 Defect Orientation

The orientation of a crack effectively changes the location of the element at which the specular reflection is received. It has been previously observed (Section 3.3.1) that this specular reflection causes a high amplitude lobe along the diagonal of

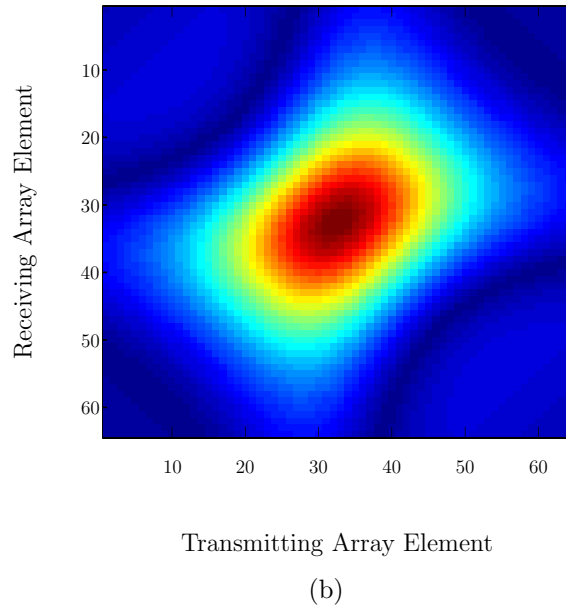
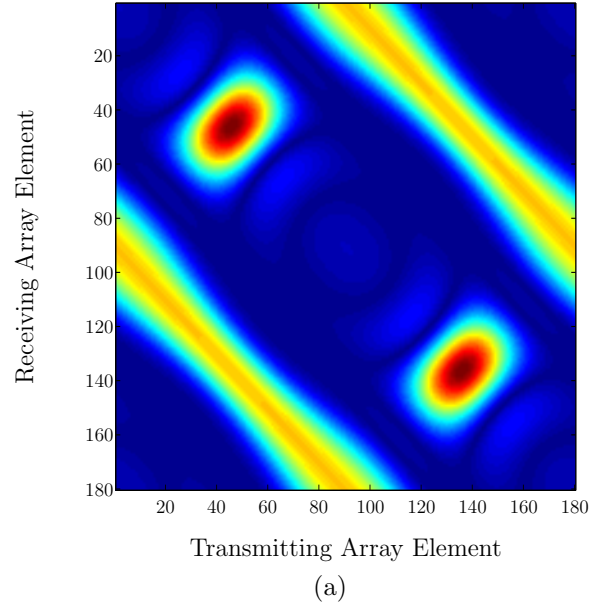
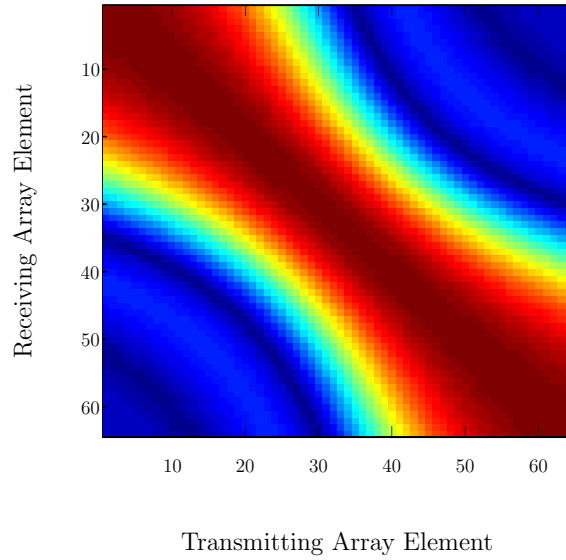
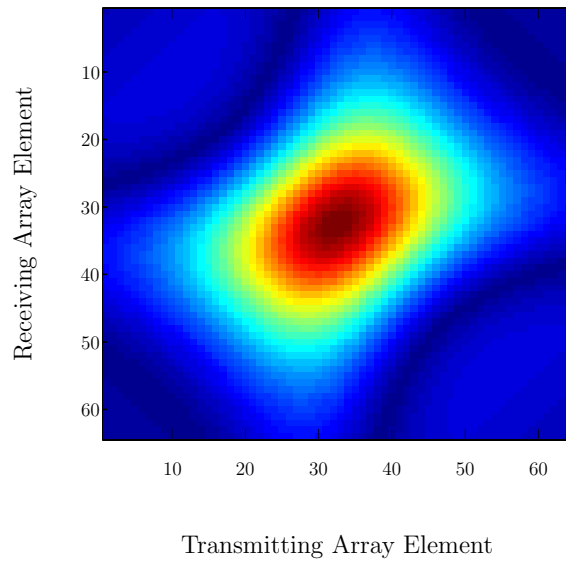


Figure 3.5: Scattering matrices generated by a crack of length $2a_1 = 5\text{mm}$ and 0° orientation inspected by (a) the circular array (b) the linear array as described in Table 3.1. Both measured at $2a_1/\lambda \approx 1.4$ in a homogeneous medium.



(a)



(b)

Figure 3.6: Scattering matrices : (a) A disc of radius $a_1 = a_2 = 2.5\text{mm}$ and (b) a crack of length $2a_1 = 5\text{mm}$ and orientation 0° inspected by the linear array as described in Table 3.1, measured at $a/\lambda \approx 1.4$ in a homogeneous medium.

the scattering matrix. The orientation of the crack dictates where along the diagonal this maximum will occur. This can be seen in Figure 3.7 where plots (a) and (b) depict scattering matrices arising from cracks orientated at 20° and 40° , respectively. A curvature of the central lobe is also apparent in these images. Since the array is linear and has no curvature then, as we move from one element to the next, the change in the angle that the normal to the crack edge makes with this next element varies in a nonlinear manner. This is rectified in the full aperture case, where the elements are spaced equally with respect to the angle ϕ (plot (d)). Plot (c) depicts the 90° crack case, where the crack is perpendicular to the array. Its high amplitude lobe has effectively split in half as the specular reflection occurs on either side of the crack edge. This is manifested in the corners of the scattering matrix with the central lobe corresponding to the diffraction by the crack tip.

3.3.4 Distance of Defect from the Array

Increasing the distance of the defect from the array has the effect of restricting the size of the maximum possible angle (Φ) between the outermost incident and scattered directions. The size of Φ dictates the extent of the scattering profile which is captured in the scattering matrix, effectively modifying the aperture of the array, as demonstrated in Figure 3.8. In Figure 3.9 (a), a crack has been inspected at a distance of only 20mm. Referring back to the schematic in Figure 3.8, it can be observed that the closer the flaw is to the array, the larger Φ is. So, in this case, both the main lobe and the side lobes of the scattering profile are captured by the array. In Figure 3.9 (b), the crack is at a distance of 100mm from the array and so the angle Φ is relatively small. Within this small interval,

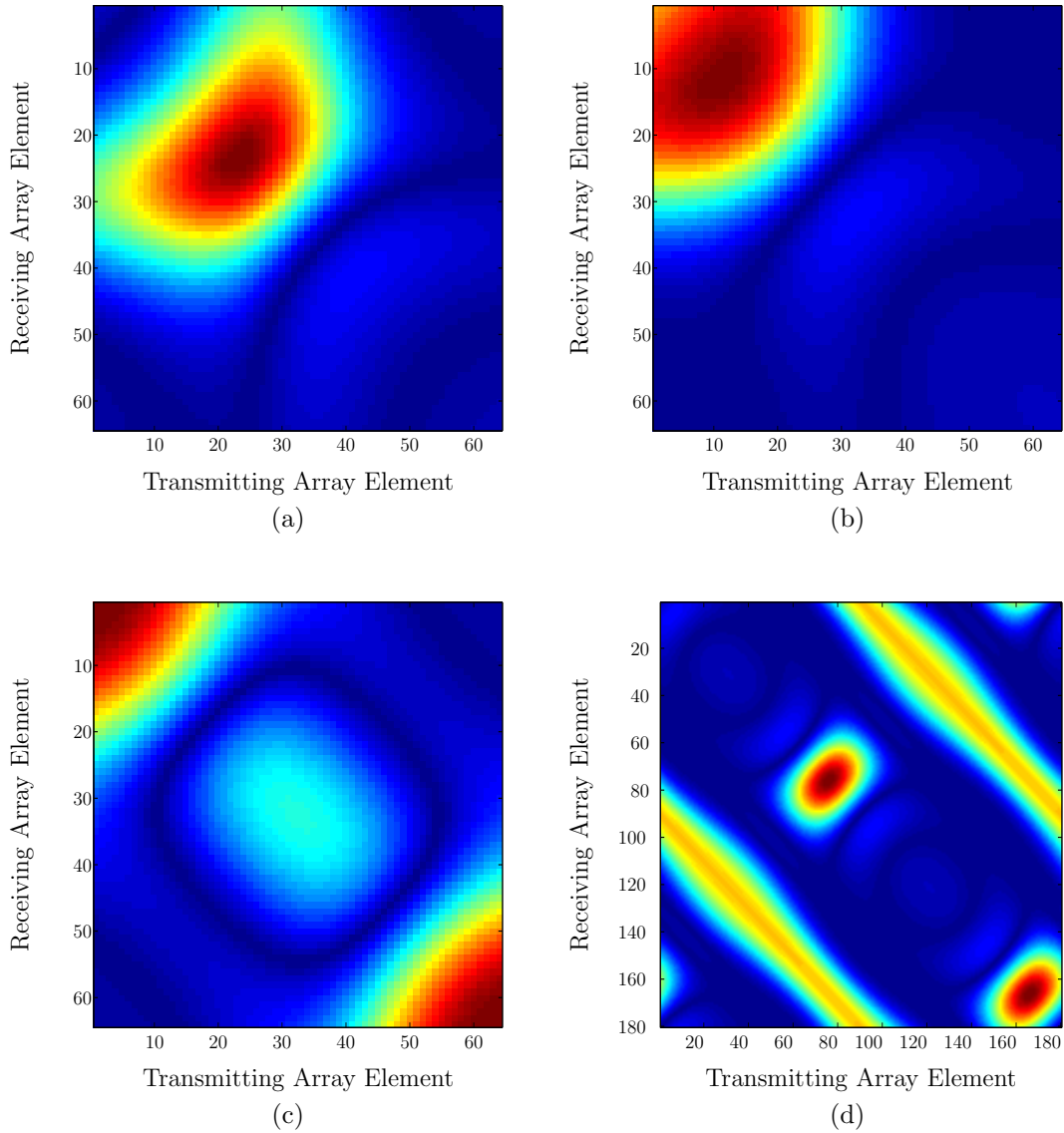


Figure 3.7: Scattering matrices for a crack inspected by the linear array as described in Table 3.1, measured at $a/\lambda \approx 1.4$ with orientations (a) 20° , (b) 40° and (c) 90° . Image (d) depicts a scattering matrix generated by a full aperture inspection for a 5mm crack with a crack orientation of 60° .

the main lobe of the scattering profile is only partially captured.

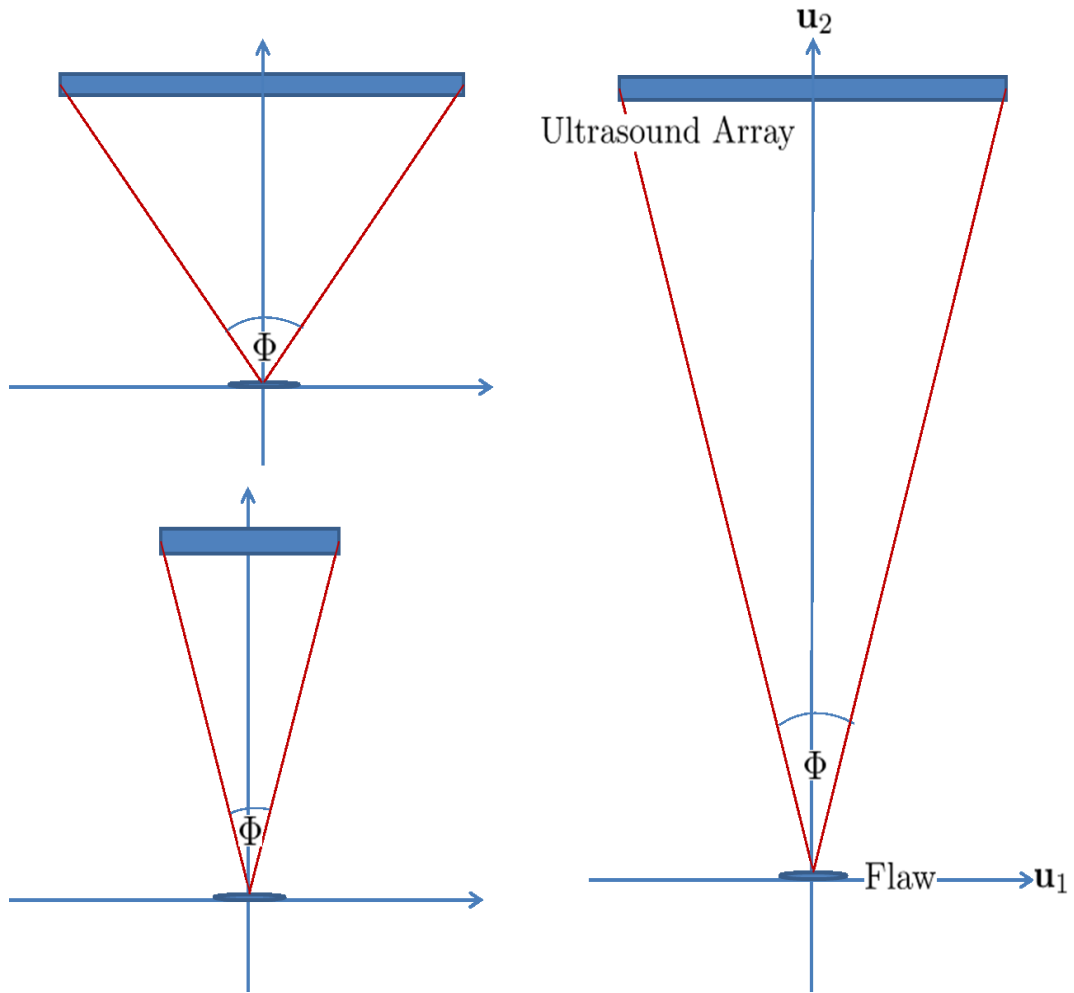


Figure 3.8: Schematic of linear array set up with varying aperture length and distance from the defect. Here the angle between the transmitted and received direction must be smaller than Φ .

3.4 A Model-Based Crack Sizing Algorithm

Work has previously been carried out by Zhang et al [41] on the extraction of key parameters (i.e. crack length and orientation) from scattering matrices for small crack-like defects. By empirical means, they showed that the half-width,

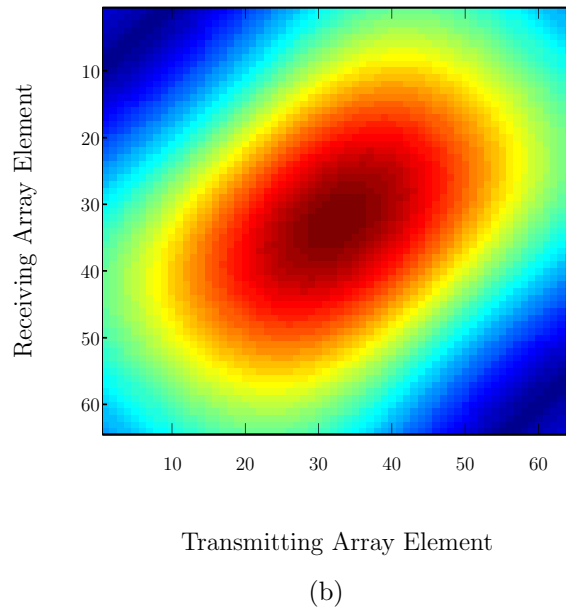
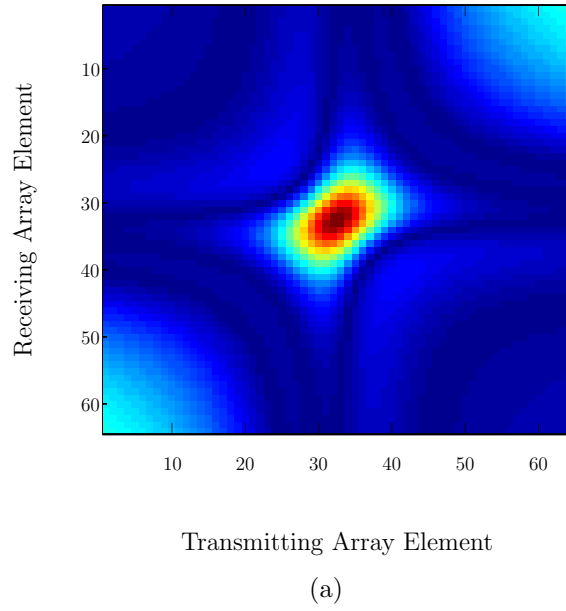


Figure 3.9: Scattering matrices for a crack of length 5mm and orientation 0° , inspected by the linear array as described in Table 3.1, at a depth of (a)20mm and (b)100mm and measured at $a/\lambda \approx 1.4$

half-maximum (HWHM) of a scattering matrix’s pulse-echo response plot (see Figures 3.10, 3.11 and 3.12) decreased monotonically with crack-length. However, the method became a less effective form of measurement for values of $a/\lambda > 2$. One disadvantage of using the HWHM is that it is affected by the transducer response. Work on characterising the field emitted and received by the transducer is discussed in [99, 100] and the scattered wave from the flaw can, in principle, be recovered by deconvolving the function describing the transducer effects from the received signal. This increases the consonance of the HWHM in relation to the flaw’s scattering profile. However, this complication can be negated completely by concentrating on the zeros of the pulse-echo response as these are independent of the transducer effects. The crack-sizing algorithms as developed and discussed below in Sections 3.4.1 and 3.4.2 are based on this idea and, in contrast to the work in [41], do not rely on empirically attained correlations but instead are derived analytically.

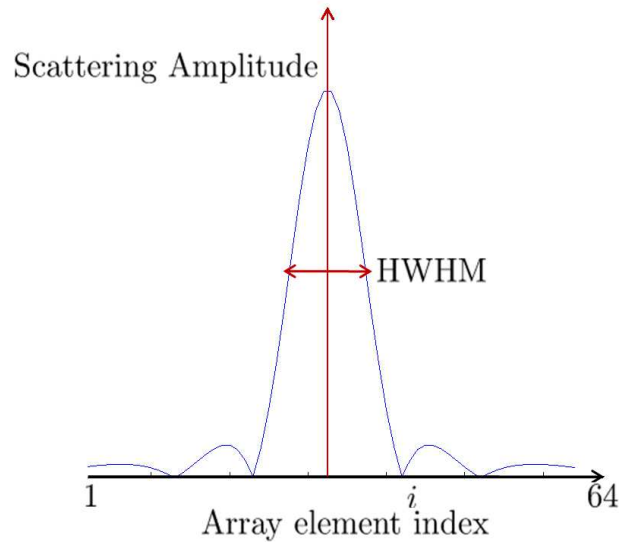


Figure 3.10: Plot of the pulse-echo response from a scattering matrix. The half-width at half maximum (HWHM) is shown by the double headed arrow. The zero of interest occurs at array element i as indicated.

3.4.1 The Zero Degree Crack Case

The diagonal elements of a scattering matrix relate to the case where $\mathbf{e}_s = -\mathbf{e}_i$, also known as the pulse-echo response. Figure 3.11 depicts four scattering matrices with the corresponding plots of their pulse-echo response amplitudes shown in Figure 3.12. These scattering matrices differ only in the value of a/λ , where $a = 2a_1$ is the crack length and λ is the wavelength. As the ratio of crack length to wavelength increases, it is observed that the central lobe of the scattering matrix narrows. This narrowing can be measured by the distance between the zeros of the pulse-echo response that lie either side of the global maximum. Due to the symmetry of the pulse-echo response in the case of a 0° orientated crack, only one of these zeros is required, as indicated by index i in Figure 3.10. Note that when using this method with discrete array elements, this zero is replaced by the location of the local minimum in the pulse-echo response, which relates to the i^{th} array element with position x_i , resulting in the transmitted wave unit vector

$$\mathbf{e}_i = \frac{(x_i, r)}{|(x_i, r)|}, \quad (3.5)$$

where r is the distance of the flaw from the array. To derive a formula for the length of the crack we will assume that x_i is a continuous variable. From equation (3.1), it follows that the zero in the pulse-echo response satisfies

$$\sin(k_{P0}|\mathbf{g}^{P:P}|r_e^{P:P}) - k_{P0}|\mathbf{g}^{P:P}|r_e^{P:P} \cos(k_{P0}|\mathbf{g}^{P:P}|r_e^{P:P}) = 0. \quad (3.6)$$

We set

$$M = 2k_{P0} \sqrt{a_1^2(\mathbf{e}_q \cdot \mathbf{u}_1)^2 + a_2^2(\mathbf{e}_q \cdot \mathbf{u}_2)^2}, \quad (3.7)$$

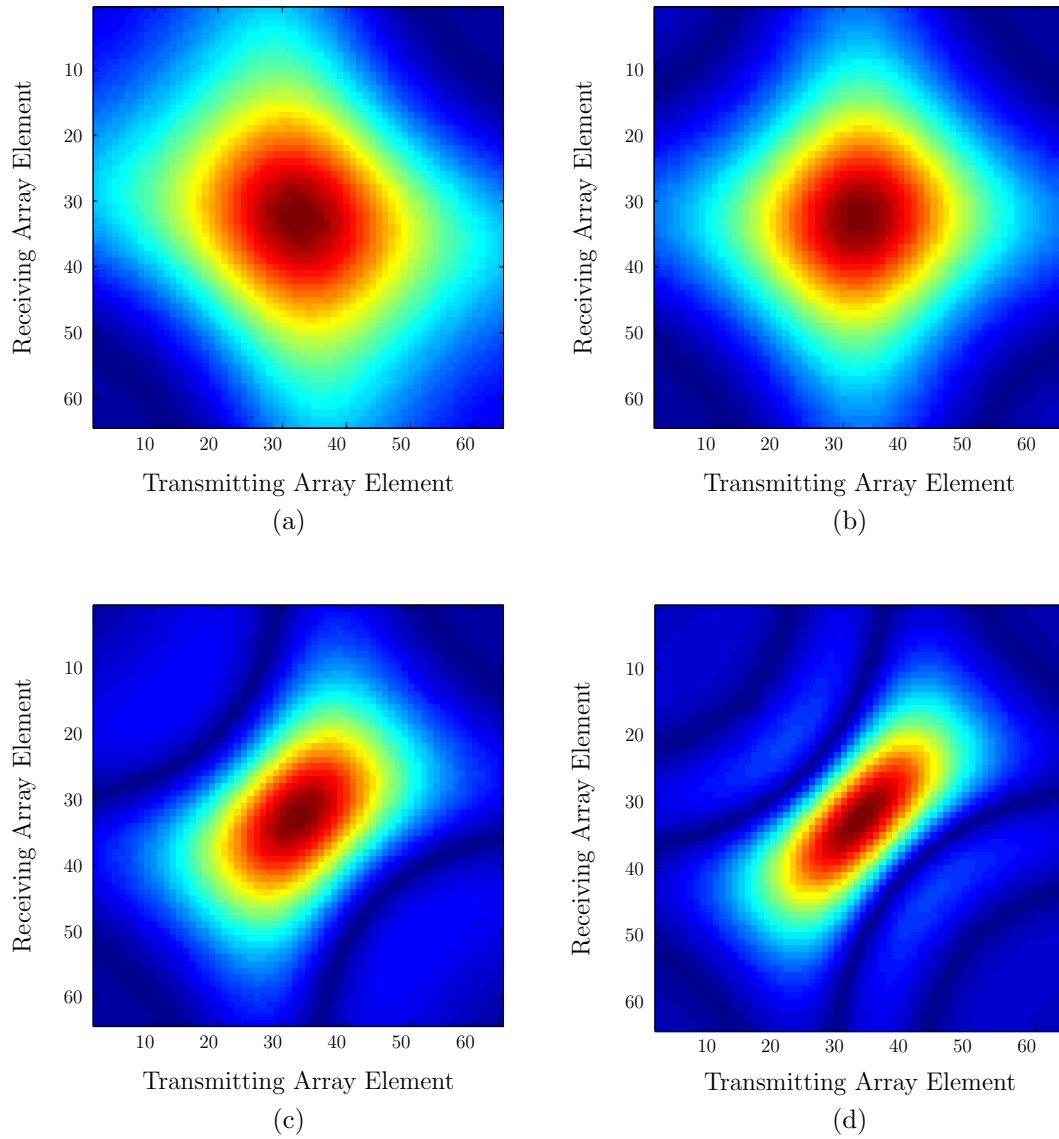


Figure 3.11: Scattering matrices for flaws embedded in a homogeneous medium and inspected by a linear array (both as described in Table 3.1). Only a/λ values vary: (a) 0.8, (b) 1, (c) 1.5 and (d) 2.

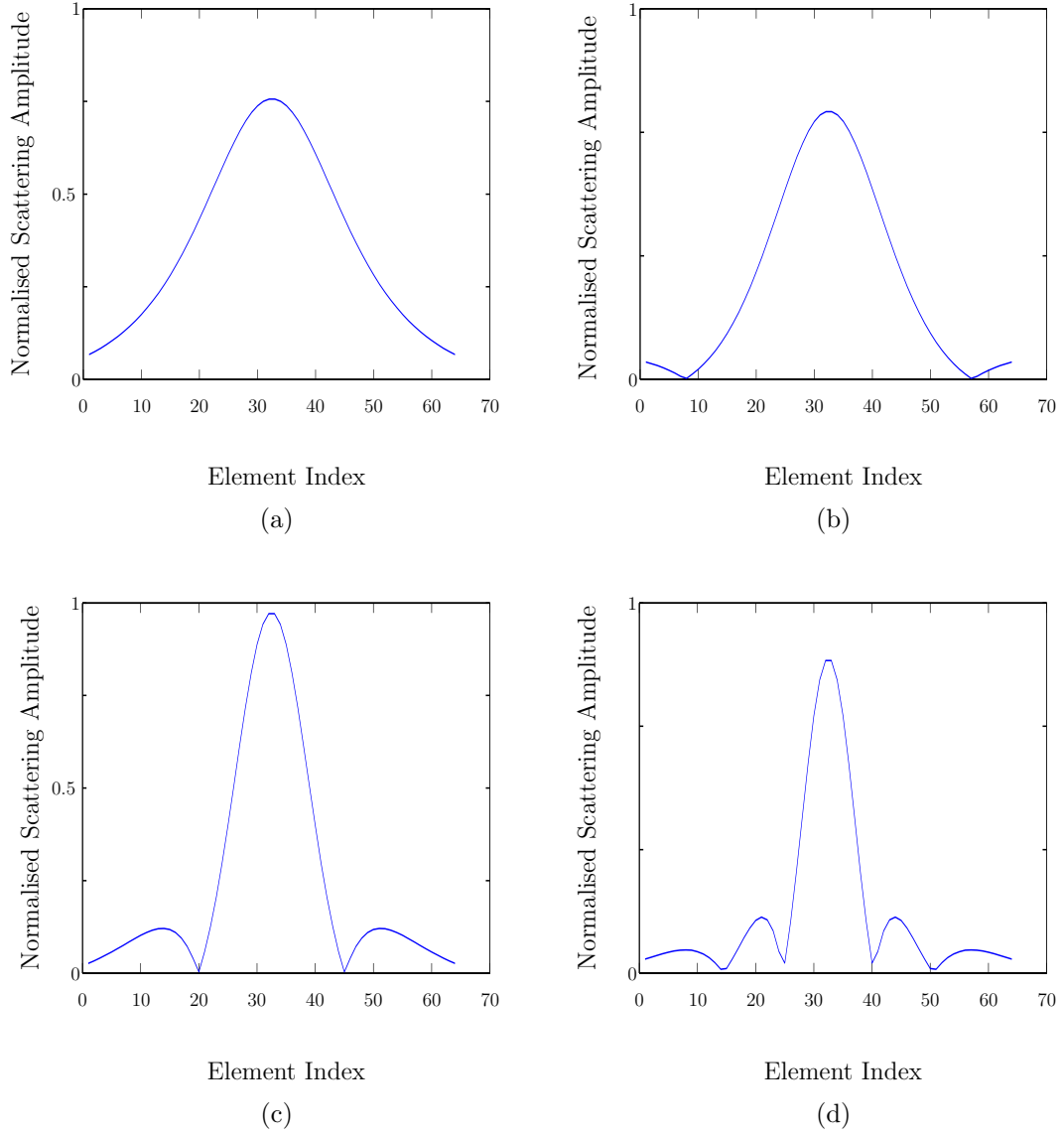


Figure 3.12: Pulse-echo responses (the amplitude down the main diagonal of the scattering matrix) for flaws embedded in a homogeneous medium, 50mm below a linear array of 64 elements with a/λ values of (a) 0.8, (b) 1, (c) 1.5 and (d) 2.

where $M=4.49341$ (the first root of $\tan M = M$), and in the pulse-echo case, $\mathbf{e}_q = \mathbf{e}_i$. Let us begin by examining the case where the crack is orientated at 0° , parallel to the array. Since \mathbf{u}_1 and \mathbf{u}_2 are equal to $[1, 0]^T$ and $[0, 1]^T$ respectively, equation (3.7) can be rewritten

$$M = 2k_{P0} \left(a_1^2 \left(\frac{x_i}{|(x_i, r)|} \right)^2 + a_2^2 \left(\frac{r}{|(x_i, r)|} \right)^2 \right)^{1/2}. \quad (3.8)$$

Substituting $k_{P0} = 2\pi/\lambda$ and rearranging to get an explicit expression for the crack length a gives

$$a = 2a_1 = \frac{2}{x_i} \left(\frac{M^2 \lambda^2}{16\pi^2} (x_i^2 + r^2) - a_2^2 r^2 \right)^{1/2}. \quad (3.9)$$

Equation (3.8) can also be rearranged to give an expression for x_i

$$x_i = r \sqrt{\frac{(M/2\pi)^2 - (2a_2/\lambda)^2}{(2a_1/\lambda)^2 - (M/2\pi)^2}} = r f \left(\frac{a_1}{\lambda}, \frac{a_2}{\lambda} \right). \quad (3.10)$$

This confirms the observation in Figure 3.9 that as the depth of the flaw, r , increases, the width of the main lobe in the scattering matrix increases. Since $a_1 \gg a_2$, equation (3.10) gives rise to the following conditions on a_1 and a_2

$$\frac{2a_1}{\lambda} > \frac{M}{2\pi} > \frac{2a_2}{\lambda}. \quad (3.11)$$

The above condition shows equation (3.9) will only hold for cracks where $a/\lambda > M/2\pi = 0.71529$. Another consideration to be taken into account is the length of the array aperture. To have roots on the pulse-echo diagonal, x_i must fall within the limits of the aperture. Let L be the length of the linear array, and let the flaw

be located beneath its centre. From equation (3.10), as the crack size decreases, then x_i increases, as shown in Figure 3.11. So the smallest crack size that can be resolved for a given aperture coincides with $x_i = L/2$. Hence, equation (3.10) gives

$$\frac{L_{min}}{2} = r \sqrt{\frac{(M/2\pi)^2 - (2a_2/\lambda)^2}{(2a_1/\lambda)^2 - (M/2\pi)^2}}. \quad (3.12)$$

That is,

$$\frac{a}{\lambda} = \sqrt{(M/2\pi)^2 + \frac{(M/2\pi)^2 - (2a_2/\lambda)^2}{(L_{min}/2r)^2}}. \quad (3.13)$$

Allowing $a_2 = 0$, to approximate a crack, the minimum resolvable crack length is given by

$$\left(\frac{a}{\lambda}\right)_{min} = \sqrt{(M/2\pi)^2 + (Mr/\pi L)^2}. \quad (3.14)$$

Once again, it can be observed that as $L_{min} \rightarrow \infty$ then $(a/\lambda)_{min} \rightarrow M/2\pi = 0.71529$, giving the smallest crack size that can be resolved relative to the wavelength. Conversely, as the distance of the flaw from the array increases, so that $r/L \gg 1/2$, then the smallest crack size that can be resolved increases ($a_{min} \rightarrow M\lambda r/\pi L$), since, as can be seen in Figure 3.9, the width of the main lobe in the scattering matrix widens. This can then be compensated for by decreasing the wavelength to narrow this lobe as per Figure 3.11. It should be borne in mind however that there is no wave attenuation in the above model and this method is based on the scattering wave coefficient rather than the scattering wave amplitude received by the array.

Equations (3.13) and (3.14) provide a measure of resolution of the crack-sizing algorithm and produce a lower bound on the smallest resolvable crack size dependent on wavelength, array aperture and flaw depth. However, standard lateral resolution is measured by the smallest distance, d , at which two points can be

identified as being individual. In the case of the crack-sizing algorithm, this is reliant on the minimum distance that two local maxima (arising from two flaws positioned at a distance d from each other) can get without appearing to merge into one (see Figure 3.13). As can be seen, this minimum distance is given by the difference $d = x_1 - x_2$ between the innermost zeros of the pulse-echo response. This can be calculated via equation (3.10) for the case where the flaw is orientated parallel to the array, so $d = 2x_i$.

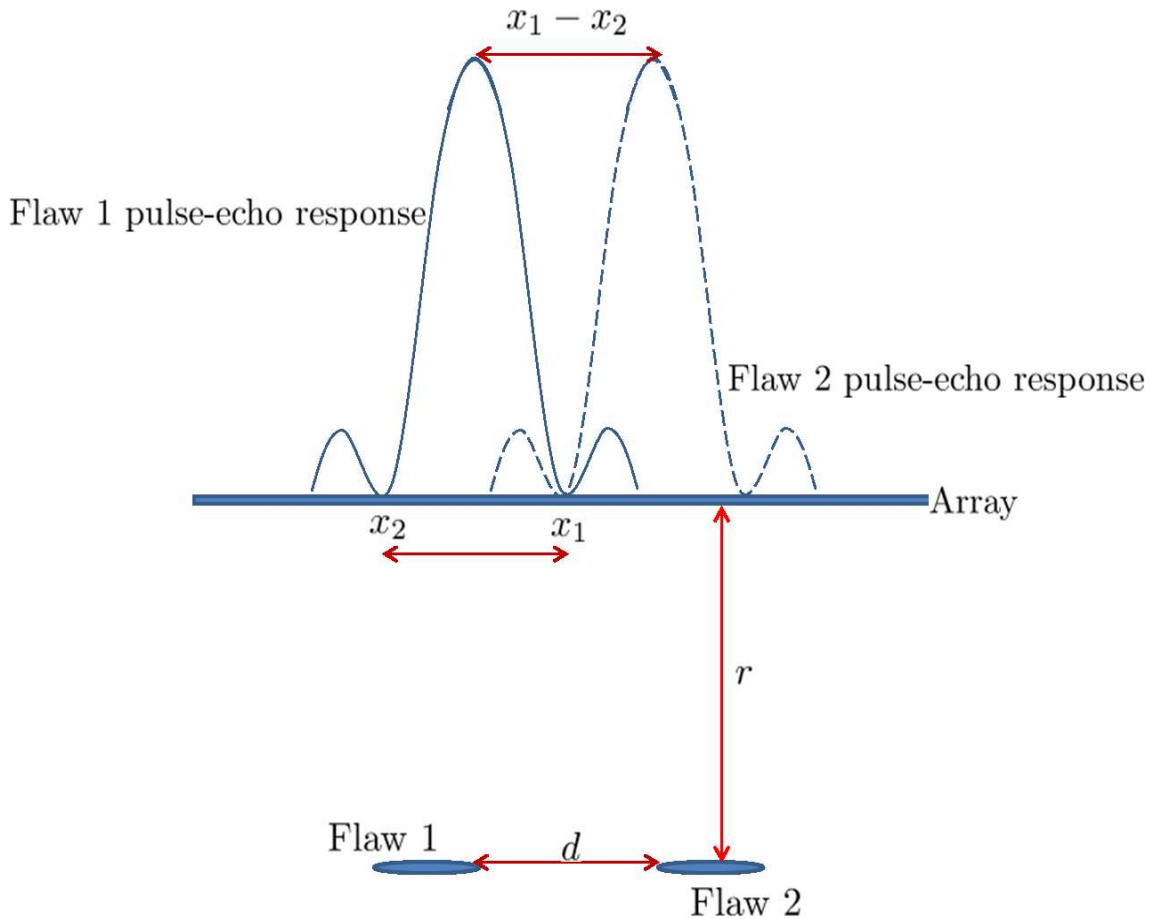


Figure 3.13: Schematic showing two flaws at a distance d from each other. The array receives a pulse-echo response from each flaw. The closest the flaws can get to each other without losing the location of either pulse-echo response curve's zero is $x_1 - x_2 = d$.

Figure 3.14 demonstrates the effects of flaw depth, r , and wavelength, λ , on the resolution of the crack-sizing algorithm for a crack of length 5mm. Plot (a) confirms that as the distance of the flaw from the array increases, the resolution decreases. This is in keeping with the results in Section 3.3 and Figure 3.9 where it was observed that as the flaw depth increased, the angle of observation narrowed and less of the scattering profile was captured. Plot (b) exhibits the effects of increasing λ . It can be seen that as λ increases, the resolution worsens. Referring back to Section 3.4 and Figure 3.11, it can be noted that a decrease in λ allows for more information to be captured within the scattering matrix.

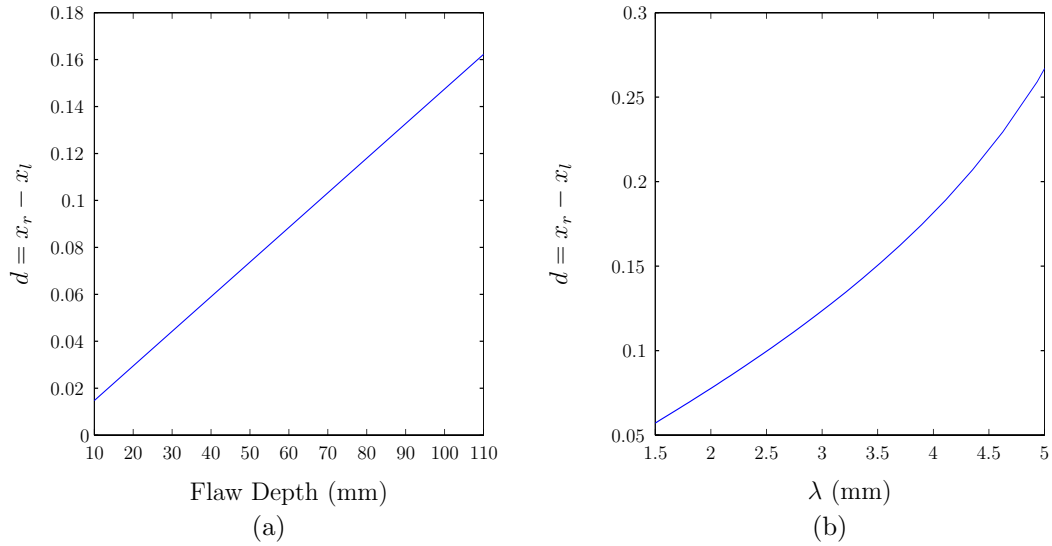


Figure 3.14: Plots showing the minimum resolvable distance between two identical cracks as different model parameters are explored: (a) Flaw depth (r) and (b) wavelength (λ).

Although the trends observed in Figure 3.14 are qualitatively correct, quantitatively, d is comparably large to the wavelength λ , resulting in what appears to be a relatively poor resolution of the method. However, referring back to equation (3.10) and Figure 3.11, it is apparent that the width of the central lobe of our

scattering matrix (and hence the resolution) is dependent on the crack length a . Evidently, this is not a factor when studying the point spread function of point scatterers and the resolution should only be dependent on the wavelength, λ , and the flaw depth (r), as seen in equation (3.14). Hence, although this standard measure of lateral resolution is useful in demonstrating the effects of varying model parameters, the resolution given by (3.14) is more meaningful in the analysis of the method's abilities and limitations.

3.4.2 The Effect of Crack Orientation on Crack Sizing

In this section, the crack is now orientated so that the array and the vector \mathbf{u}_1 are no longer parallel. Let the crack now be rotated by an angle θ in the anti-clockwise direction. Hence

$$\mathbf{u}_1 = \begin{pmatrix} \cos \theta & -\sin \theta \\ \sin \theta & \cos \theta \end{pmatrix} \begin{pmatrix} 1 \\ 0 \end{pmatrix} = \begin{pmatrix} \cos(\theta) \\ \sin(\theta) \end{pmatrix}$$

and

$$\mathbf{u}_2 = \begin{pmatrix} \cos \theta & -\sin \theta \\ \sin \theta & \cos \theta \end{pmatrix} \begin{pmatrix} 0 \\ 1 \end{pmatrix} = \begin{pmatrix} -\sin \theta \\ \cos \theta \end{pmatrix}.$$

The new algorithm remains dependent on the pulse-echo response values and so it still holds that $\mathbf{e}_q = \mathbf{e}_i$, with \mathbf{e}_i as set in equation (3.5). Relating the values of

x_i and r to the angle ϕ as in Figure 3.15, then

$$\begin{aligned}
(\mathbf{e}_q \cdot \mathbf{u}_1) &= \frac{(x_i, r)}{|(x_i, r)|} \cdot (\cos \theta, \sin \theta)^T \\
&= \sin \phi \cos \theta + \cos \phi \sin \theta \\
&= \sin(\phi + \theta).
\end{aligned} \tag{3.15}$$

Similarly,

$$(\mathbf{e}_q \cdot \mathbf{u}_2) = \cos(\phi + \theta). \tag{3.16}$$

It follows then, from equation (3.7), that

$$M = \frac{4\pi}{\lambda} \sqrt{a_1^2 \sin^2(\phi + \theta) + a_2^2 \cos^2(\phi + \theta)} \tag{3.17}$$

which results in an expression for the cracklength

$$a = \sqrt{\frac{M^2 \lambda^2}{4\pi^2} \operatorname{cosec}^2(\phi + \theta) - 4a_2^2 \cot^2(\phi + \theta)}. \tag{3.18}$$

However, there are now two unknowns, a and θ . The introduction of the crack orientation angle θ calls for the use of the two innermost roots, as these describe the width and location of the main lobe of the scattering matrix. These relate to element positions x_1 and x_2 , which translate to the angles ϕ_1 and ϕ_2 as in shown Figure 3.15. Equation (3.18) can then be used to give

$$\frac{M^2 \lambda^2}{16\pi^2} \operatorname{cosec}^2(\phi_1 + \theta) - a_2^2 \cot^2(\phi_1 + \theta) = \frac{M^2 \lambda^2}{16\pi^2} \operatorname{cosec}^2(\phi_2 + \theta) - a_2^2 \cot^2(\phi_2 + \theta) \tag{3.19}$$

which can be solved for θ . Having calculated the crack orientation, it is then possible to substitute this value into equation (3.18) and retrieve the crack length. Once

again, it is also possible to draw conclusions on the minimum aperture required for the algorithm to succeed. As the crack rotates from 0° to 90° , anti-clockwise, it is apparent that the array must be moved to the left in order to capture two zeros along the pulse-echo response. Referring to Figure 3.15, the locations of the first and last elements of the shortest suitable array can be calculated as $x_i = r \tan(\phi_i)$. An exact value for ϕ_i can be calculated via equation (3.18)

$$\phi_i = \pm \sin^{-1} \left(\sqrt{\frac{M^2 \lambda^2 - 16\pi^2 a_2^2}{16\pi^2 (a_1^2 - a_2^2)}} \right) - \theta \quad (3.20)$$

where the negative branch gives ϕ_2 and the positive branch relates to ϕ_1 . The minimum aperture length required is then given by

$$L_{min} = r |\tan(\phi_1) - \tan(\phi_2)|. \quad (3.21)$$

3.5 The Error Manifested in the Crack-Sizing Formulae due to the Array Pitch

As seen, the formulae presented in Section 3.4 are derived from the Born Approximation. Although a widely accepted model for scattering in elastic media, it is nonetheless an approximation. As such, it is reasonable to assume that equations (3.9) and (3.18) will give rise to an error when compared to experimental data. The implementation of this crack-sizing algorithm is dependent on the estimation of experimental parameters such as the array element pitch and the wavelength. It is of particular interest to analyse the maximum errors that can occur due to

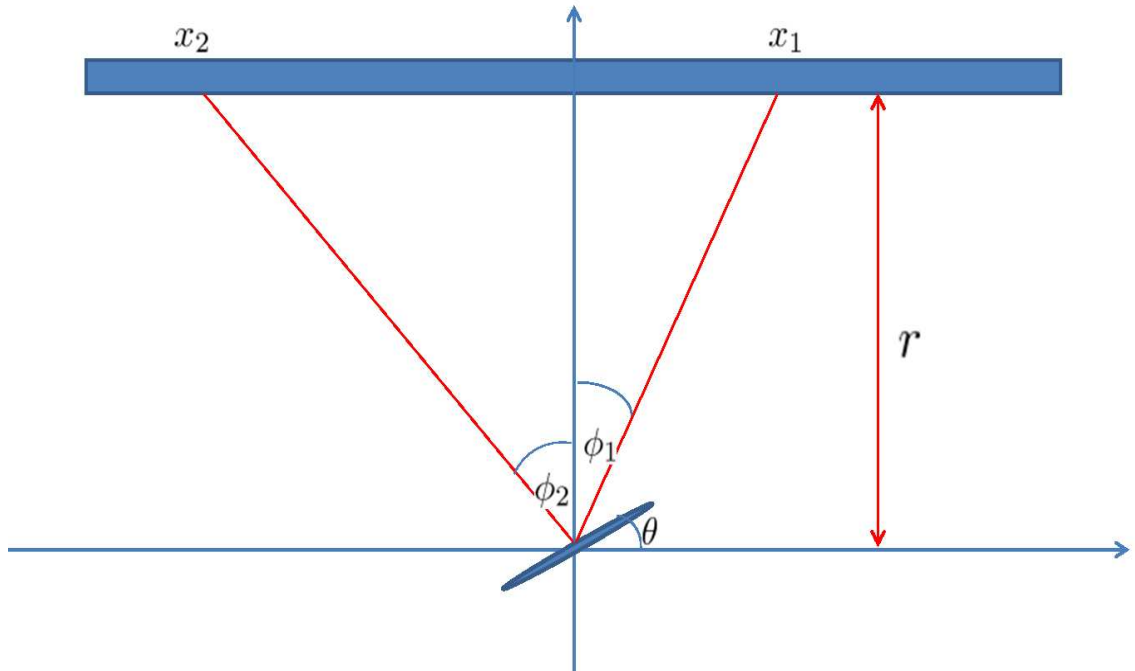


Figure 3.15: Diagram depicting the general situation where the crack is orientated at an angle θ relative to the x -axis. The variables x_1 and x_2 are the element locations corresponding to the innermost zero of the pulse-echo response and ϕ_1 and ϕ_2 are the corresponding angles.

the discretisation of x arising from the array design. Since the ultrasonic array is composed of a discrete set of elements, positioned at regular intervals called the pitch p , then the value of x_i that is extracted from the scattering matrix will only be approximate due to this discretisation. The value of the crack size that is then predicted using this approximate value of x_i is denoted by a^D . The error due to this discretisation (ϵ^D) is then given by the difference between the known a and a^D . In the worst case this numerically extracted value for x_i will be out by at most one pitch (see Figure 3.16). Hence, we can analyse our formulae for the crack length and arrive at an expression for the maximum error ϵ^M . The resulting expression for the error can be further approximated to provide an analytical form that shows its dependency on the model parameters. This error is then denoted ϵ^A .

3.5.1 The Zero Degree Crack Case

Assuming the conditions as laid out in equations (3.11) are met, then equation (3.9) provides an explicit expression for the crack length a given data from a scattering matrix. However, in practice, an error in discretisation (manifested in the array pitch) is observed as it is necessary to round to the nearest array element at location x_i . An approximation of the crack length when the error in x_i is one

pitch p is given by

$$\begin{aligned}
a^M &= \frac{2}{x_i + p} \left(\frac{M^2 \lambda^2}{16\pi^2} ((x_i + p)^2 + r^2) - a_2^2 r^2 \right)^{1/2} \\
&= \frac{2}{x_i} \left(1 - \frac{p}{x_i} \right) \left(\frac{M^2 \lambda^2}{16\pi^2} (x_i^2 + 2x_i p + r^2) - a_2^2 r^2 \right)^{1/2} + \mathcal{O} \left(\frac{p^2}{x_i^2} \right) \\
&= \frac{2}{x_i} \left(1 - \frac{p}{x_i} \right) \left[\left(\frac{M^2 \lambda^2}{16\pi^2} (x_i^2 + r^2) - a_2^2 r^2 \right) \left(1 + \frac{(M^2 \lambda^2 / 8\pi^2) x_i p}{(M^2 \lambda^2 / 16\pi^2) (x_i^2 + r^2) - a_2^2 r^2} \right) \right]^{1/2} \\
&\quad + \mathcal{O} \left(\frac{p^2}{x_i^2} \right) \\
&= a \left(1 - \frac{p}{x_i} \right) \left(1 + \frac{M^2 \lambda^2 p}{4\pi^2 a^2 x_i} \right) + \mathcal{O} \left(\frac{p^2}{a^3 x_i^2} \right) \\
&= a^A + \mathcal{O} \left(\frac{p^2}{a^3 x_i^2} \right). \tag{3.22}
\end{aligned}$$

Hence, the maximum absolute error caused by discretisation via the array pitch can be written

$$\begin{aligned}
\epsilon^M &= |a - a^M| = \left| -\frac{pa}{x_i} + a \left(1 - \frac{p}{x_i} \right) \left(\frac{M^2 \lambda^2 p}{4\pi^2 a^2 x_i} \right) \right| + \mathcal{O} \left(\frac{p^2}{a^3 x_i^2} \right) \\
&= \epsilon^A + \mathcal{O} \left(\frac{p^2}{a^3 x_i^2} \right). \tag{3.23}
\end{aligned}$$

Alternatively, letting $\hat{p} = p/r$ and substituting in the formula for x_i as given in equation (3.10), this error can be written as

$$\hat{\epsilon}^A = \left| -\frac{\hat{p}}{f\left(\frac{a_1}{\lambda}, \frac{a_2}{\lambda}\right)} \left(\frac{a}{\lambda}\right) + \frac{a}{\lambda} \left(1 - \frac{\hat{p}}{f\left(\frac{a_1}{\lambda}, \frac{a_2}{\lambda}\right)} \right) \left(\frac{M^2 \hat{p}}{4\pi^2 \left(\frac{a}{\lambda}\right)^2 f\left(\frac{a_1}{\lambda}, \frac{a_2}{\lambda}\right)} \right) \right|. \tag{3.24}$$

The results are displayed in Figure 3.17. The maximum error estimate (ϵ^M) provides a clear upper bound on the actual error that incurs (ϵ^D) when equation (3.9) is used to determine the crack size from a given discrete set of array element positions, x_i . It is also clear that the approximate error ϵ^A provides a reasonable

approximation of this upper bound. From equation (3.24) it is clear that as $\hat{p} \rightarrow 0$, $\epsilon^A \rightarrow 0$, as expected. Unfortunately, zero-error is unobtainable as creating arrays with zero pitch has manufacturing difficulties and in the case of allowing $r \rightarrow \infty$, wave attenuation would prevent the scattered wave registering in the array. Figure 3.17 confirms that any decrease in pitch is beneficial to the accuracy of the algorithm.

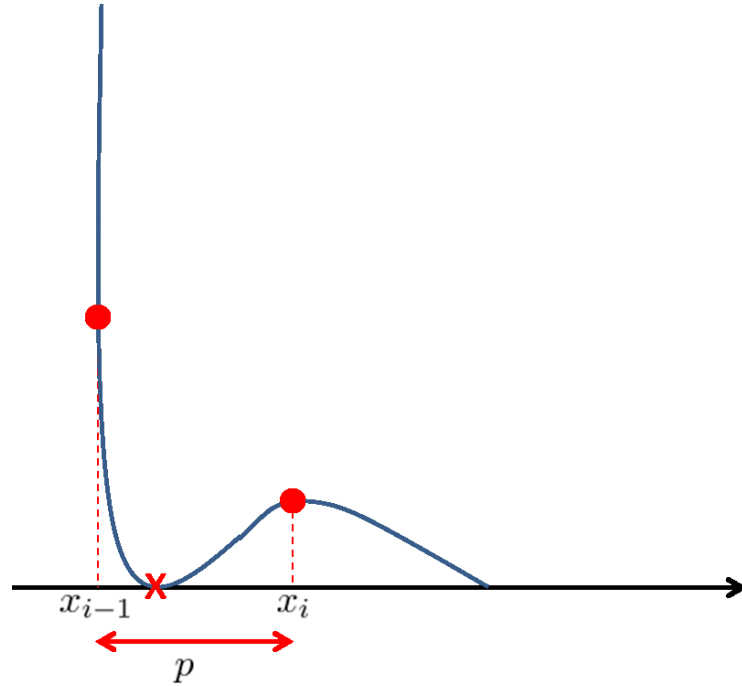


Figure 3.16: A segment of a pulse-echo response curve where the cross indicates the location of the zero. The minimum is taken from a discrete set of points dictated by the array element locations. This diagram demonstrates that the minimum value of this discrete set, which occurs at x_i , may not correspond to the element closest to the exact location of the zero and can in fact be as much as pitch p away.

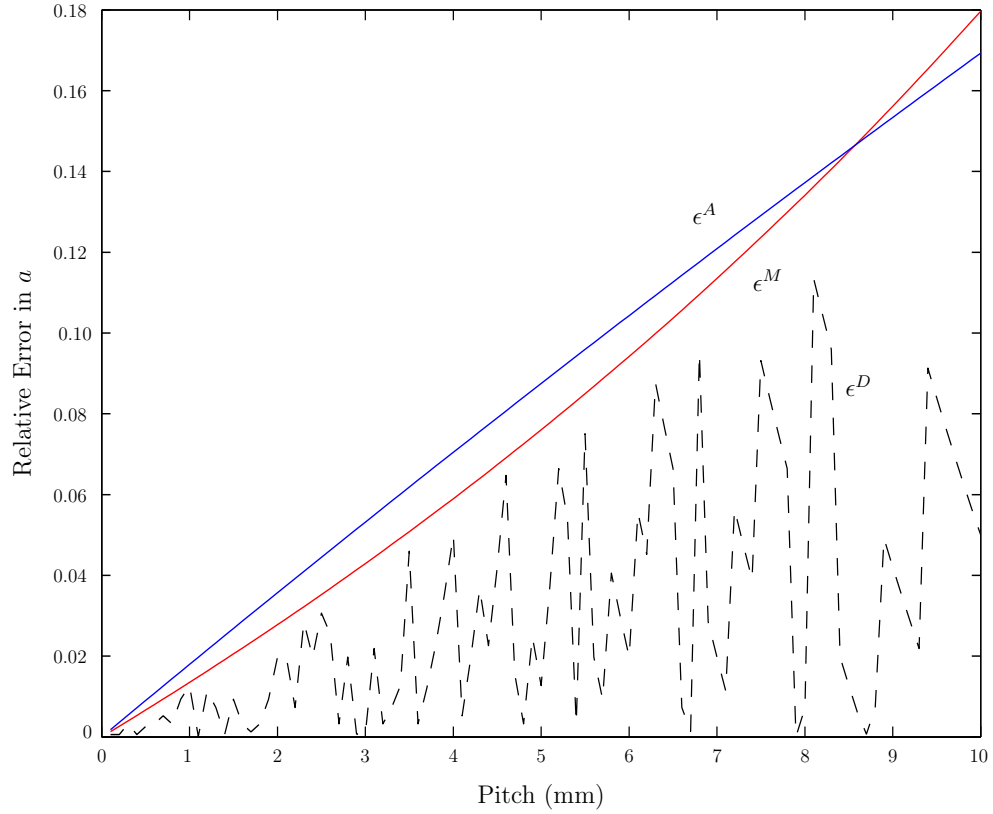


Figure 3.17: Error in the crack size measured versus the pitch p for the zero degree crack sizing algorithm. Equation (3.23) provides ϵ_M (red) and ϵ_A (blue). The numerically calculated error ϵ_D , obtained using the zero degree crack sizing algorithm with the estimated value of x_i taken from the discrete set of points dictated by the array element locations, is plotted in black.

3.5.2 General Crack Orientation

Repeating the error analysis as in Section 3.4.1, it is possible to explore the limitations of the crack-sizing algorithm for cracks of non-zero orientation. However, since the discretisation is dependent on the array pitch p , it is more intuitive to implement this error analysis in terms of element location x_i , rather than angle ϕ . From equation (3.17)

$$\begin{aligned}
 M^2 &= \frac{16\pi^2}{\lambda^2} (a_1^2(\sin \phi \cos \theta + \cos \phi \sin \theta)^2 + a_2^2(\cos \phi \cos \theta - \sin \phi \sin \theta)^2) \\
 &= \frac{16\pi^2 a_1^2}{\lambda^2} \left(\frac{x_i}{\sqrt{x_i^2 + r^2}} \cdot \cos \theta + \frac{r}{\sqrt{x_i^2 + r^2}} \cdot \sin \theta \right)^2 \\
 &\quad + \frac{16\pi^2 a_2^2}{\lambda^2} \left(\frac{r}{\sqrt{x_i^2 + r^2}} \cdot \cos \theta - \frac{x_i}{\sqrt{x_i^2 + r^2}} \cdot \sin \theta \right)^2. \tag{3.25}
 \end{aligned}$$

Rearranging for a gives

$$a = 2a_1 = \frac{2\sqrt{(M^2\lambda^2/16\pi^2)(x_i^2 + r^2) - a_2^2(r \cos \theta - x_i \sin \theta)^2}}{(x_i \cos \theta + r \sin \theta)}. \tag{3.26}$$

Note that by substituting in $\theta = 0$, recreating the 0° orientated crack case, equation (3.9) is recovered. As with the zero degree case, it is possible to calculate the maximum error due to discretisation via the array pitch p . From equation (3.26) an approximation for the estimated crack length when the error in x_i is one pitch

is given by

$$\begin{aligned}
\hat{a}^M &= \frac{\sqrt{M^2((x_i + p)^2 + r^2) - 16\pi^2\hat{a}_2^2(r \cos \theta - (x_i + p) \sin \theta)^2}}{2\pi((x_i + p) \cos \theta + r \sin \theta)} \\
&= (M^2(x_i^2 + r^2) - 16\pi^2\hat{a}_2^2(r \cos \theta - x_i \sin \theta)^2 \\
&\quad + M^2(2x_i p + p^2) - 16\pi^2\hat{a}_2^2 p \sin \theta (2x_i \sin \theta + p \sin \theta - 2r \cos \theta))^{1/2} \\
&\quad \times (2\pi(x_i \cos \theta + r \sin \theta) + 2\pi p \cos \theta)^{-1}. \tag{3.27}
\end{aligned}$$

Letting $q = M^2(x_i^2 + r^2) - 16\pi^2\hat{a}_2^2(r \cos \theta - x_i \sin \theta)^2$, $s = M^2(2x_i p + p^2) - 16\pi^2\hat{a}_2^2 p \sin \theta (2x_i \sin \theta + p \sin \theta - 2r \cos \theta)$, $v = 2\pi(x_i \cos \theta + r \sin \theta)$ and $w = 2\pi p \cos \theta$, this can be rewritten

$$\begin{aligned}
\hat{a}^M &= (q + s)^{1/2} (v + w)^{-1} \\
&= q^{1/2} \left(1 + \frac{s}{q}\right)^{1/2} v^{-1} \left(1 + \frac{w}{v}\right)^{-1}. \tag{3.28}
\end{aligned}$$

Now from (3.26)

$$a = \frac{2\lambda}{4\pi} q^{1/2} \left(\frac{v}{2\pi}\right)^{-1}, \tag{3.29}$$

and so it follows that

$$\hat{a} = \frac{a}{\lambda} = q^{1/2} v^{-1}. \tag{3.30}$$

So, by Taylor expanding,

$$\begin{aligned}
\hat{a}^M &= \hat{a} \left(1 + \frac{s}{2q} + \mathcal{O}\left(\frac{s^2}{q^2}\right) \right) \left(1 - \frac{w}{v} \right) + \mathcal{O}\left(\frac{w^2}{v^2}\right) \\
&= \hat{a} \left(1 + \frac{s}{2q} \right) \left(1 - \frac{w}{v} \right) + \mathcal{O}\left(\max \left\{ \hat{a} \left(\frac{s}{q} \right)^2, \hat{a} \left(\frac{w}{v} \right)^2 \right\} \right) \\
&= \hat{a} \left(1 + \frac{s}{2q} - \frac{w}{v} - \frac{sw}{2qv} \right) + \mathcal{O}(e_1) \\
&= \hat{a} \left(1 + \frac{s}{2q} - \frac{w}{v} \right) + \mathcal{O}\left(\frac{\hat{a}sw}{qv}\right), \tag{3.31}
\end{aligned}$$

where $e_1 = \max \left\{ \hat{a} \left(\frac{s}{q} \right)^2, \hat{a} \left(\frac{w}{v} \right)^2 \right\}$. The maximum error can thus be written

$$\begin{aligned}
\epsilon^M &= |\hat{a} - \hat{a}^M| \\
&= \left| \frac{\hat{a}s}{2q} - \frac{\hat{a}w}{v} \right| + \mathcal{O}\left(\frac{\hat{a}sw}{qv}\right) \\
&= \epsilon^A + \mathcal{O}\left(\frac{\hat{a}sw}{qv}\right). \tag{3.32}
\end{aligned}$$

Expressing ϵ^A explicitly gives

$$\epsilon^A = \left| \frac{M^2(2x_i p + p^2) - 16\pi^2 \hat{a}_2^2 p \sin \theta (2x_i \sin \theta + p \sin \theta - 2r \cos \theta)}{8\pi^2 \hat{a} (x_i \cos \theta + r \sin \theta)^2} - \frac{\hat{a} p \cos \theta}{x_i \cos \theta + r \sin \theta} \right|. \tag{3.33}$$

It can be seen from equation (3.33) that allowing $p \rightarrow 0$ it follows that $\epsilon^A \rightarrow 0$, as expected. Figures 3.18 and 3.19 demonstrate the effect of an increasing array pitch on the maximum possible error, ϵ^M (red), the analytical approximation of the maximum error, ϵ^A (blue) and the actual error incurred ϵ^D (black).

Having studied the effect of discretisation via the array pitch on the algorithm's

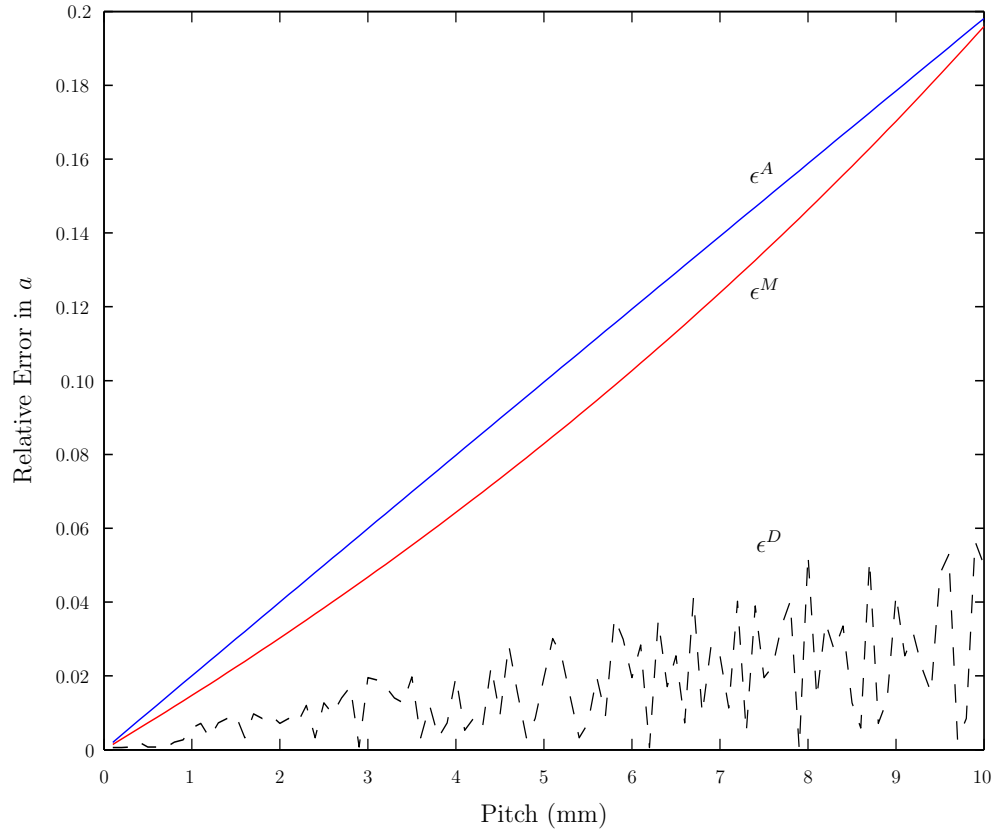


Figure 3.18: Relative error in the crack size measured versus the pitch p for the multi-orientation crack sizing algorithm for a crack with $a/\lambda \approx 1$ and 0° orientation. Equation (3.27) provides ϵ_M (red) and equation gives (3.33) ϵ_A (blue). The actual error, ϵ_D (black), is obtained using the multi-orientation crack sizing algorithm with the estimated value of x_i taken from the discrete set of points dictated by the array element locations.

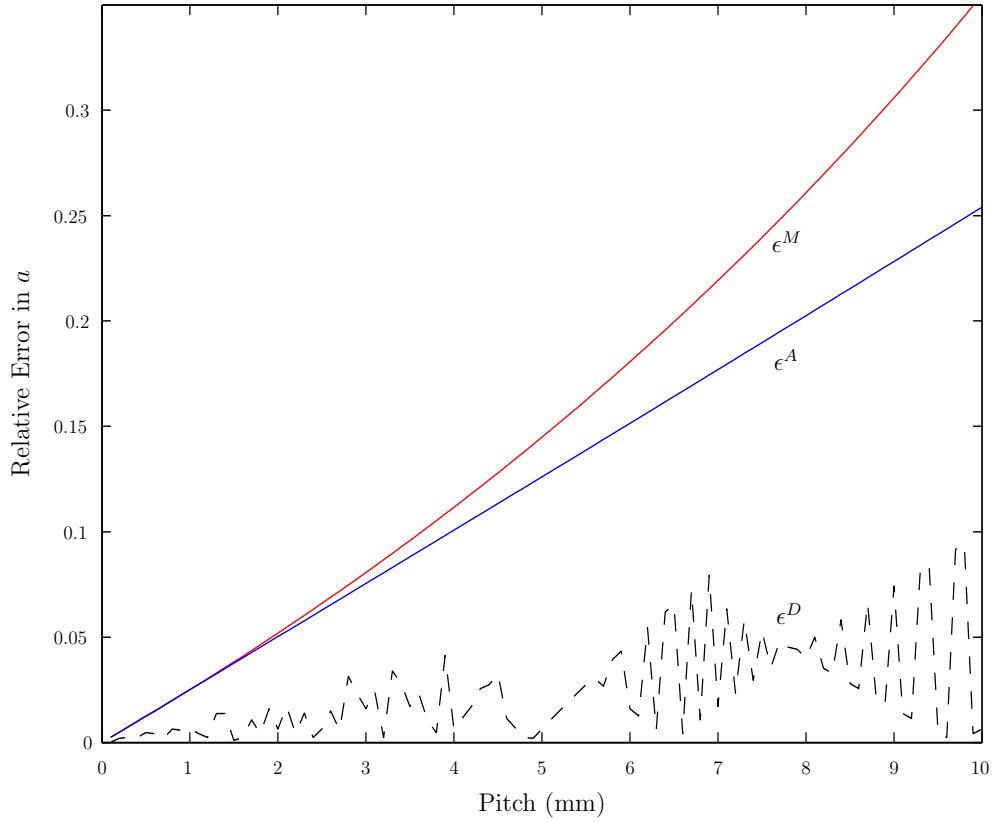


Figure 3.19: Relative error in the crack size measured versus the pitch p for the multi-orientation crack sizing algorithm for a crack with $a/\lambda \approx 1$ and 30° orientation. Equation (3.27) provides ϵ_M (red) and equation (3.33) gives ϵ_A (blue). The actual error, ϵ_D (black), is obtained using the multi-orientation crack sizing algorithm with the estimated value of x_i taken from the discrete set of points dictated by the array element locations. The known value of θ has been used to demonstrate the effects of the discretisation due to the array element pitch on the error.

accuracy, we will now look at the effect of an error in the estimated orientation of the crack. Using values varying by up to 10° from the known value of θ , and inputting the exact value for ϕ (to discount the effects of discretisation), equation (3.18) was calculated. Figure 3.20 shows the results, plotting the relative error in a against the crack orientation θ , for a 5mm crack of orientations 0° and 30° in plots (a) and (b) respectively. From these plots, it can be observed that for the crack size to remain within a 5% error interval, θ must not be out by more than approximately 2.5° . Plots (c) and (d) show the absolute error in θ calculated via equation (3.19) as the the pitch p increases. It can be observed that, to remain within 2.5° of the known orientation $\theta = 0^\circ$ (plot (c)), a pitch of up to and including 10mm (for an array of length 500mm with a flaw at a depth of 50mm) can be used. In the case where $\theta = 30^\circ$ (plot (d)), the pitch can be increased to approximately 5.5mm. In both cases, equation (3.19) provides a suitable estimate of θ over the range of array pitches usually used within the NDT industry (0.5mm - 2mm) and hence is viable for the purpose of our multi-orientation crack-sizing algorithm.

3.5.3 Sensitivity

To assess the potential for further application of the crack-sizing algorithm shown in Section 3.4.2, it is interesting to examine its sensitivity to the model parameters.

To analyse this, from equation (3.18), let

$$\hat{a} = \frac{a}{\lambda} = \sqrt{\frac{M^2}{4\pi^2} \operatorname{cosec}^2(\phi + \theta) - 4 \left(\frac{a_2}{\lambda}\right)^2 \cot^2(\phi + \theta)} = f(\phi, \theta). \quad (3.34)$$

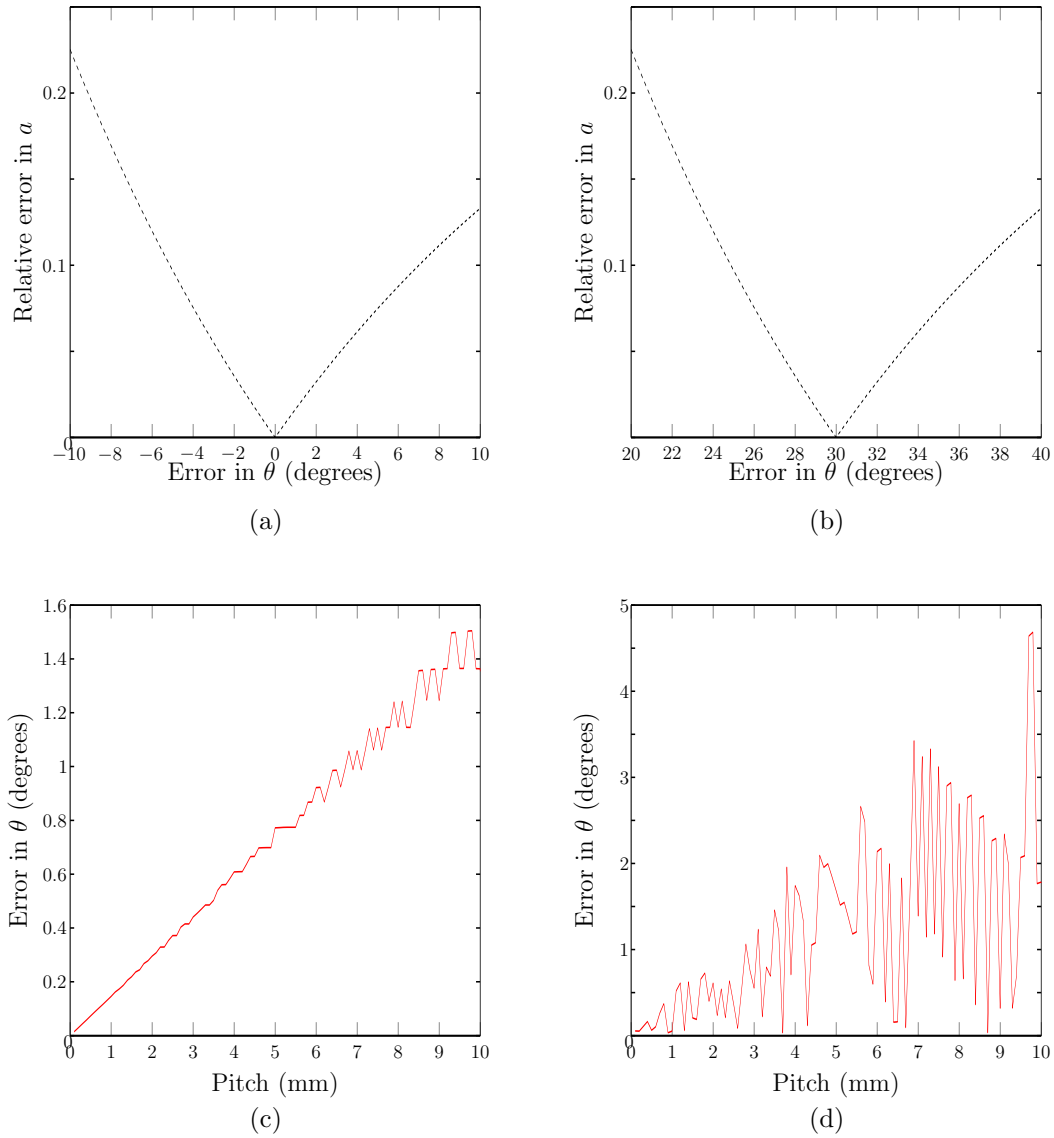


Figure 3.20: By inserting the exact angle ϕ_i as calculated in equation (3.20) into the crack sizing formula, equation (3.18), and keeping all other parameters constant, it is possible to vary θ and analyse the effect on the estimate for the crack size a . The results for cracks orientated at 0° and 30° are plotted in (a) and (b). Plots (c) and (d) track the absolute error in the estimation of θ , calculated via equation (3.19), as the pitch increases for cracks orientated at 0° and 30° , respectively. All of the plots shown are plotted for the case where $a/\lambda \approx 1$.

Then

$$\begin{aligned}
\frac{\partial f}{\partial \phi} = \frac{\partial f}{\partial \theta} &= \left(\frac{M^2}{16\pi^2} \operatorname{cosec}^2(\phi + \theta) - \hat{a}_2^2 \cot^2(\phi + \theta) \right)^{-1/2} \\
&\times \frac{M^2}{16\pi^2} (-2 \operatorname{cosec}^2(\phi + \theta) \cot(\phi + \theta)) + 2\hat{a}_2^2 \operatorname{cosec}^2(\phi + \theta) \cot(\phi + \theta) \\
&= \frac{2 \operatorname{cosec}^2(\phi + \theta) \cot(\phi + \theta) (16\pi^2 \hat{a}_2^2 - M^2)}{4\pi (M^2 \operatorname{cosec}^2(\phi + \theta) - 16\pi^2 \hat{a}_2^2 \cot^2(\phi + \theta))^{1/2}} \\
&= \frac{2 \cot(\phi + \theta) (16\pi^2 \hat{a}_2^2 - M^2)}{4\pi \sin(\phi + \theta) (M^2 - 16\pi^2 \hat{a}_2^2 \cos^2(\phi + \theta))^{1/2}}. \tag{3.35}
\end{aligned}$$

The relative effects of changes in the crack orientation, θ and the estimated angle of reception, ϕ , on the crack size relative to the wavelength, \hat{a} , can be calculated from

$$\frac{\Delta \hat{a}}{\hat{a}} = \frac{\partial f}{\partial \phi} \frac{\phi}{\hat{a}} \frac{\Delta \phi}{\phi} + \frac{\partial f}{\partial \theta} \frac{\theta}{\hat{a}} \frac{\Delta \theta}{\theta}. \tag{3.36}$$

Plotting $(\phi/\hat{a}) \frac{\partial f}{\partial \phi}$ allows for the assessment of the algorithm's sensitivity to the system parameters. Note that the results shown in Figure 3.22 also provide the sensitivity to changes in θ ; as equation (3.35) suggests. Plot (a) shows the sensitivity of the measurement of \hat{a} due to changes in ϕ as \hat{a} changes. It is observed that as the value of \hat{a} increases, the crack sizing algorithm's sensitivity to changes in ϕ decreases. In Section 3.4, Figure 3.11, it was shown that as a/λ increased, the width of the scattering matrices central lobe decreased, and hence, the elements at which the zeros of the pulse-echo response plot reside, were located closer to the vertical. Figure 3.21 demonstrates that the closer the zero of the pulse-echo response is to the vertical, the greater is the change in ϕ between neighbouring array elements and hence, the larger the potential error in the recovered crack size. This is corroborated in plot (b) where it is shown that as ϕ increases, the sensitivity of the crack-sizing algorithm to changes in ϕ decreases.

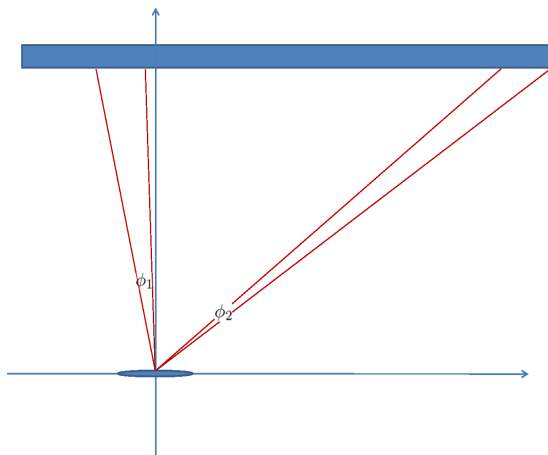


Figure 3.21: Schematic demonstrating that the closer the zero of the pulse-echo response (expressed as angle ϕ_i) is to being vertical the larger is the difference in ϕ between ϕ_i and the angle pertaining to the neighbouring array element.

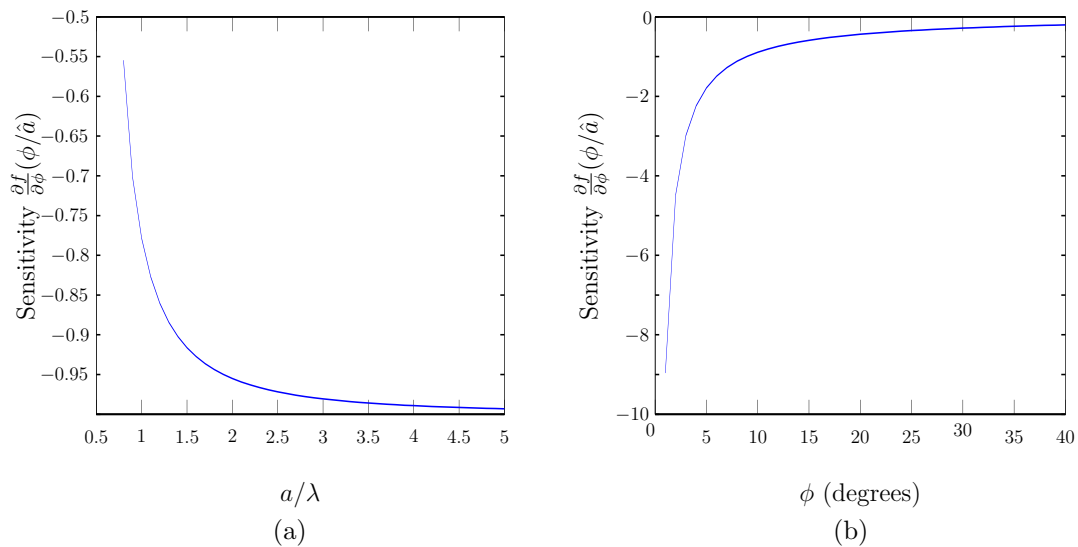


Figure 3.22: Plots of $\frac{\partial f}{\partial \phi}(\phi/\hat{a})$ as (a) a/λ increases and (b) ϕ increases.

3.6 Application of the Model Based Crack Sizing Algorithm to Simulated Data

To corroborate the conclusions drawn from the error analysis of the model based crack sizing algorithm (as derived from the Born Approximation in Section 3.5), the method has been applied to scattering matrices arising from data generated by the simulation of an ultrasound wave scattered by a crack embedded in a homogeneous medium via the finite element method in the software package PZFlex (see Appendix B). Although efforts have been made to recreate the setting of the PZFlex simulation within the Born approximation, it is important to note that each model approximates the physical scattering by a flaw in a different way and so an exact match up between the two is not anticipated. Hence, the application of the model based crack-sizing algorithm to data generated via PZFlex is not expected to achieve the same success. However, regardless of the differences, it is hoped that the conclusions drawn through the analytical error analysis will hold true. Important deviations between the assumptions inherent to the two modelling approaches are listed below.

The Born approximation is a scattering model for volumetric flaws, where a crack-like flaw is approximated by a two-dimensional ellipsoid with a high aspect ratio ($a_1 \gg a_2$). Within the PZFlex software, the domain is meshed with regular square elements and hence the crack is simulated by a rectangular void. Although the material parameters used for the host and defect medium in the Born approximation have been chosen to replicate those found in the PZFlex simulation, the Born approximation is designed as a weak scattering model and hence some accuracy may be lost. Also note that the time domain PZFlex simulation will in-

clude some mode conversion as the pressure wave interacts with the flaw whereas the Born approximation formulation focusses on the scattered pressure wave only. The PZFlex simulation includes wave attenuation while the algorithm as derived in this chapter is based on the scattering coefficient only. The PZFlex data is collected in the time domain and a discrete FFT is required to convert it into a form comparable with the frequency domain scattering matrices of the Born Approximation. In doing so, the continuous spectrum of frequencies is replaced by a discrete set dictated by the value of the time step, Δt . Furthermore, a sinusoidal pulse is simulated as the driving function within the finite element simulation, and hence, there are bounds to the bandwidth of usable frequencies. Figure 3.23 depicts typical scattering matrices and their corresponding pulse-echo responses as generated by the Born Approximation and by the finite-element simulation (see Table B.1 for parameter values), arising from a crack lying parallel to the array ($\theta = 0^\circ$) with a crack length to wavelength ratio of $a/\lambda \approx 2.6$. A reasonable correspondance between the two pulse-echo response plots can be observed. In plot (b), the innermost local minimum at element 25 (or 40) can be used as the approximated zero of the pulse-echo response plot. This is then converted into positional co-ordinates along the linear array (x_i) and substituted into the crack sizing algorithm shown in equation (3.9). Studying the equivalent plot generated by the finite element simulation (plot (d)), the zeros of the pulse-echo are less obvious. This requires another approximation which may further affect the success of the model based algorithm in applications. To do so, the gradient is calculated at the half-maximum and the zero is estimated as the point at which the curve would have met the x -axis had it retained this gradient. Unfortunately this implementation of the method ceases to be immune to the transducer trans-

fer function but, for the purposes of verifying the analytical conclusions made in previous sections, this approach is sufficient.

3.6.1 Effects of an Artificially Increasing Array Pitch

It is possible to vary the array pitch without running further simulations in PZFlex, by taking subsets of the full matrix capture (FMC - see Section 2.1.1) and in doing so, artificially altering the array pitch. Figure 3.24 displays three scattering matrices arising from a finite element simulation (see Table B.1) and all are plotted at the same frequency. In plot (a), only the signals corresponding to odd transmit/receive elements have been retained. This corresponds to an array of approximately the same aperture as that used to generate plot (c) in Figure 3.23, but with half the number of array elements and hence an artificially increased array pitch of $p^* = 4\text{mm}$. Plots (b) and (c) have been generated in the same manner using every third element ($p^* = 6\text{mm}$) and every fourth element ($p^* = 8\text{mm}$), respectively. It has already been shown analytically (Section 3.5), that as the array pitch increases, so does the relative error in the recovered crack size. Plot (d) plots the relative error in the recovered crack size using equation (3.9) against the artificially increasing pitch. The difference in the magnitude of the relative errors seen in this plot and those shown in Figure 3.17, can be attributed to the disparities between the two models as discussed earlier in this Section. However the declining accuracy of the crack sizing algorithm as the pitch increases is a common characteristic and verifies the previously drawn conclusion that as the pitch tends to zero, the relative error (ϵ^D) in the recovered crack size also tends to zero. Note also, that in this case, using the full FMC ($p = 2\text{mm}$), a relative error of $\epsilon^D = 5.5\%$ is incurred and the actual crack length estimate of the

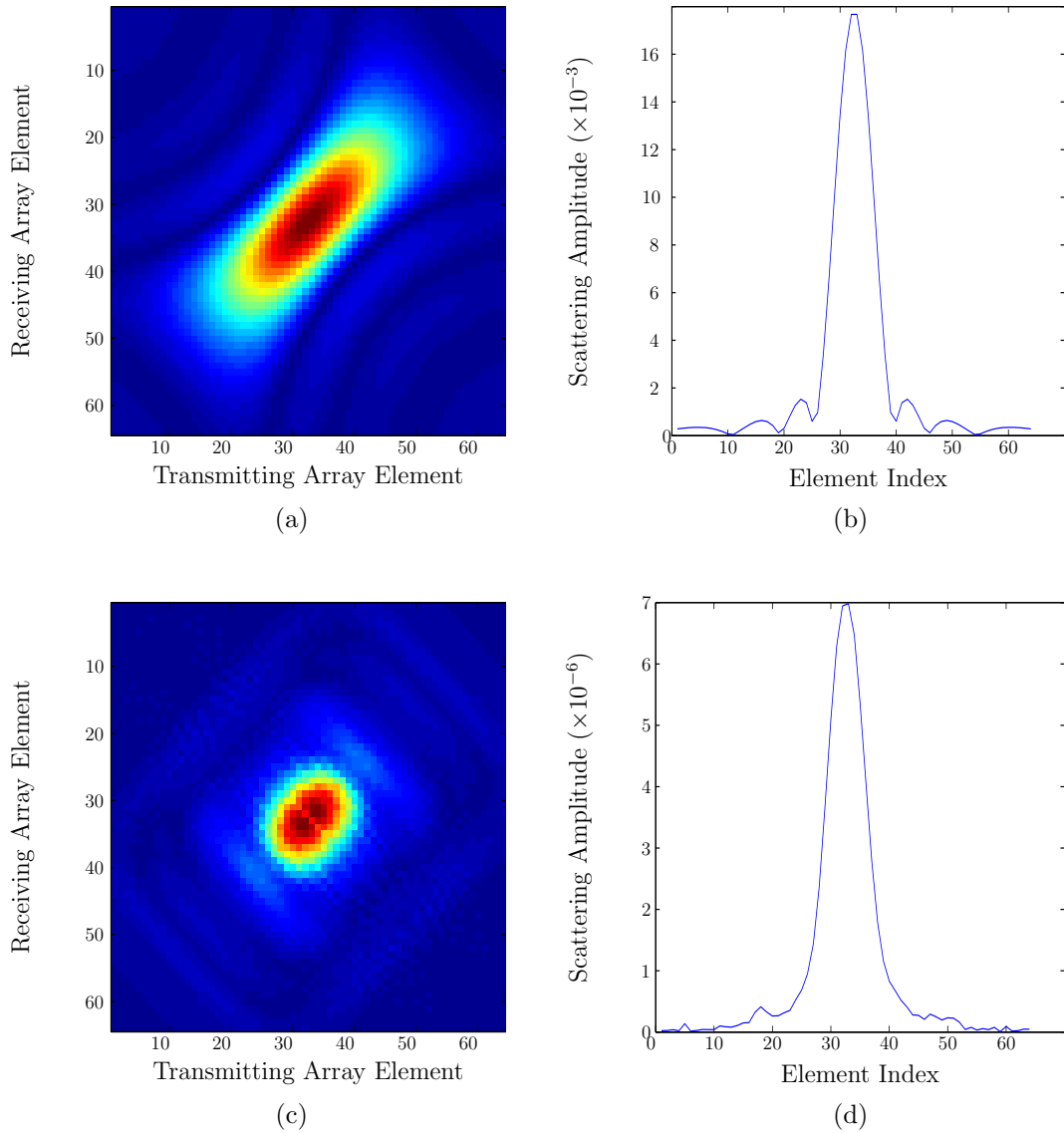


Figure 3.23: Plots comparing the scattering matrices and their corresponding pulse-echo responses from a finite element, time domain simulation and the Born Approximation. Plots (a) and (b) depict the scattering matrix and pulse-echo response generated by the Born approximation for a crack of 0° orientation and crack length to wavelength ratio $a/\lambda \approx 2.6$. Plots (c) and (d) depict the scattering matrix and pulse-echo response arising from the data given by Table B.1 for a crack of 0° orientation and crack length to wavelength ratio $a/\lambda \approx 2.6$. There is a good correspondence between the pulse-echo response plots.

5mm crack is 4.7mm. This objective measurement of crack size is perhaps better than expected considering the inconsistencies between the two models.

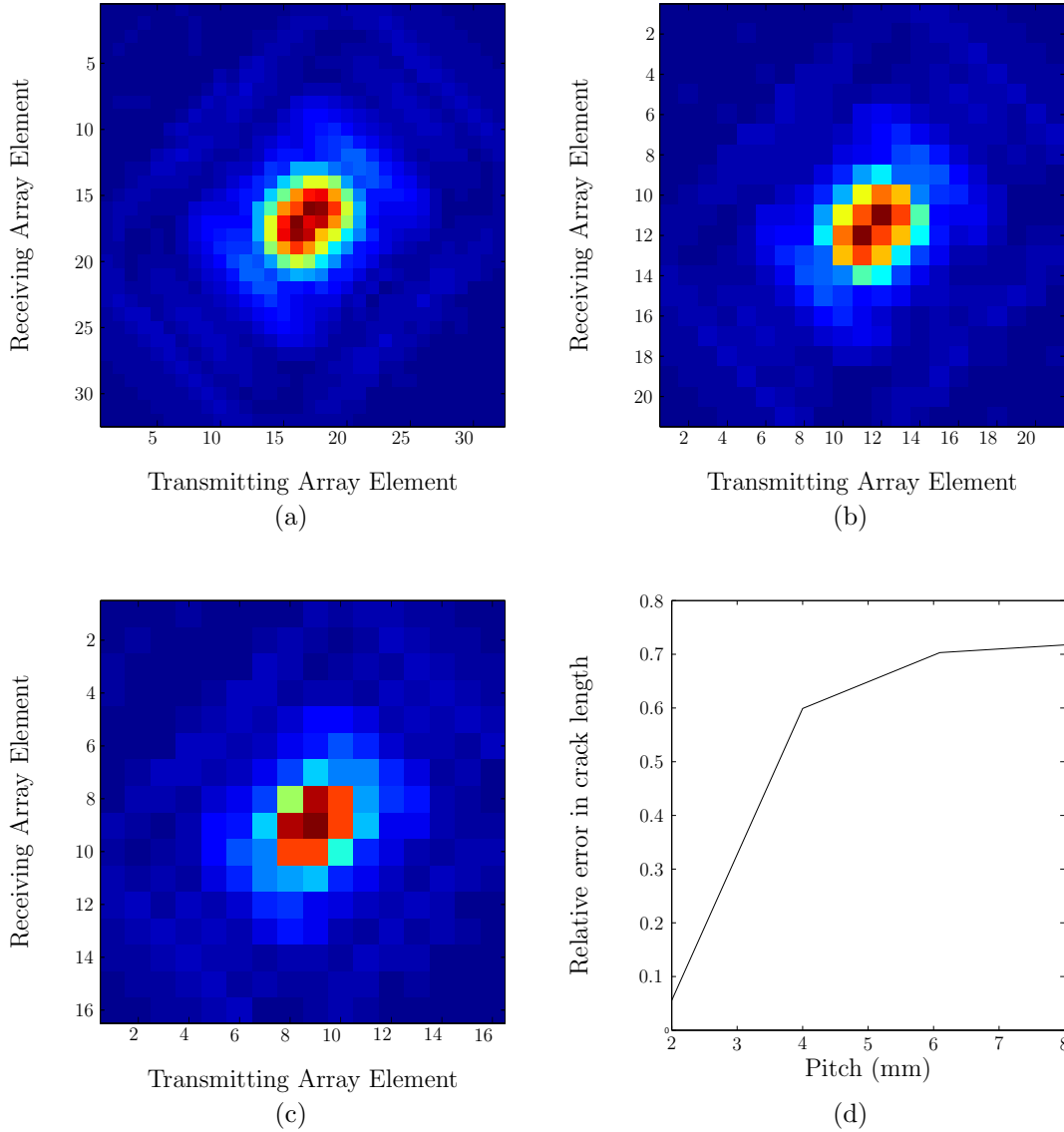


Figure 3.24: Plots showing scattering matrices arising from finite element simulations with different subsets of the full matrix capture (see Table B.1). Plot (a) simulates an artificially increased array pitch of $p^* = 4\text{mm}$, (b) $p^* = 6\text{mm}$ and (c) $p^* = 8\text{mm}$. Plot (d) plots the relative error in the crack length obtained by substituting the estimated location of the zeros (x_i) in these scattering matrices corresponding pulse-echo response plots in equation (3.9).

3.6.2 Effects of an Artificially Decreasing Array Length

It was shown in equation (3.12), Section 3.4.1 that we could analytically obtain a value for the minimum length of the array aperture needed to successfully capture both zeros of the pulse-echo response plot arising from a crack of 0° orientation, situated beneath the centre of the array. Substituting in the values used in the finite element simulation (see see Table B.1) it was calculated that a minimum linear array aperture of $L = 28\text{mm}$ was required to capture the zeros in the pulse-echo diagonal of the scattering matrix. As seen previously in Section 3.6.1, it is possible to artificially alter physical parameters of the simulation by using subsets of the FMC. To vary the length of the array, we start by using the central 2×2 submatrix of the scattering matrix. This square matrix is then gradually increased until it returns to its original 64×64 dimensions. This is demonstrated in Figure 3.25 in which we can see submatrices of dimension (a) 12×12 , (b) 14×14 and (c) 20×20 . The crack sizing algorithm was not applicable for matrices of dimensions smaller than 12×12 . This matrix corresponds to an array length of only 24mm and hence, according to the analytical predictions, should not capture the roots of the pulse-echo response plot. This is shown to be true in plot (d), which depicts the pulse-echo response for scattering matrix (a) and confirms the fact there are no roots. Note, however, that the algorithm can still be used in this case since the tangent lines at the HWHM points cut the x -axis at element 1. And so, it can be concluded that, as a guide, the analytical expression for the minimum array length proves useful. Equation (3.13), uses this estimation to calculate the minimum resolvable crack length to wavelength ratio for a given array length L . Setting $L = 28\text{mm}$, the minimum crack length to wavelength ratio that can be resolved via this method in this case is $a/\lambda \approx 3.064$. However, if we increase the

array length to 128mm, the minimum crack length to wavelength ratio that can be resolved is $a/\lambda \approx 0.9075$. This is in line with the conclusion that as $L \rightarrow \infty$ the minimum resolvable crack length to wavelength ratio $a/\lambda \rightarrow M/2\pi = 0.71529$.

3.7 Conclusions

A model-based approach to crack-sizing via the Born approximation has been derived. Through the analysis of the pulse-echo diagonal of the scattering matrices, it was observed that the distance between the zeros surrounding the central lobe correlate with the crack length. Using these zeros, a formula was derived to extract the crack length from the scattering matrices for the case where a single crack lay parallel (zero degrees orientation) to an ultrasonic, linear array. This was then extended to cover cracks of non-zero orientation. Subsequently, it was discovered that the orientation could also be extracted from knowledge of the placement of the two innermost roots in the pulse-echo response plot. An analytical expression for the maximum error caused by discretisation arising from the finite extent of the array pitch p was derived for both cases and conclusions were drawn from these. It was shown that as the array pitch p tended to zero or the flaw depth, r , tended to infinity, this error tended to zero. The error in the approximation of the crack orientation, θ , was also studied. Through a sensitivity analysis, it was observed that the algorithm was susceptible to the errors in the measurement of these zeros in the pulse-echo profile. Thus, obtaining an accurate value for these roots is key to the method's success. As shown in the error analysis, this can be achieved by using as small an array element pitch as possible. The benefit of this method, which uses the roots of the pulse-echo response rather than the Half

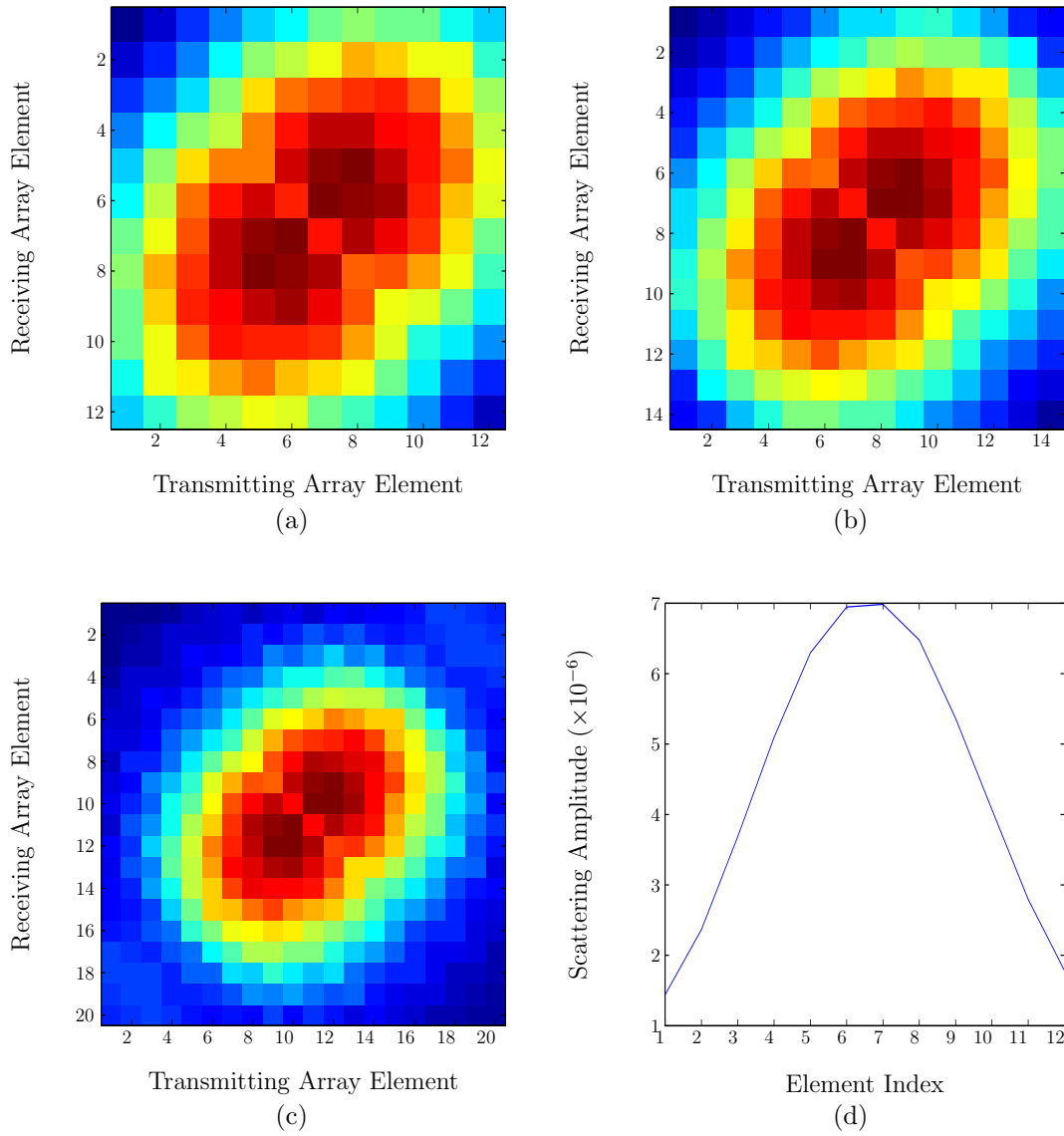


Figure 3.25: Plots showing scattering matrices arising from different subsets of the data given by Table B.1. Plots (a), (b) and (c) simulate a shorter array length by using only the central 12, 14 and 20 array elements, giving rise to an array of length 24mm, 28mm and 40mm respectively. Plot (d) is the pulse-echo response of matrix (a). Although it has no roots, using the gradient at the half-maximum and projecting on to the x -axis provides a reasonable approximation.

Width at Half Maximum (HWHM) measurement, lies in the algorithm's immunity to the transducer transfer function.

To further validate the claims made on optimal array pitch and array length, the crack sizing algorithm for cracks of 0° orientation was applied to data arising from a finite element simulation of an ultrasonic array and the scattering of the waves from this array by a crack (PZFlex, see Appendix B). As this data is generated by the finite element method, an exact match with the Born approximation was not envisioned. However, there was good qualitative agreement in the results. The array pitch and length were artificially altered by using subsets of the full matrix capture data and it was shown that as the pitch increased, so did the relative error in cracklength. In addition, the FE results confirmed that equation (3.12) is a useful guide to the minimum array length needed to capture the necessary zeros of the pulse-echo response plot.

Chapter 4

Crack Sizing via Model Based Optimisation for Application to Experimental Data

4.1 Introduction

Chapter 3 demonstrates how a mathematical model can be used to derive formulae for the characterisation of zero-volume flaws, given a frequency domain scattering matrix. This analytical formulation allows for insight into the effects of individual parameters on the ability of the algorithm to correctly size a defect. However, the method is reliant on the approximation of the roots of the pulse-echo response. Figure 4.1 demonstrates the difficulty in extracting the location of these roots from pulse-echo responses arising from (a) a PZFlex finite element simulation incorporating a heterogeneous microstructure (see Appendix B, Table B.2) and (b) experimentally collected data (see Appendix C, Table C.2). Although we have

come across this problem previously (see Section 3.6), it is no longer viable to exploit the gradient at the half-maximum to approximate the roots, as the width of the central lobe is no longer obvious. Hence, it is not possible to implement the model based crack sizing algorithm in its current form to these cases. Instead, the model will now be used as a basis for an optimisation technique, which will importantly retain the objective nature of the final crack-size estimate.

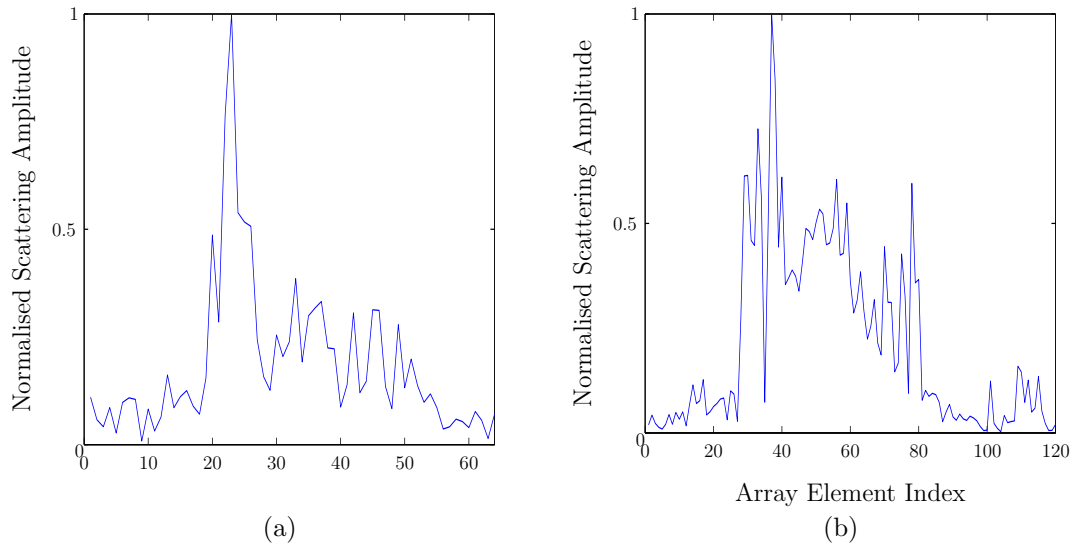


Figure 4.1: Plot (a) depicts the pulse-echo response from a finite element simulation of a 0° orientated crack of 5mm length, embedded in a heterogeneous medium where the microstructure has been generated using electron backscatter diffraction (EBSD) measurements taken from an austenitic steel weld (see Appendix B). Plot (b) depicts the pulse-echo response taken from experimentally collected data arising from a lack of fusion crack of 6mm length and 40° orientation (see Appendix C, Table C.2)

4.2 Optimisation Over Crack Length

As seen previously in Sections 3.2 and 3.3, it is possible to imitate certain variables of an experimental set up within the Born approximation, so as to generate a scattering matrix from the model which is comparable to that derived from the experiment. These replicable variables include: the array pitch and length, the subsequent incident and scattered wave directions, the location and depth of the flaw in relation to the array, the material properties of the host and flaw media, the frequency at which the scattering matrix is plotted at and the flaw dimensions. As the model based optimisation technique discussed below has been developed as a tool for objective characterisation, it is assumed that the location of the defect is known. Assuming, for now, that the frequency is fixed at the centre operating frequency of the transducer, all variables can be extracted from the experimental set up, with the exception of the flaw dimensions and orientation. Referring back to Section 3.3, it was observed that the location of the maximum along the pulse-echo response curve is indicative of the crack orientation and independent of the crack size. Hence, by comparing the location of the maximum in the pulse-echo response arising from the data, to that of pulse-echo responses generated by the Born approximation for varying crack orientations (and arbitrary crack sizes), an orientation can be estimated. It can be seen in Figure 4.1 that the global maximum is easily identified. However, it must be noted that in dealing with a highly heterogeneous host medium, as depicted in plot (a), the maximum shifts due to bending of the wave by the material anisotropy. It is suggested that, in this case, the calculated orientation is used to compensate for this shift. In doing so, a more accurate estimation of crack length can be extracted. Now, allowing $P^B(a)$ to denote the pulse-echo response of a scattering matrix generated via the

Born approximation for some crack length a and orientation θ (as estimated using the maximum), and letting P^e be the pulse-echo response of a scattering matrix extracted from some time domain dataset containing a crack of unknown size, we can approximate the area A under the pulse-echo curve by

$$A^B(a) = \sum_{i=1}^N P_i^B(a) \quad (4.1)$$

$$A^e = \sum_{i=1}^N P_i^e \quad (4.2)$$

for the scattering matrices arising from the model and the experiment respectively, where N is the number of array elements. Note, both pulse-echo responses have been normalised with respect to their respective maxima as we are concerned more with the scattering profile (signature) of the flaw than the scattering amplitude. The optimisation is then executed over some range of a , where the minimum gives rise to an objective estimation a_e of the crack size

$$a_e = \min_a \|A^B(a) - A^e\|_2 \quad \text{for} \quad l \leq a \leq m, \quad (4.3)$$

where m and l are the upper and lower bounds on the range of a over which we are optimising. This method is applied to data arising from finite element simulations as detailed in Appendix B (see Tables B.1 and B.2). The results are shown in Figure 4.2. Plot (a) depicts the results of the optimisation performed over the range $1\text{mm} \leq a \leq 12\text{mm}$, for a crack of length 5mm and 0° orientation, simulated with the parameters as detailed in Table B.1. The orientation, calculated using the location of the maximum of the pulse-echo response, is estimated to be a reasonably accurate -2° . However, the minimum of the curve predicts a crack

length of approximately 7.7mm. Unsurprisingly, the results shown in plot (b) for the data detailed in Table B.2 (incorporating a heterogeneous microstructure), show an even bigger discrepancy in the crack length measurement, which is estimated to be 11mm. Although quantitatively the initial results are not excellent, considering the modelling assumptions made (see Section 3.6) and the absence of any subjectivity from the measurement, the method shows potential. Plots (c) and (d) are generated by the same algorithm for the same datasets, where the optimisation has been implemented over pulse-echo responses plotted at a frequency of 3.5MHz (in both the experimental and model cases). A vast improvement in the crack length estimations is apparent in both cases with measurements of 6mm and 4mm obtained respectively. These results indicate that the data can be further exploited over a range of different frequencies and hence, a multi-frequency approach is developed below.

4.3 Development of A Multi-Frequency Optimisation Method

When converting time domain data into the time-frequency domain via the FFT, a host of scattering matrices are generated over a finite range of frequencies dependent on the bandwidth of the transducer. To fully exploit the available data, it is intuitive to explore the multi-frequency potential of the model based optimisation technique. Hence, instead of using equation (4.3), we now consider

$$a_e = \min_{a,f} \|A^B(a, f) - A^e(f)\|_2 \quad \text{for} \quad l \leq a \leq m, \quad q \leq f \leq r, \quad (4.4)$$

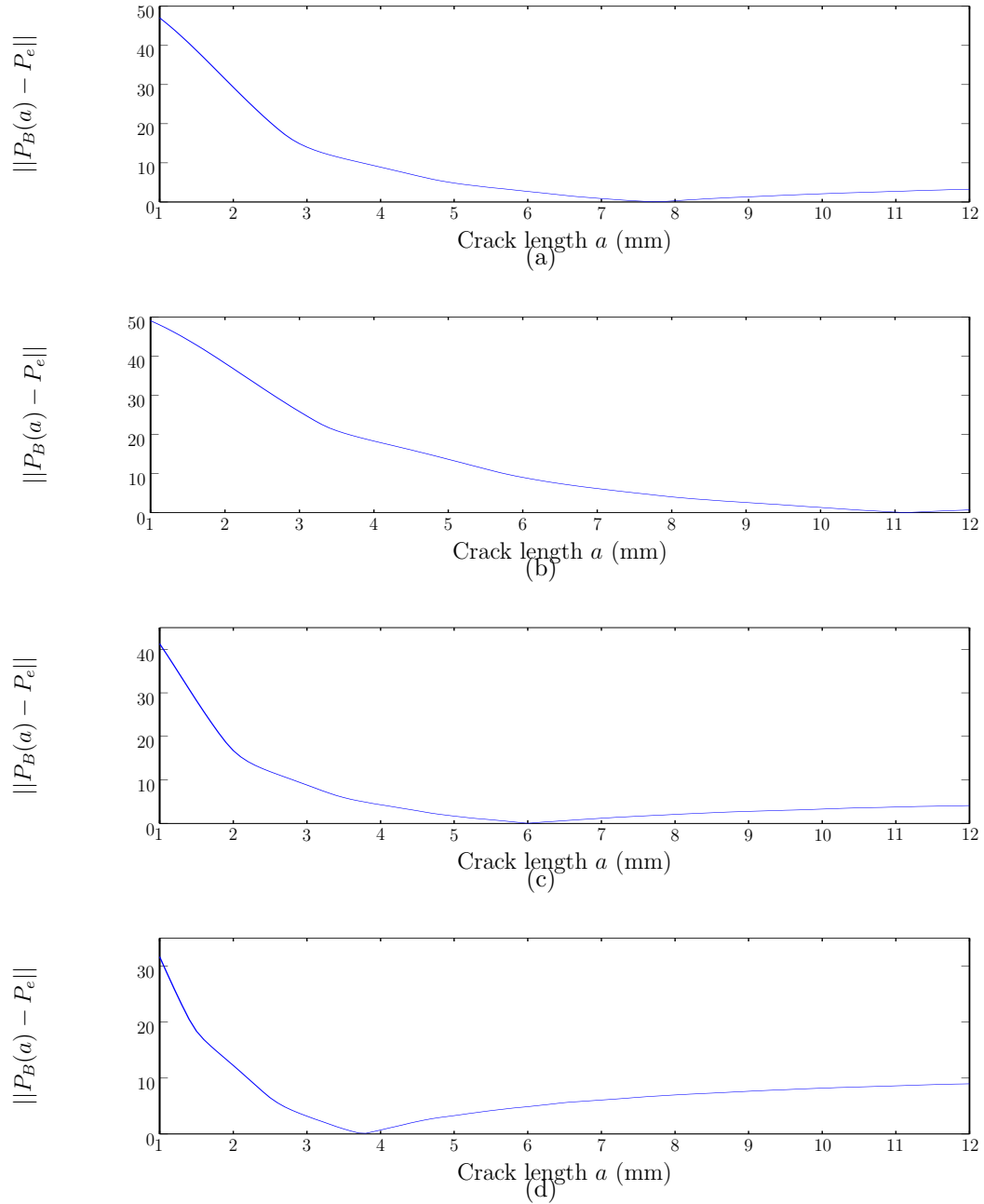


Figure 4.2: Optimisation over a range of a for pulse-echo responses arising from data as detailed in (a) Table B.2 and plotted at 1.5Mhz, (b) Table C.2 and plotted at 1.5Mhz, (c) Table B.2 and plotted at 3.5Mhz and (d) Table C.2 and plotted at 3.5Mhz.

where f is the frequency at which the pulse-echo response is plotted at, and q and r are the upper and lower bounds on the bandwidth of the transducer. It must be noted that although the maximum of the pulse-echo response is independent of frequency within the Born approximation, it does vary in the more difficult simulated and experimental datasets. Hence, to increase accuracy, for every frequency that P^e is plotted at, a new value of θ is calculated via the location of the global maximum for that specific pulse-echo response curve. This multi-frequency approach results in a matrix which records the difference in area under the pulse-echo response curves for any crack length and frequency pair. We refer to this as the Objective Sizing Matrix (OSM) and it is plotted on a logarithmic scale to allow for closer examination of the local minima. Figure 4.3 shows the results of the method's initial application over frequencies ranging from 0.5 – 10MHz. In plot (a) the algorithm is applied to the data as laid out in Table B.1. Note that the local minima lie along the thin, dark, blue region. The global minimum here gives an objective crack length measurement of 3mm. However, extracting the minima from each column of the objective sizing matrix and averaging, a new, improved objective crack length estimate of 4.6mm is produced. This agrees well with the known value of 5mm. Plot (b) is generated by applying the method to the data given in Table B.2. The global minimum estimates the crack to be approximately 10.5mm and this is greatly improved and approximated as 4.4mm if we average over the frequency domain. Considering that heterogeneities can add a significant amount to the scattering amplitude (see Figure 4.1 (a)) and will resonate more at some frequencies than others, it is to be expected that some anomalies occur over the full spectrum of frequencies. The averaging approach should minimise the contribution from these anomalies to the final estimate. Obviously, the range

of frequencies over which we average can change the estimate and the choice of this domain may introduce some subjectivity into this method. However, to remove this subjective aspect, we can set the frequency range to cover only the bandwidth of the transducer. This is demonstrated below in application to the experimentally collected data.

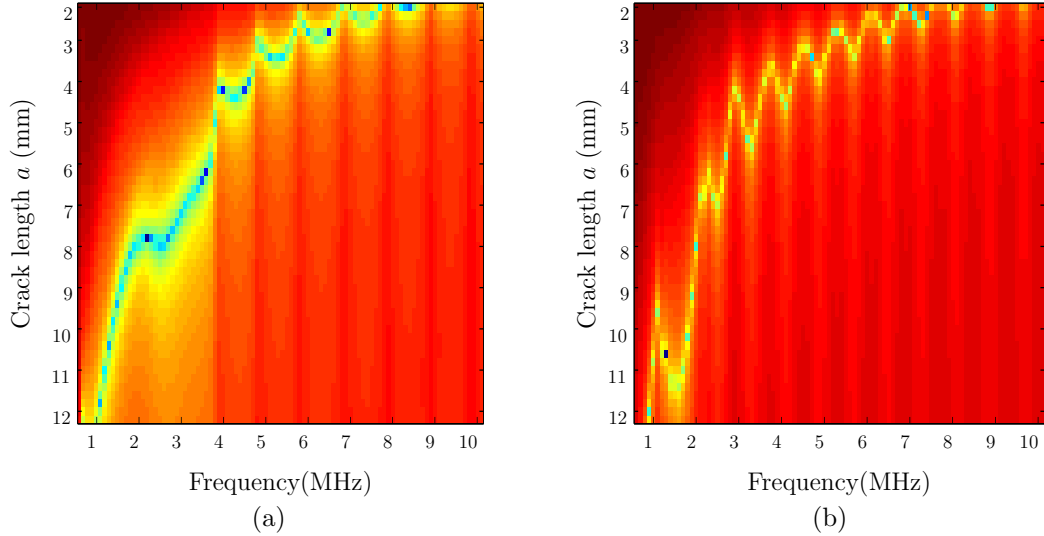


Figure 4.3: Plots of the Objective Sizing Matrix for the datasets given in (a) Table B.1 and (b) Table B.2

4.4 Application to Experimental Data

4.4.1 Scattering Submatrices

To apply our model based optimisation crack-sizing method to experimental data, we need to first convert our time domain datasets into frequency-domain scattering matrices via a discrete Fourier transform (DFT). As discussed in Section 1.1.5, in inverse problems, small errors in the collected data can result in large errors in

the solution (which in this case is the crack size). Although typical regularisation techniques, such as Tikhonov regularisation [49], have not been implemented here, several precautions have been taken to ensure our algorithm can be implemented successfully. Firstly, it is assumed that the location of the flaw is known *a priori*. This allows us to take the Fourier transform over the small time interval pertaining to the location of the flaw, excluding the majority of scattering arising from the microstructure and structural artefacts. However, extracting the interval related solely to the flaw scattering is not always possible. The Total Focussing Method (TFM) can be used to illustrate this particular problem. Figure 4.4 (a) depicts a TFM image arising from the data given in Table C.2. Notice that the crack is located in close proximity to the back wall. Using the now known distance of the flaw from every array element and the estimated pressure wave velocity, the time window corresponding to the flaw scattering can be isolated for every time trace. The TFM can then be recalculated for this cropped time-domain dataset; this is shown in Figure 4.4, image (b). Note that although we are only plotting over a relatively small interval of 146 timesteps (equivalent to the time taken for the wave to travel a distance of 8.5mm through the weld), there are still remnants from the backwall in the image. Figure 4.5 demonstrates that, in some cases, the time taken to reach the flaw can equal the time taken to reach the back wall. Further decreasing the interval proves futile and can also result in a loss of definition of the flaw itself, which is not desirable. Hence, in taking the DFT over this interval and plotting the resulting scattering matrices, it is expected that there may be some interference from the back wall.

Scattering matrices generated over this interval have been plotted in Figure 4.6. Plot (a) depicts the full scattering matrix over the 128 array elements plotted

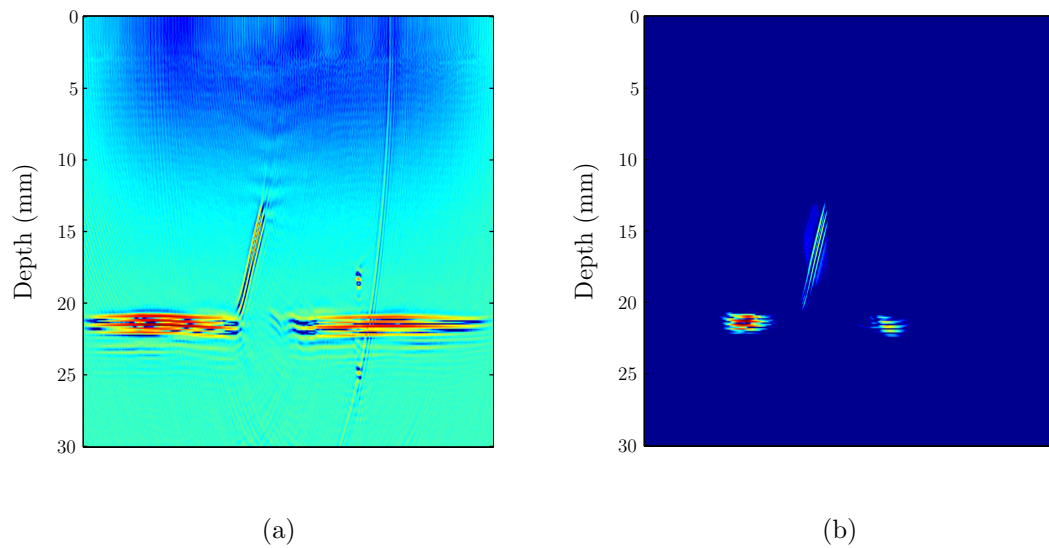


Figure 4.4: Image (a) has been generated via the TFM (with a 30dB threshold) for the data arising from the experiment as detailed in Table C.2. Using the location of the flaw as detected in this image, the Full Matrix Capture of the data has been cropped around a time interval corresponding to the flaw scattering. Image (b) shows the resulting TFM over the same imaging domain. Unfortunately, due to their close proximity, the scattering from the flaw and the back wall are inextricably linked.

at the central operating frequency of the transducer. The comparable scattering matrix as generated by the Born approximation is shown in plot (b). It can be observed that although the highest amplitude lobe of plot (a) is of similar size and location as that of plot (b), there is some additional interference in the bottom, right corner. This can be attributed to scattering by the back wall as discussed above. To negate this unwanted effect and further regularise the data, we can choose to use only a submatrix of the scattering matrix. In this case, we have chosen to consider only the responses corresponding to transmission and reception by the first 60 array elements. Note, that due to the orientation of the crack, this is the section of the array which captures the scattered signals which lie closest to the specular reflection. The signals which have been ignored should be of lower amplitude as they involve a longer travel time, and are therefore subject to more attenuation (as seen in Figure 4.5). This submatrix results in plot (c), and the corresponding model based matrix, plot (d). Plots (e) and (f) depict scattering submatrices from the same dataset (Table C.2), plotted at different frequencies. Plot (e) displays a slight narrowing of the central lobe, characteristic of a rise in frequency (as seen in Section 3.3) and plot (f) depicts a high amplitude pulse-echo response which continues past the central lobe of the scattering matrix. These high amplitudes at the pulse-echo can be attributed to the ring down of the array elements, where the transmitted wave from the transmitting element can initially interfere with the reception of that same element (see Figure 2.9). This effect can be overshadowed when the scattering amplitude is large (as in plot (e)) but, due to the multi-frequency nature of the algorithm, can lead to some misleading results at lower frequencies. However, the averaging of the crack length estimate over all frequencies within the bandwidth of the transducer (as discussed in Section

4.3), should minimise the interference the ring down has on the final crack length estimate.

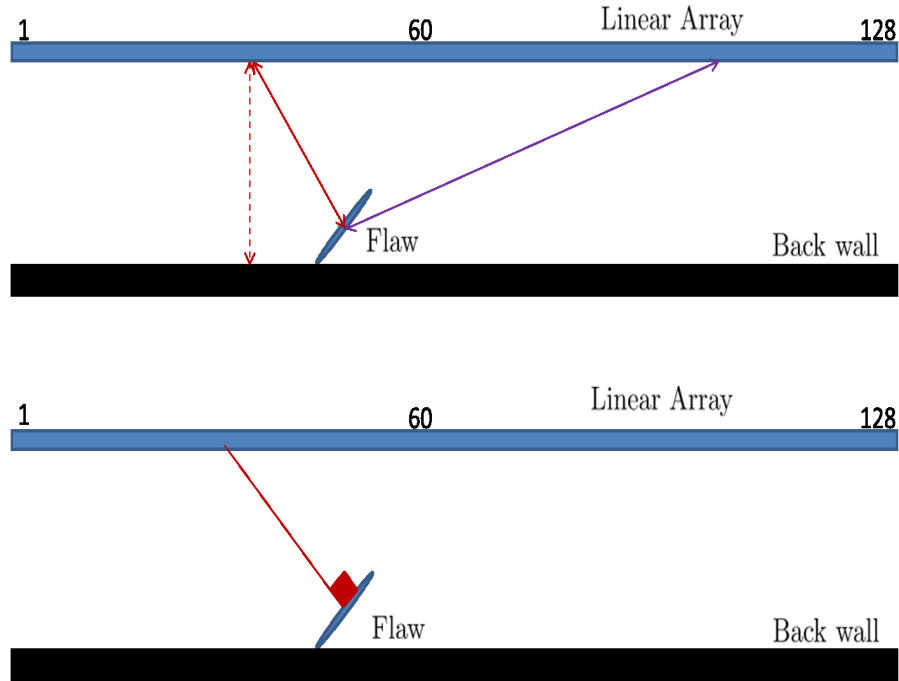


Figure 4.5: The above schematics depict an 128 element array placed over the shallow sample as described in Table C.2, with a crack of 6mm length at 40° orientation located near the back wall. The top schematic demonstrates that in some cases, the time taken to reach the flaw (solid red arrow) is equal to that taken to reach the back wall (dashed red arrow). The purple arrow is representative of the signals excluded from the scattering submatrix. Its longer travel time means it is more prone to attenuation, hence giving way to a lower scattering amplitude. The bottom schematic shows that employing only the first 60 array elements, it is possible to capture the high amplitude scattering arising from the specular reflection.

4.4.2 Extending the Multi-Frequency Optimisation over the Scattering Matrix

Until now, both the single frequency and multi-frequency optimisation approaches have been performed over the pulse-echo responses of the scattering matrices.

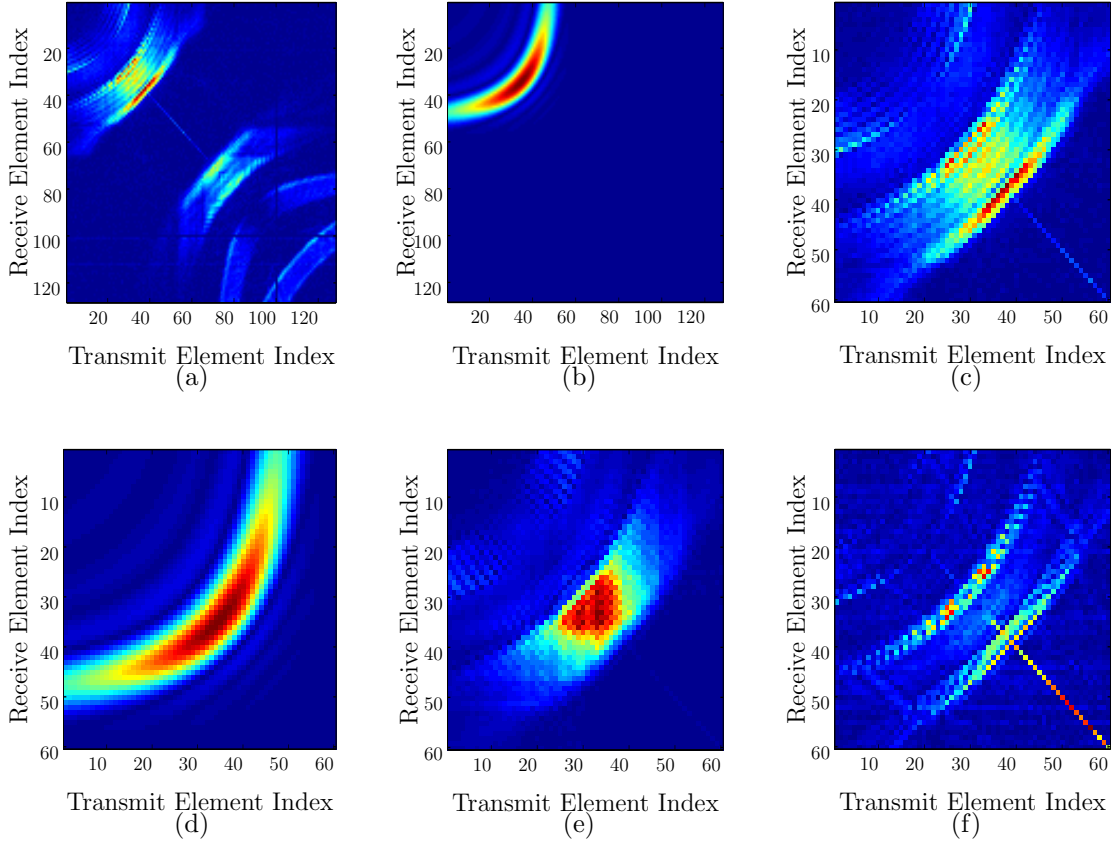


Figure 4.6: Plot (a) is the scattering matrix taken from the experimental data as described in Table C.2, plotted at the centre operating frequency of the transducer (5MHz). Plot (b) has been generated via the Born approximation, imitating the experimental properties in Table C.2. Plots (c) and (d) are the respective submatrices of (a) and (b), using only the signals captured by the first 60 elements of the array. Plot (e) is also from the experimental data but plotted at a higher frequency of 8MHz. Plot (f) is plotted at approximately 2MHz and demonstrates problems arising from the *ring down* of the array elements.

However, in doing so, only N elements of the scattering matrix are utilised. The method can be extended to fully exploit the $N \times N$ elements of the scattering matrix by implementing the optimisation over the full matrix (or submatrix of interest), and comparing the total energy received over the entire array. The difference in this energy, between the scattering matrices arising from the experimental data F^e , and the corresponding scattering matrices generated by the model over a range of crack lengths F^B , is what will now be plotted for each frequency and crack length pair in the objective sizing matrix M

$$M_{a,f} = \left\| \sum_i^N \sum_j^N F_{i,j}^B(a, f) - \sum_i^N \sum_j^N F_{i,j}^e(f) \right\| \quad (4.5)$$

The results below correspond to submatrices of size 60×60 (as seen in Section 4.4.1), arising from the data given by Table C.2. As mentioned in Section 4.3, the crack orientation is estimated at every frequency, allowing us to tailor the model based scattering matrices to the experimental scattering matrix in question. Averaging the estimations of orientation over all frequencies, an objective estimate of 47° crack orientation was reached, giving way to an absolute error of only 7° . Figure 4.7 displays the objective sizing matrix calculated by exploiting (a) the pulse-echo response only and (b) the full scattering submatrix. It is observed that in both plots, when $f \leq 2\text{MHz}$, the results seem incongruous with the rest of the plot. This can be attributed to the bandwidth of the transducer; at its outer limits the array is more susceptible to noise (such as the *ring down*, as discussed in Section 4.4.1 and shown in Figure 4.6). The effects of this can be minimised by the averaging approach taken over the frequency range. Again, this can be perceived as a type of regularisation as it minimises the contributions from

any ill-conditioned matrices. The global minimum of plot (a) occurs when the crack length is equal to 3mm and the frequency is 5.6MHz. However, averaging over the range of frequencies covered by the 0.5 – 10MHz pass band filter, the objective crack length measurement obtained is 3.6mm. Inspecting the objective crack sizing matrix as plotted in plot (b), generated by optimising over all 60×60 elements of the scattering submatrix, the global minimum occurs when the crack length is equal to 7.4mm at a frequency of 3.4MHz. Averaging over the frequencies lying within the band-pass filter applied to the transducer, we obtain the objective crack length estimation of 6.2mm (recall the actual crack length is 6mm), yielding a relative error of only 3%.

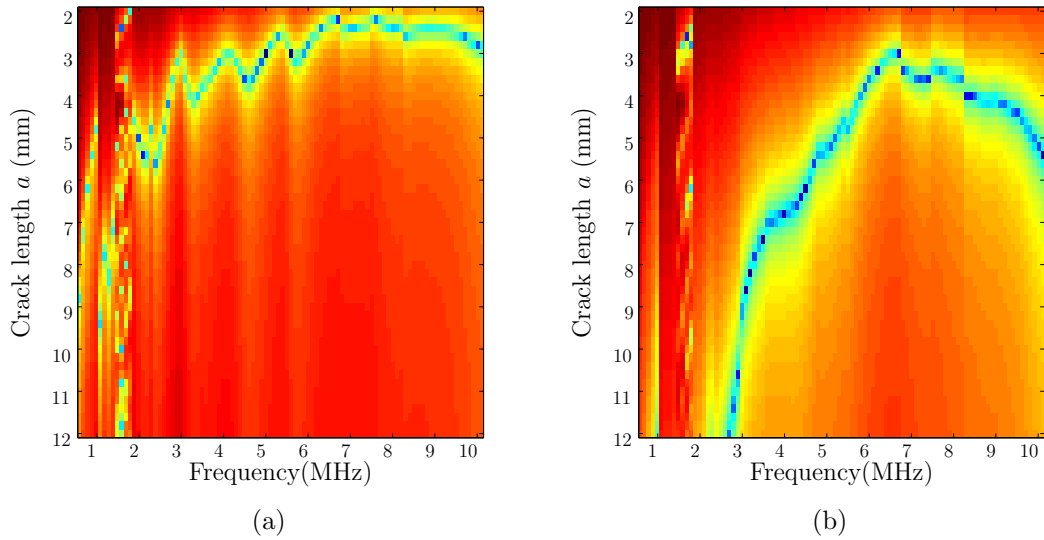


Figure 4.7: Plots of the Objective Sizing Matrix for the dataset given in Table C.2, computed over the range of frequencies determined by the pass band filter that was applied to the transducer (0.5–10MHz). Plot (a) arises from the optimisation carried out over the pulse-echo of the scattering submatrices and plot (b) from the optimisation executed over all $N \times N$ elements of the scattering submatrices.

4.5 Conclusions

Although the crack sizing algorithm as developed in Chapter 3 proved interesting from a mathematical perspective, providing analytical insight into the effects of array pitch and length, crack length to wavelength ratio, frequency and flaw depth, it was deemed unsuitable for application to experimentally collected data, due to the difficulty of extracting the zeros of the pulse-echo response curve. Hence, it was decided to use the model as a basis for an optimisation technique, which importantly retains the objectivity of the final crack length estimate. Firstly, the orientation of the crack is determined; it was ascertained in Chapter 3 that the location of the global maximum along the pulse-echo response is indicative of crack orientation. Next, the sum of the energy beneath the pulse-echo response curve was used to measure the similarity between the scattering matrices generated via the model and those produced by the data at a fixed frequency (typically chosen to be the central operating frequency of the transducer in the experiment). Initial results were poor but it was observed that plotting the pulse-echo response at different frequencies gave rise to a range of recovered values. Hence, a multi-frequency approach was developed to exploit the information available over the entire bandwidth of the transducer. Unfortunately, due to anomalies caused by the resonance of heterogeneities and the consequences of dealing with experimental equipment (i.e. the ring down), using the global minimum over this now two dimensional Objective Sizing matrix, was not always reliable. Therefore, it was decided to extract the minima of each matrix column, and average over all frequencies. Another adjustment to the algorithm was made in the form of cropping the scattering matrices. The scattering matrix as derived from the experimental data in Table C.2 displayed some interference from scattering by the back wall,

which was not incorporated in the model. In an attempt to lessen the gap between the model and experiment, it was decided to use only the submatrix corresponding to the flaw scattering. The optimisation over the pulse-echo response was once again executed and produced promising results. However, it was realised that by only considering the N diagonal elements of the $N \times N$ matrix, useful information was being excluded. This observation gave rise to the development of the more effective full matrix optimisation technique. In application to the available experimental data, this provided an objective crack length estimate of 6.2mm with 47° orientation, for an actual crack of length 6mm at 40° orientation.

Chapter 5

Improved Signal to Noise Ratio by Using Chirp Excitations to Illuminate Flaws

5.1 Coded Excitations

Coded excitations are an effective way of delivering large amounts of energy using relatively low acoustic pressure amplitudes. Inspiration for coded signal design can be drawn from bioacoustics; bats and dolphins use frequency modulated sweeps to navigate and hunt [6, 7]. The use of coded excitations in signal processing has been shown to improve signal to noise ratio (SNR) and lessen trade-offs between sample penetration and image resolution [64, 65]. There are numerous examples of different types of coded excitation. Golay Sequences, commonly used in radar, are complementary pairs of signals whose out of phase auto-correlation coefficients equal zero when summed [101]. Zero phase (ZPH) signals, also known as ladder

chirps [102], are engineered via the summation of a series of sine waves at different frequencies, with no initial phase offset. They provide high energy over a short duration to mimic the clicks of dolphins. Figure 5.1, plot (a) depicts a ladder chirp constructed by the summation of sine waves over sixty different frequencies. Chirps contain a frequency content that varies with time, typically in a linear or exponential manner. Their broad frequency content increases the likelihood of reaching the resonant frequency of a defect, in turn causing stronger vibrations and consequently improving the probability of detection. Figure 5.1, plot (b) depicts the plot of a linear chirp with gradient $m = 1\text{Hz}$. For the purposes of this work, a Gaussian modulated linear chirp in time t of the form

$$q(t) = \exp[-2\pi i f_1(t + mt^2)] \exp\left[-\frac{(t - t_1)^2}{\sigma^2}\right] \quad (5.1)$$

has been employed, where m is the gradient of the chirp (the rate at which it sweeps through a prescribed range of frequencies), f_1 is the initial frequency, t_1 is the centre of the Gaussian envelope and σ is the standard deviation. By varying f_1 , m and σ , the bandwidth of the chirp can be altered. Setting $m = 0\text{Hz}$, the chirp reverts back to a time harmonic signal with frequency f_1 . For a fair comparison of the chirp with a continuous gated waveform (the typical signal emitted by the transducer), it is imperative both are optimised for the same transducer and hence utilise its full bandwidth. Figure 5.2 shows one such matched pair. In the time domain, the gated continuous sine wave (in red) spans a far shorter time interval than that of the Gaussian modulated linear chirp, whilst both signals have the same peak amplitude. Studying the plots of their respective Fourier transforms in plot (b), it is apparent that they have similar -6dB bandwidths (circa 50%) but

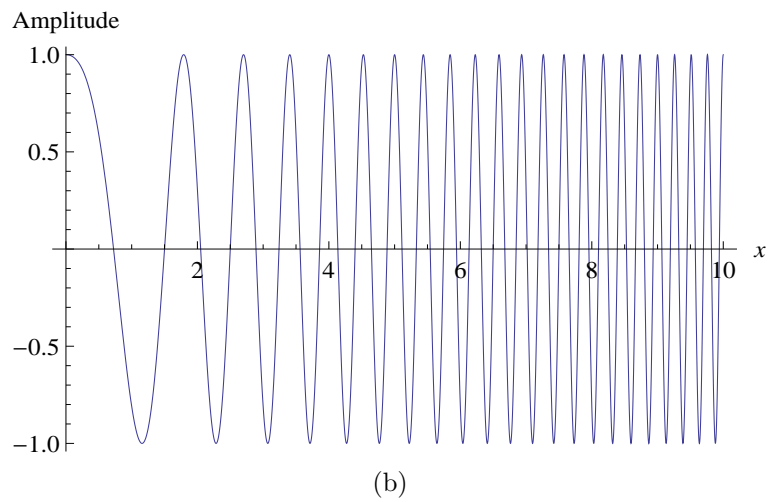
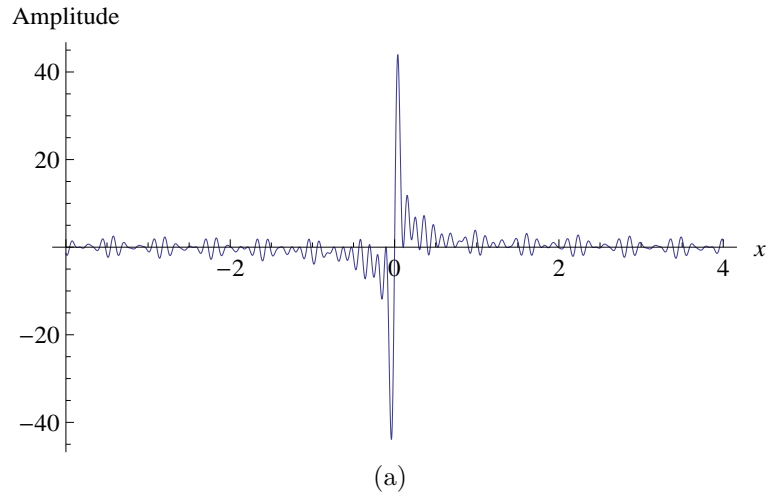
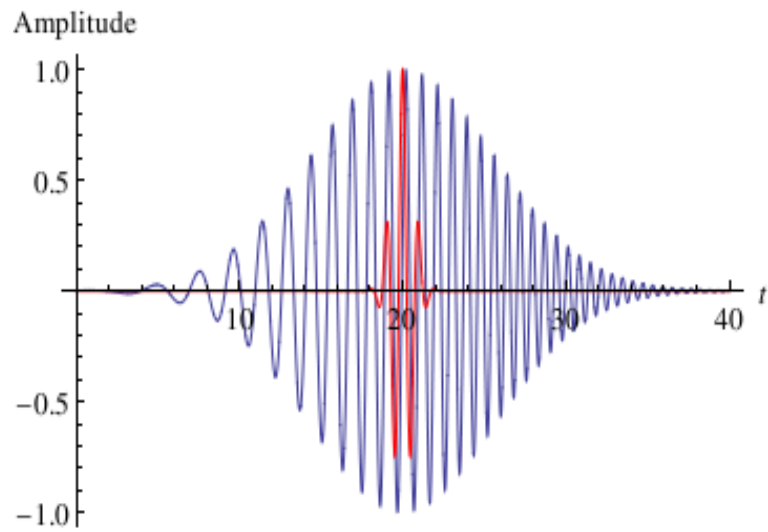
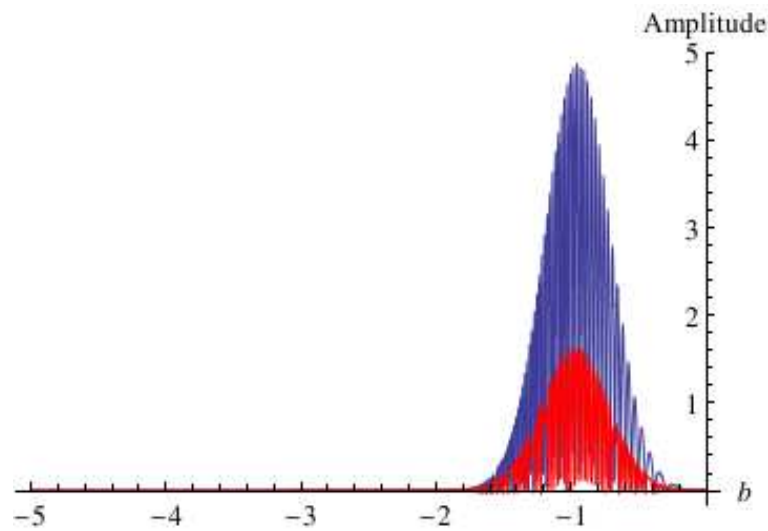


Figure 5.1: Image (a) depicts a ladder chirp constructed by the summation of sine waves over sixty different frequencies. Image (b) depicts a linear chirp with gradient $m = 1\text{Hz}$ and initial frequency $f = 0.2\text{Hz}$.

observe that the chirp contains an increased amount of energy.



(a)



(b)

Figure 5.2: Plot (a) depicts a gated continuous sine wave with frequency $f = 1\text{Hz}$ modulated by a Gaussian envelope with parameters $\sigma = 1\mu\text{s}$, $t_1 = 20\text{s}$ (in red) and a Gaussian modulated linear chirp with parameters $\sigma = 8\mu\text{s}$, $t_1 = 20\text{s}$, $m = 0.22\text{Hz}$, $f_1 = 0.1\text{Hz}$ (in blue). Their respective Fourier transforms are shown in plot (b).

5.2 The Fractional Fourier Transform

The theory of fractional powers of the Fourier transform was originally presented by V. Namias in 1980 [60], and later given a rigorous mathematical framework by McBride and Kerr in [61, 62, 103]. As a generalisation of the ordinary Fourier transform, the fractional Fourier Transform (FrFT) is more flexible in its applications and hence of potential interest to any area in which the Fourier transform is frequently implemented. Its main advantage is that it allows continuous movement between the time and frequency domains, retaining information from each, thus presenting an alternative to using the time windowed Fourier transform. Figure 5.3 demonstrates the increased versatility of the FrFT over the ordinary Fourier transform, depicting just a few of the infinite possibilities which lie in the continuous spectrum of angles $-\pi \leq \alpha \leq \pi$ (equivalent to the order of the FrFT a satisfying $-2 \leq a \leq 2$). There exist several conventions for defining the FrFT, each of which give a slightly different physical interpretation. For the purposes of this work, the fractional Fourier transform of order a is given as the linear integral transform [59]

$$\mathcal{F}_a(u) \equiv \int_{-\infty}^{\infty} K_a(u, u') f(u') du', \quad (5.2)$$

where

$$K_a(u, u') \equiv \sqrt{1 - i \cot \alpha} \exp [i\pi(\cot \alpha u^2 - 2 \csc \alpha uu' + \cot \alpha u'^2)] \quad (5.3)$$

and $\alpha = a\pi/2$. The kernel $K_a(u, u')$ satisfies the properties as listed in Table 5.1 and hence allows the FrFT to satisfy the properties as listed in Table 5.2. When a is an integer, it denotes the number of repeated applications of the ordinary Fourier transform. Hence, setting $a = 1$ (and consequently, $\alpha = \pi/2$), equation

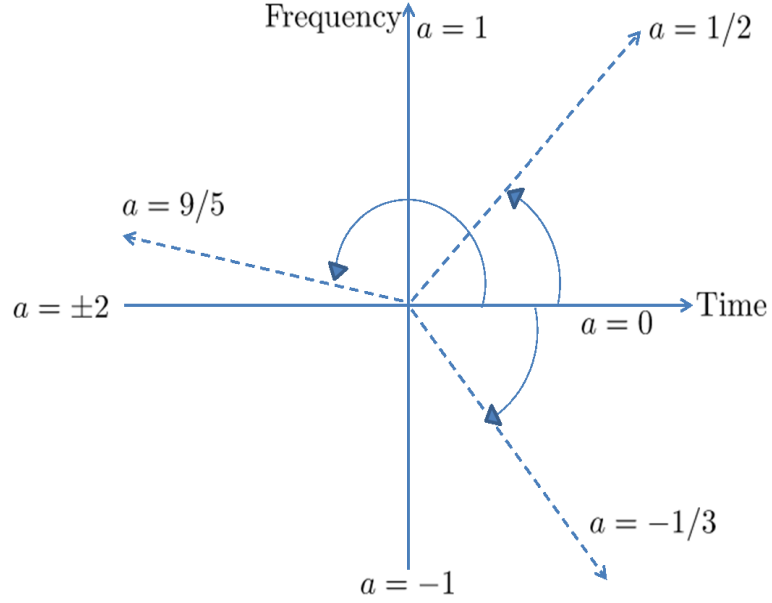


Figure 5.3: This schematic demonstrates some of the possibilities of the fractional Fourier transform where data on the time axis can be mapped to any axis u at an angle $\alpha = a\pi/2$ (relative to the positive time axis), where $-2 \leq a \leq 2$.

(5.2) simplifies to

$$\mathcal{F}_1(u) \equiv \int_{-\infty}^{\infty} f(u') e^{-i2\pi uu'} du', \quad (5.4)$$

the definition of the Fourier transform as used by Ozaktas et al in [59]. To extend to the $a = 0$ case, the kernel given by equation (5.3) is rewritten

$$K_a(u, u') \equiv \frac{e^{-i(\pi \operatorname{sgn}(\alpha)/4 - \alpha/2)}}{\sqrt{|\sin \alpha|}} \exp [i\pi(\cot \alpha u^2 - 2 \csc \alpha uu' + \cot \alpha u'^2)]. \quad (5.5)$$

Taking the first term of the Laurent series for $\cot \alpha$ and $\csc \alpha$ around the origin gives

$$\begin{aligned} K_a(u, u') &= \frac{e^{-i\pi \operatorname{sgn}(\alpha)/4}}{\sqrt{|\alpha|}} \exp [i\pi(u^2/\alpha - 2uu'/\alpha + u'^2/\alpha)] \\ &= \frac{e^{-i\pi \operatorname{sgn}(\alpha)/4}}{\sqrt{|\alpha|}} \exp [i\pi((u - u')^2/\alpha)], \end{aligned} \quad (5.6)$$

and allowing $\alpha \rightarrow 0$, it can be written that

$$K_0(u, u') = \delta(u - u'). \quad (5.7)$$

Hence, from the sifting property of the Dirac delta function it can be shown

$$\mathcal{F}_0(u) = \int_{-\infty}^{\infty} \delta(u - u')f(u')du' = f(u), \quad (5.8)$$

returning the original function. Similarly, at $a = \pm 2$ ($\alpha = \pm\pi$) it can be shown that

$$\mathcal{F}_{\pm 2}(u) = \int_{-\infty}^{\infty} \delta(u + u')f(u')du' = f(-u). \quad (5.9)$$

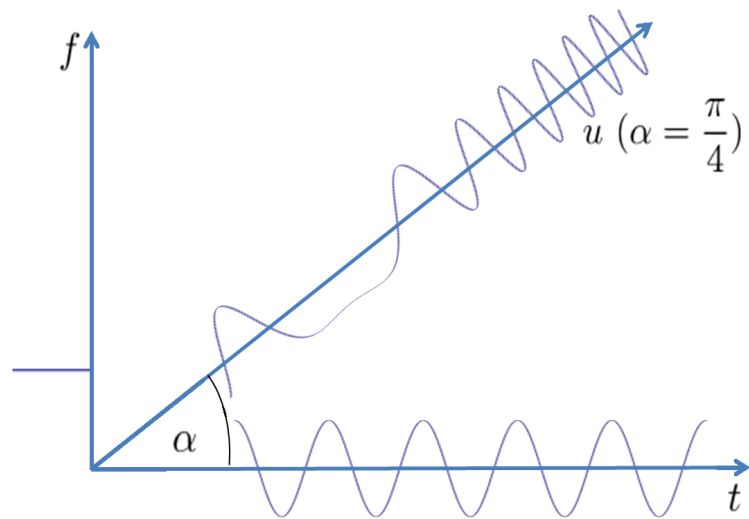
It can be observed from equation (5.9) and Figure 5.3 that the FrFT is periodic in a with period 4. As the name suggests, the fractional Fourier transform is not limited to integer powers and a can in fact take the value of any real or complex number. In the case of a complex power, $a = a_1 + ia_2$, the index additivity law (see Table 5.2) can be used to separate the transform into a real ordered transform and a complex ordered transform (equation (5.2) holds for complex values of a). However, only real ordered transforms will be considered below. Above, the fractional Fourier transform is described as a tool which facilitates continuous movement between the time and frequency domains. This is demonstrated by the diagram in Figure 5.4, plot (a). Between the time axis, t , and the frequency axis f , the signal can be plotted along any intermediate axis, u . Each axis u is partnered with an angle $\alpha = a\pi/2$, relative to the time axis. The translation to time order plots is shown in plot (b). Figure 5.5 depicts time-order plots of the FrFT for orders $0 \leq a < 1$ for several different functions. Plot (a) depicts

| | |
|------------------------------------|-----------------------------------------------------------------|
| Periodicity ($a = 4j + b$) | $K_a(u, u') = K_b(u, u')$ |
| Forward Transform ($a = 4j + 1$) | $K_a(u, u') = K_1(u, u') = \exp(-i2\pi uu')$ |
| Inverse Transform ($a = 4j - 1$) | $K_a(u, u') = K_{-1}(u, u') = \exp(i2\pi uu')$ |
| Identity Operator ($a = 4j$) | $K_a(u, u') = K_0(u, u') = \delta(u - u')$ |
| Parity Operator ($a = 4j \pm 2$) | $K_a(u, u') = K_{\pm 2}(u, u') = \delta(u + u')$ |
| Inverse Property | $K_a^{-1}(u, u') = K_{-a}(u, u')$ |
| Index Additivity | $K_{a_2+a_1}(u, u') = \int K_{a_2}(u, u'')K_{a_1}(u'', u')du''$ |

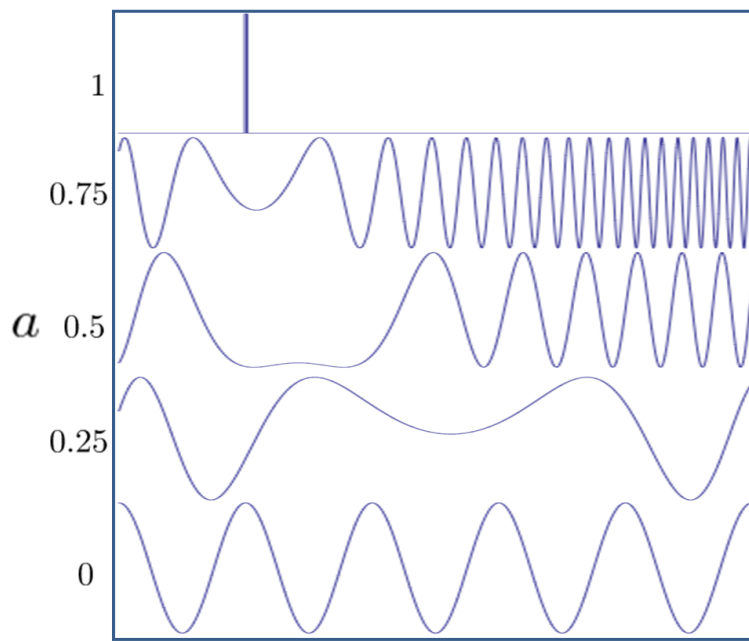
Table 5.1: Properties of the fractional Fourier transform Kernel $K_a(u, u')$

| | |
|------------------|---------------------------------------------------------------------------------------------------------------------|
| Linearity | $\mathcal{F} \left[\sum_j \alpha_j f_j(u) \right] = \sum_j \alpha_j \mathcal{F}^a f_j(u)$ |
| Inverse | $(\mathcal{F}^a)^{-1} = \mathcal{F}^{-a}$ |
| Index Additivity | $\mathcal{F}^{a_2} \mathcal{F}^{a_1} = \mathcal{F}^{a_2+a_1}$ |
| Commutativity | $\mathcal{F}^{a_2} \mathcal{F}^{a_1} = \mathcal{F}^{a_1} \mathcal{F}^{a_2}$ |
| Associativity | $\mathcal{F}^{a_3} (\mathcal{F}^{a_2} \mathcal{F}^{a_1}) = (\mathcal{F}^{a_3} \mathcal{F}^{a_2}) \mathcal{F}^{a_1}$ |
| Eigenfunctions | $\mathcal{F}^a \psi_l = \exp(-ial\pi/2) \psi_l$ |
| Parseval | $\langle f(u), g(u) \rangle = \langle f_a(u), g_a(u) \rangle$ |

Table 5.2: Properties of the fractional Fourier transform



(a)



(b)

Figure 5.4: Plot (a) demonstrates the continuous movement between the time and frequency domains of a time-harmonic wave as facilitated by the FrFT. Plot (b) depicts how the resulting signals can be displayed in a time-order plot.

the FrFT of a time harmonic function. The evenly spaced troughs and peaks at $a = 0$ (the original time domain signal) slowly converge to a single peak as $a \rightarrow 1$, representing the delta function. Plot (b) shows the results of the application of the FrFT to a delta function. The single peak at $a = 0$ slowly flattens out, culminating in a line with amplitude 1 and infinite bandwidth. As a change of frequency with time is inherent to the nature of a chirp, the FrFT is a natural choice for their analysis. Plots (c)-(f) plot the results for four different linear chirp functions, given by

$$q(u) = \exp [i\pi(mu^2 + 2f_1u)] , \quad (5.10)$$

where m is the gradient of the chirp and f_1 is the initial frequency. Plot (c) shows the results for a linear chirp with parameters $f_1 = 0.01\text{Hz}$ and $m = 1\text{Hz}$. As m is increased to 5 and then 20 in plots (d) and (e) respectively, it can be seen that the frequency content of the chirp (at $a = 1$) gradually approaches that of the delta function due to the broad frequency content. Plot (f) is the result of the application of the FrFT to a linear chirp with $f_1 = 1\text{Hz}$ and $m = 1\text{Hz}$, demonstrating the effects of altering the initial frequency f_1 .

5.3 The Wave Equation with Linear Chirp Forcing Function

As mentioned previously, the fractional Fourier transform is complementary to the multi-frequency nature of the linear chirp. To build a mathematical framework to allow for analysis of the scattering of an ultrasonic chirp by a flaw, the wave equation with a time dependent forcing function, $q(t)$, will be solved in the time-

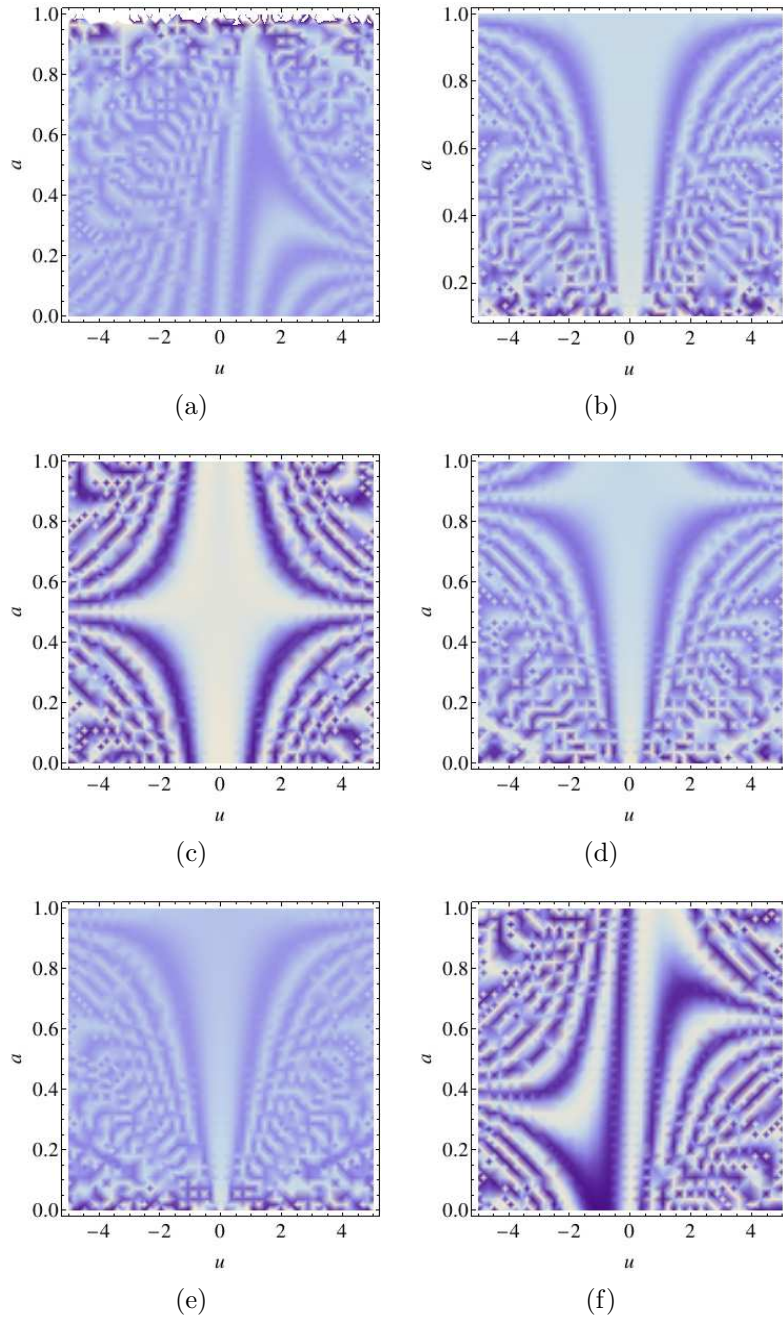


Figure 5.5: Density plots of the fractional Fourier transform over orders $0 \leq a < 1$ for (a) a time harmonic function, (b) the delta function and a host of linear chirps with parameters (c) $m = 1\text{Hz}$, $f_1 = 0.01\text{Hz}$, (d) $m = 5\text{Hz}$, $f_1 = 0.01\text{Hz}$, (e) $m = 20\text{Hz}$, $f_1 = 0.01\text{Hz}$ and (f) $m = 1\text{Hz}$, $f_1 = 1\text{Hz}$.

frequency space. Note that $q(t)$ is spatially independent and hence acts like a body force, affecting the whole flaw domain simultaneously. To justify this, we assume that the length of the flaw is smaller than the wavelength. This is in keeping with the low frequency assumption made in the Born approximation [94]. A second assumption inherent to the Born approximation is that the transmission and reception of waves takes place at a distance from the flaw which is much larger than the wavelength; the far-field assumption. Firstly, consider the non-homogeneous wave equation

$$\frac{\partial^2}{\partial t^2} f(\mathbf{x}, t) - c^2 \nabla^2 f(\mathbf{x}, t) = q(t) \quad (5.11)$$

where $\mathbf{x} \in \mathbb{R}_+^2$, $t \in \mathbb{R}$ and c is the wave speed. The solution is bounded in time and space and must satisfy the Sommerfeld radiation condition as given by equation (2.5), guaranteeing that the waves are outgoing and decay sufficiently fast so there exist no sources at infinity. It is also assumed that an initial pressure amplitude of h_0 is present at the ultrasonic array. From [59], the fractional Fourier transform, with respect to time, of a derivative of a function is given by

$$\mathcal{F}^a \left(\left[(i2\pi)^{-1} \frac{d}{du} \right]^n f(u) \right) = \left[\sin \alpha u + \cos \alpha (i2\pi)^{-1} \frac{d}{du} \right]^n f_a(u). \quad (5.12)$$

Hence, taking the FrFT of every term in equation (5.11) gives

$$\begin{aligned} (i2\pi)^2 \sin^2 \alpha u^2 f_a(\mathbf{x}, u) + i4\pi \sin \alpha \cos \alpha u \frac{\partial}{\partial u} f_a(\mathbf{x}, u) + \cos^2 \alpha \frac{\partial^2}{\partial u^2} f_a(\mathbf{x}, u) \\ = c^2 \nabla^2 f_a(\mathbf{x}, u) + q_a(u), \end{aligned} \quad (5.13)$$

the non-homogeneous wave equation in time-frequency space.

5.3.1 The Homogeneous Solution

To solve equation (5.13), we start by finding the solution to the homogeneous differential equation ($q_a(u) = 0$) via separation of variables. The solution is written in product form

$$f_a^h(\mathbf{x}, u) = h(\mathbf{x})g_a(u) \quad (5.14)$$

and substituted into the homogeneous wave equation to give

$$(i2\pi)^2 \sin^2 \alpha u^2 + i4\pi \sin \alpha \cos \alpha u \frac{g_a'(u)}{g_a(u)} + \cos^2 \alpha \frac{g_a''(u)}{g_a(u)} = c^2 \frac{\nabla^2 h(\mathbf{x})}{h(\mathbf{x})} = -b^2 \quad (5.15)$$

for some $b \in \mathbb{R}$. This can then be separated into two equations

$$\left(-4\pi^2 \sin^2 \alpha u^2 + i4\pi \sin \alpha \cos \alpha u \frac{d}{du} + \cos^2 \alpha \frac{d^2}{du^2} \right) g_a(u) = -b^2 g_a(u) \quad (5.16)$$

and

$$c^2 \nabla^2 h(\mathbf{x}) = -b^2 h(\mathbf{x}), \quad (5.17)$$

from which the temporal and spatial components of the homogeneous solution can be derived. To solve equation (5.16), a chirp like ansatz of the form

$$g_a(u) = \exp[\gamma u^2 + \beta u] \quad (5.18)$$

is chosen. Substituting this into equation (5.16) gives

$$\begin{aligned} & [-(4\pi^2 \sin^2 \alpha u^2 - b^2) + i4\pi \sin \alpha \cos \alpha u(2\gamma u + \beta) \\ & + \cos^2 \alpha(2\gamma + (2\gamma u + \beta)^2)] e^{\gamma u^2 + \beta u} = 0. \end{aligned} \quad (5.19)$$

That is,

$$\begin{aligned}
& u^2(4\gamma^2 \cos^2 \alpha + i8\pi\gamma \sin \alpha \cos \alpha - 4\pi^2 \sin^2 \alpha) + u(4\gamma\beta \cos^2 \alpha + i4\pi\beta \sin \alpha \cos \alpha) \\
& + (2 \cos^2 \alpha \gamma + \beta^2 \cos^2 \alpha + b^2) = 0.
\end{aligned} \tag{5.20}$$

Equating coefficients of powers of u , γ and β can be calculated as

$$\gamma = -i\pi \tan \alpha \quad \text{and} \quad \beta = \pm \sqrt{-b^2 \sec^2 \alpha + i2\pi \tan \alpha}. \tag{5.21}$$

where the square root is taken so that the real part is positive. Hence

$$\begin{aligned}
g_a(u) = & d_1 \exp[u(-i\pi \tan \alpha u - \sqrt{-b^2 \sec^2 \alpha + i2\pi \tan \alpha})] \\
& + d_2 \exp[u(-i\pi \tan \alpha u + \sqrt{-b^2 \sec^2 \alpha + i2\pi \tan \alpha})].
\end{aligned} \tag{5.22}$$

However, to ensure that the solution is bounded in u , $d_2 = 0$.

Turning attention now to the spatially dependent component of the homogeneous solution, equation (5.17) can be recognised as the homogeneous Helmholtz equation

$$\nabla^2 h(\mathbf{x}) + \hat{k}^2 h(\mathbf{x}) = 0 \tag{5.23}$$

where $\hat{k} = b/c$ (c is the plane wave velocity and b is analogous to the circular frequency). An explicit approximation of the scattered wave at a specified b ,

$h(\mathbf{y}, b)$, is derived via the Born approximation in Appendix A, giving

$$h(\mathbf{y}, b) = h_0 \frac{e^{i\hat{k}r_s}}{r_s} \times \frac{a_1 a_2 a_3 [\gamma_\lambda - \gamma_\rho (\mathbf{e}_i \cdot \mathbf{e}_s)]}{|\mathbf{e}_i - \mathbf{e}_s|^2 r_e^2} \left[\frac{\sin(\hat{k}_0 |\mathbf{e}_i - \mathbf{e}_s| r_e) - \hat{k}_0 |\mathbf{e}_i - \mathbf{e}_s| r_e \cos(\hat{k}_0 |\mathbf{e}_i - \mathbf{e}_s| r_e)}{\hat{k} |\mathbf{e}_i - \mathbf{e}_s| r_e} \right], \quad (5.24)$$

where a_1 , a_2 and a_3 represent the flaw dimensions, $\gamma_\rho = 1 - \rho_0/\rho_1$ (ρ_0 and ρ_1 are the material densities of the host and flaw materials respectively), $\gamma_\lambda = 1 - \lambda_0/\lambda_1$ (λ_0 and λ_1 are the bulk moduli of the host and flaw materials respectively), $r_s = |\mathbf{y}|$ is the distance of the flaw from the array, h_0 is the initial pressure amplitude, \mathbf{e}_i and \mathbf{e}_s are unit vectors in the incident and scattered wave directions respectively, and r_e is the effective radius of the flaw, given by

$$r_e = \sqrt{a_1^2 (\mathbf{e}_q \cdot \mathbf{u}_1)^2 + a_2^2 (\mathbf{e}_q \cdot \mathbf{u}_2)^2 + a_3^2 (\mathbf{e}_q \cdot \mathbf{u}_3)^2} \quad (5.25)$$

where

$$\mathbf{e}_q = \frac{\mathbf{e}_i - \mathbf{e}_s}{|\mathbf{e}_i - \mathbf{e}_s|}. \quad (5.26)$$

Here, unit vectors \mathbf{u}_1 , \mathbf{u}_2 and \mathbf{u}_3 lie along the axes of the flaw. For the purposes of this work it is enough to only consider the pulse-echo case (where $\mathbf{e}_i = -\mathbf{e}_s$) and so equation (5.24) becomes

$$h(\mathbf{y}, b) = h_0 \frac{e^{i\hat{k}r_s}}{r_s} \frac{a_1 a_2 a_3 [\gamma_\lambda + \gamma_\rho]}{4r_e^2} \left[\frac{\sin(2\hat{k}_0 r_e) - 2\hat{k}_0 r_e \cos(2\hat{k}_0 r_e)}{2\hat{k} r_e} \right], \quad (5.27)$$

the spatial component of the homogeneous solution.

5.3.2 The Inhomogeneous Solution

To find a time dependent inhomogeneous solution $f_a^p(u)$ to equation (5.11), an ansatz of the form

$$f_a^p(u) = \int_{-\infty}^{\infty} v(b)s_a(u, b)db \quad (5.28)$$

is chosen, where

$$s_a(u, b) = \sqrt{1 + i \tan \alpha} \exp \left[-i\pi(u^2 \tan \alpha + 2ub \sec \alpha + b^2 \tan \alpha) \right]. \quad (5.29)$$

This form is chosen as s_a is the a^{th} order FrFT of the time harmonic function $\exp(i2\pi bu)$ [59] and equation (5.28) thus becomes the Fourier transform of $v(b)$ when $a = 0$. It follows that

$$\begin{aligned} \frac{\partial}{\partial u} s_a(u, b) &= \sqrt{1 + i \tan \alpha} (-2i\pi u \tan \alpha - 2i\pi b \sec \alpha) \\ &\quad \times \exp \left[-i\pi(u^2 \tan \alpha + 2ub \sec \alpha + b^2 \tan \alpha) \right], \end{aligned} \quad (5.30)$$

$$\begin{aligned} \frac{\partial^2}{\partial u^2} s_a(u, b) &= \sqrt{1 + i \tan \alpha} \left[(-2i\pi u \tan \alpha - 2i\pi b \sec \alpha)^2 \right. \\ &\quad \left. - 2i\pi \tan \alpha \right] \exp \left[-i\pi(u^2 \tan \alpha + 2ub \sec \alpha + b^2 \tan \alpha) \right]. \end{aligned} \quad (5.31)$$

Substituting these into equation (5.13) shows that the left hand side can be written as

$$\begin{aligned}
& (i2\pi)^2 \sin^2 \alpha u^2 s_a(u, b) + i4\pi \sin \alpha \cos \alpha u \frac{\partial}{\partial u} s_a(u, b) + \cos^2 \alpha \frac{\partial^2}{\partial u^2} s_a(u, b) \\
&= \sqrt{1 + i \tan \alpha} \exp \left[-i\pi(u^2 \tan \alpha + 2ub \sec \alpha + b^2 \tan \alpha) \right] \\
&\quad \times \left[-4\pi^2 \sin^2 \alpha u^2 + 8\pi^2 u^2 \sin^2 \alpha + 8\pi^2 ub \sin \alpha - 2i\pi \sin \alpha \cos \alpha \right. \\
&\quad \left. - 4\pi^2 u^2 \sin^2 \alpha - 8\pi^2 ub \sin \alpha - 4\pi^2 b^2 \right] \\
&= \sqrt{1 + i \tan \alpha} \exp \left[-i\pi(u^2 \tan \alpha + 2ub \sec \alpha + b^2 \tan \alpha) \right] (-4b^2 \pi^2 - i\pi \sin 2\alpha) \\
&= s_a(u, b) (-4b^2 \pi^2 - i\pi \sin 2\alpha), \tag{5.32}
\end{aligned}$$

which holds for all values of a . Substituting equation (5.28) into equation (5.13) then gives

$$\int_{-\infty}^{\infty} (-4b^2 \pi^2 - i\pi \sin 2\alpha) v(b) s_a(u, b) db = q_a(u). \tag{5.33}$$

Note that when u lies along the $a = 0$ axis, it is analogous to the original time domain signal. In the work below $q_0(u)$ will be written as $q(t)$ to allow for easier physical interpretation. As mentioned above, by letting $a = 0$ and $D(b) = (-4b^2 \pi^2 - i\pi \sin 2\alpha) v(b)$ in equation (5.33) (the $-i\pi \sin 2\alpha$ term must be retained to allow for general application over all a), the fractional Fourier transform of order $a = 1$ (as defined in [59]) of the function $D(b)$ is obtained,

$$\int_{-\infty}^{\infty} D(b) e^{-i2\pi tb} db = q(t). \tag{5.34}$$

It follows that, by taking the fractional Fourier transform of order $a = -1$ of both sides, that

$$D(b) = \int_{-\infty}^{\infty} q(t)e^{i2\pi tb} dt, \quad (5.35)$$

and the unknown function $v(b)$ of the integral equation (5.33) can thus be found. Note that the FrFT of order $a = -1$ is being applied to the time domain forcing function $q(t)$ to provide the inhomogeneous solution in equation (5.28). This maps the solution to the negative frequency axis. Hence, when studying the inhomogeneous solution, the FrFT of order $a = 1$ (or ordinary Fourier transform) will give rise to negative frequencies.

5.3.2.1 Fractional Fourier Transform of Order $a = -1$ of a Gaussian Modulated Linear Chirp

An analytical expression for the FrFT of order $a = -1$ of a Gaussian modulated linear chirp must now be derived. To evaluate equation (5.35), the chirp given by equation (5.1) must be rewritten in the form

$$q(t) = E_0 \exp[-(p + ir)t^2 - iw_0t]. \quad (5.36)$$

Rearranging equation (5.1), it follows that $q(t)$ can be rewritten

$$\begin{aligned} q(t) &= \exp(-2\pi i f_1(t + mt^2)) \exp\left(\frac{-(t - t_1)^2}{\sigma^2}\right) \\ &= \exp\left(-2\pi i f_1 t - 2\pi i f_1 m t^2 - \frac{(t^2 - 2t t_1 + t_1^2)}{\sigma^2}\right) \\ &= \exp\left(\frac{-t_1^2}{\sigma^2}\right) \exp\left(-\left(\frac{1}{\sigma^2} + i2\pi f_1 m\right)t^2 - i\left(2\pi f_1 + \frac{2t_1 i}{\sigma^2}\right)t\right). \end{aligned} \quad (5.37)$$

Letting $E_0 = \exp(-t_1^2/\sigma^2)$, $p = 1/\sigma^2$, $r = 2\pi f_1 m$ and $w_0 = 2\pi f_1 + 2t_1 i/\sigma^2$, equation (5.36) is obtained. Applying the fractional Fourier transform of order $a = -1$ gives

$$\begin{aligned} q_{-1}(t) &= \int_{-\infty}^{\infty} q(t) \exp[i2\pi tb] dt \\ &= \int_{-\infty}^{\infty} E_0 \exp[-(p + ir)t^2 - iw_0 t] \exp[i2\pi tb] dt \\ &= \int_{-\infty}^{\infty} E_0 \exp[-((p + ir)t^2 - i(2\pi b - w_0)t)] dt. \end{aligned} \quad (5.38)$$

Note the FrFT of order $a = -1$ is equivalent to the ordinary inverse Fourier transform and hence the variables t and b are used here in place of the more general u and u' . Note that equation (5.38) is simply the integral of a general quadratic exponent which can be solved

$$\int_{-\infty}^{\infty} \exp[-ax^2 + bx] dx = \sqrt{\frac{\pi}{a}} \exp\left[\frac{b^2}{4a}\right]. \quad (5.39)$$

It then follows that the fractional Fourier transform of order $a = -1$ of the chirp $q(t)$ can be written

$$q_{-1}(t) = \frac{\sqrt{\pi}}{\sqrt{p + ir}} E_0 \exp\left(\frac{-(2\pi b - w_0)^2}{4(p + ir)}\right). \quad (5.40)$$

From equation (5.35), $D(b) = q_{-1}(t)$ and so,

$$v(b) = \frac{\sqrt{\pi}}{\sqrt{p + ir}} \frac{E_0}{(-4b^2\pi^2 - i\pi \sin 2\alpha)} \exp\left(\frac{-(2\pi b - w_0)^2}{4(p + ir)}\right). \quad (5.41)$$

Due to the independence of $D(b)$ from u , it can be shown that this relationship between $D(b)$ and $q(u)$ holds for all orders of the FrFT. Taking the FrFT of order

a of equation (5.34) and using equation (5.29) with $a = 0$ gives

$$\mathcal{F}^a \left(\int_{-\infty}^{\infty} D(b) s_0(u, b) db \right) = \mathcal{F}^a (q_0(u)). \quad (5.42)$$

From equation (5.2) then

$$\int_{u=-\infty}^{u=\infty} K_a(u, u') \left(\int_{b=-\infty}^{b=\infty} D(b) s_0(u', b) db \right) du' = q_a(u). \quad (5.43)$$

Changing the order of integration gives

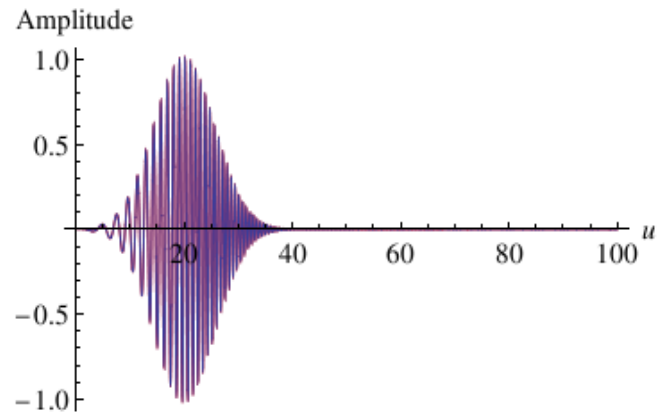
$$\int_{b=-\infty}^{b=\infty} D(b) \left(\int_{u=-\infty}^{u=\infty} K_a(u, u') s_0(u', b) du' \right) db = q_a(u), \quad (5.44)$$

and so

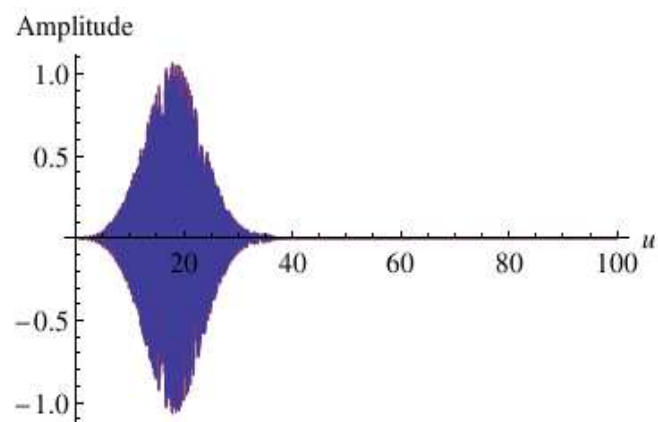
$$\int_{b=-\infty}^{b=\infty} D(b) s_a(u, b) db = q_a(u). \quad (5.45)$$

To validate that this does in fact hold true, the left hand side of equation (5.45) is plotted on top of the right hand side, for different values of a , in Figure 5.6, and it can be seen that the two are equal in every case. Finally, by equations (5.29) and (5.41), the inhomogeneous solution of the wave equation in time-frequency space is given by

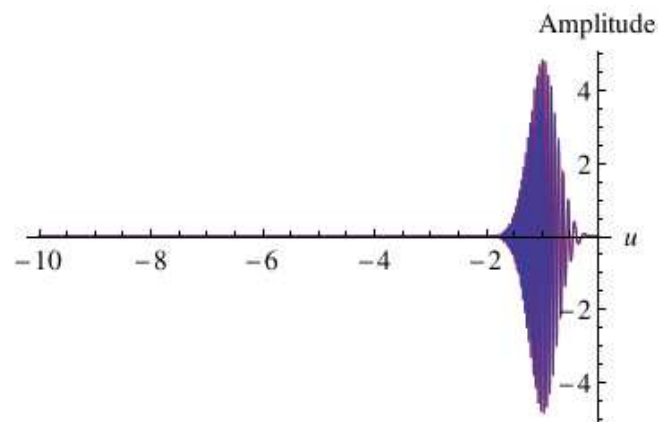
$$\begin{aligned} f_a^p(u) &= \frac{\sqrt{\pi}}{\sqrt{p+ir}} \int_{-\infty}^{\infty} \frac{E_0}{(-4b^2\pi^2 - i\pi \sin 2\alpha)} \exp\left(\frac{-(2\pi b - w_0)^2}{4(p+ir)}\right) \\ &\times \sqrt{1+i \tan \alpha} \exp(-i\pi(u^2 \tan \alpha + 2ub \sec \alpha + b^2 \tan \alpha)) db. \end{aligned} \quad (5.46)$$



(a)



(b)



(c)

Figure 5.6: To validate that equation (5.45) holds, the left hand side of the equation is plotted on top of the right hand side for different values of a : (a) 0 (b) 0.25 and (c) 1.

5.3.3 The General Solution

Having calculated the homogeneous solution and inhomogeneous solution, the general expression for the (pulse-echo) scattering from a flaw due to the excitation by a linear chirp forcing function, is given by

$$f_a(\mathbf{x}, u, b) = f_a^h(\mathbf{x}, u, b) + f_a^p(u). \quad (5.47)$$

Using equations (5.14), (5.22), (5.27) and (5.46), this can be written as

$$\begin{aligned} f_a(\mathbf{x}, u, b) = & d_1 \exp[u(-i\pi \tan \alpha u - \sqrt{-b^2 \sec^2 \alpha + i2\pi \tan \alpha})] \\ & \times h_0 \frac{e^{i\hat{k}r_s}}{r_s} \frac{a_1 a_2 a_3 [\gamma_\lambda + \gamma_\rho]}{4r_e^2} \left(\frac{\sin(2\hat{k}_0 r_e) - 2\hat{k}_0 r_e \cos(2\hat{k}_0 r_e)}{2\hat{k}_0 r_e} \right) \\ & + \frac{\sqrt{\pi}}{\sqrt{p+ir}} \int_{-\infty}^{\infty} \frac{E_0}{(-4b^2\pi^2 - i\pi \sin 2\alpha)} \exp\left(\frac{-(2\pi b - w_0)^2}{4(p+ir)}\right) \\ & \times \sqrt{1 + i \tan \alpha} \exp(-i\pi(u^2 \tan \alpha + 2ub \sec \alpha + b^2 \tan \alpha)) db. \quad (5.48) \end{aligned}$$

Note that the spatial component of the solution, which gives rise to the scattering profile of the defect and encapsulates the geometry of the flaw, is unaffected by the chirp insonification. The contribution from the chirp simply amplifies the response and should allow for an increased signal to noise ratio.

5.4 Results

A general solution to the inhomogeneous wave equation (and the scattering by a flaw) in the time-frequency domain with a Gaussian modulated linear chirp forcing function was arrived at in Section 5.3.3. It can be observed that a specific value of b is required to calculate the homogeneous solution. This part of the

solution gives rise to the scattering profile of the defect and when plotted for a specific b and every transmit/receive pair of array elements, generates a scattering matrix. The additive inhomogeneous solution does not carry flaw shape information but does involve the chirp excitation parameters. If we wish to contrast the excitation by a chirp with that of a gated continuous wave then we can restrict attention to the inhomogeneous solution only. To compute the inhomogeneous solution numerically, the infinite integral over b is approximated by the integral over the bandwidth of the transducer. This is justified as it can be assumed that the integral is zero outside this interval (the received signal will not contain any frequencies outside of the bandwidth). This approach also resolves any issues around the singularity in the integrand when $b = 0$ and $\alpha = 0$. Figure 5.7 shows two time order density plots of the inhomogeneous solution with forcing function parameters (a) $f_1 = 1\text{Hz}$, $m = 0\text{Hz}$, $t_1 = 20\text{s}$ and $\sigma = 1\mu\text{s}$ and (b) $f_1 = 0.1\text{Hz}$, $m = 0.22\text{Hz}$, $t_1 = 20\text{s}$ and $\sigma = 8\mu\text{s}$. By setting the gradient of the chirp to $m = 0$ in (a), a gated continuous wave form has been simulated. The frequency content of these signals is shown in Figure 5.2 and the bandwidths are shown to be equal thus allowing a fair comparison. The time order density plots are plotted over the range $-2 \leq u \leq 50$ to accommodate for the negative frequencies generated by taking the FrFT of order $a = -1$ of the time domain forcing function in equation (5.35). It is clear from these density plots that use of the chirp results in a greater spread of energy and that each order of the FrFT contains some signal for analysis. In the case of the gated continuous wave (plot (a)), some orders of the FrFT (for example $a = 0.55$) offer no additive amplification for the scattering matrix at any point along u . Figure 5.8 depicts the corresponding three dimensional plots to allow greater appreciation of the amplitude increase offered by use of the chirp.

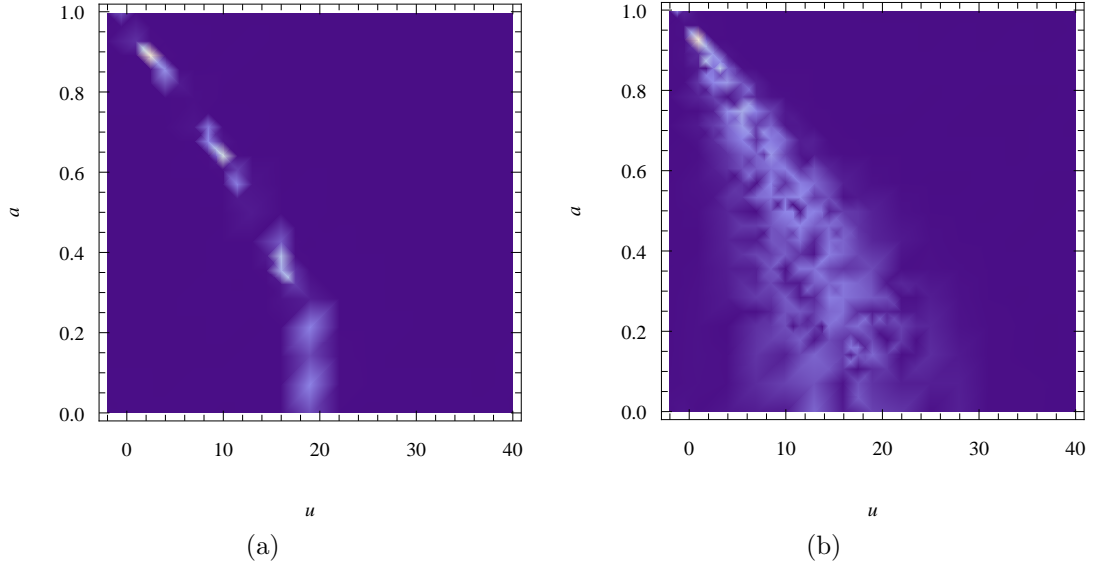
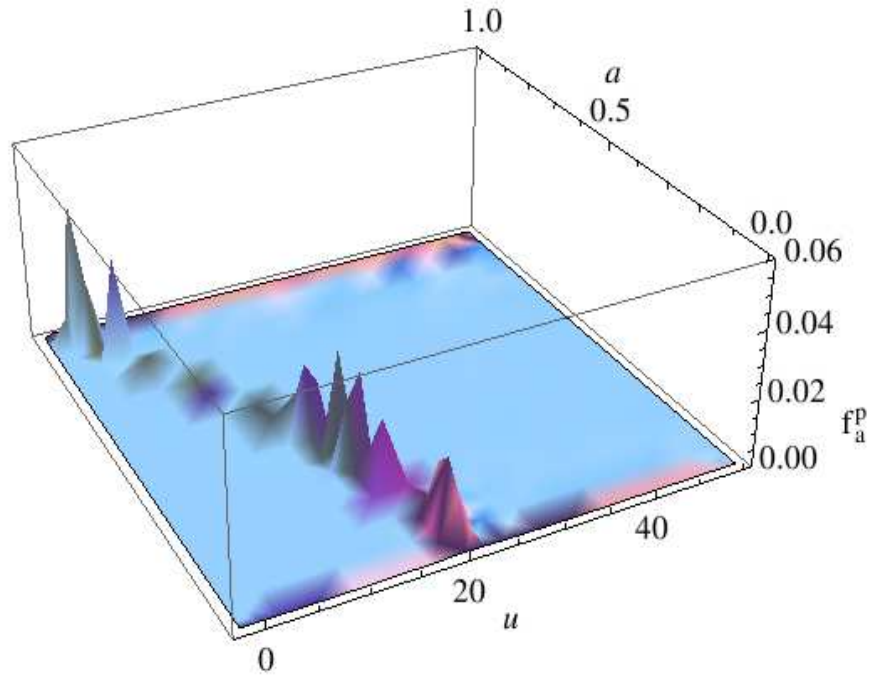


Figure 5.7: Time order density plots of the inhomogeneous solution given by equation (5.46) with chirp parameters (a) $f_1 = 1\text{Hz}$, $m = 0\text{Hz}$, $t_1 = 20\text{s}$ and $\sigma = 1\mu\text{s}$ (gated continuous wave) and (b) $f_1 = 0.1\text{Hz}$, $m = 0.22\text{Hz}$, $t_1 = 20\text{s}$ and $\sigma = 8\mu\text{s}$ (Gaussian modulated linear chirp).

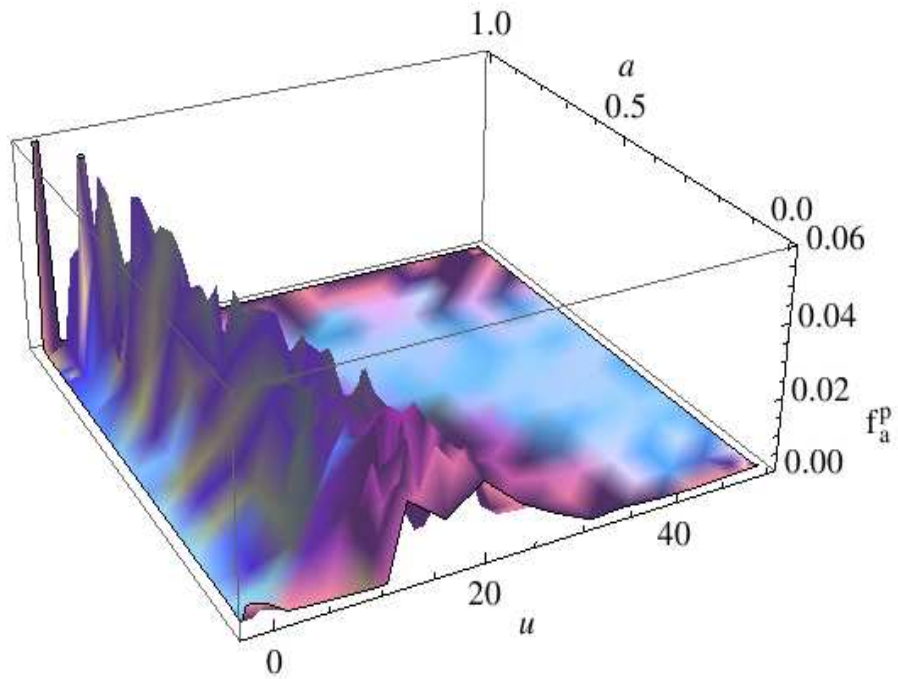
To further demonstrate the benefits of excitation by the chirp, Figure 5.9 depicts scattering matrices (previously examined in Section 3.3) arising from (a) gated continuous wave excitation and (b) linear chirp insonification, as generated via the Born approximation for a crack lying parallel to the array. Geometrically, the scattering matrices are identical, however, it can be seen that the scattering profile of the flaw is amplified in the case of chirp insonification (plot(b)). It is clear that if noise were present in the signal, the higher amplitudes exhibited in the case of chirp excitation would provide an increased signal to noise ratio.

5.4.1 Choosing the Optimal Order a

It is shown in [104] that the fractional Fourier transform of a Gaussian function has the form of a Gaussian for all orders a . The standard deviation of these



(a)



(b)

Figure 5.8: 3D surface plots of the inhomogeneous solution given by equation (5.46) with chirp parameters (a) $f_1 = 1\text{Hz}$, $m = 0\text{Hz}$, $t_1 = 20\text{s}$ and $\sigma = 1\mu\text{s}$ (gated continuous wave) and (b) $f_1 = 0.1\text{Hz}$, $m = 0.22\text{Hz}$, $t_1 = 20\text{s}$ and $\sigma = 8\mu\text{s}$ (Gaussian modulated linear chirp). 142

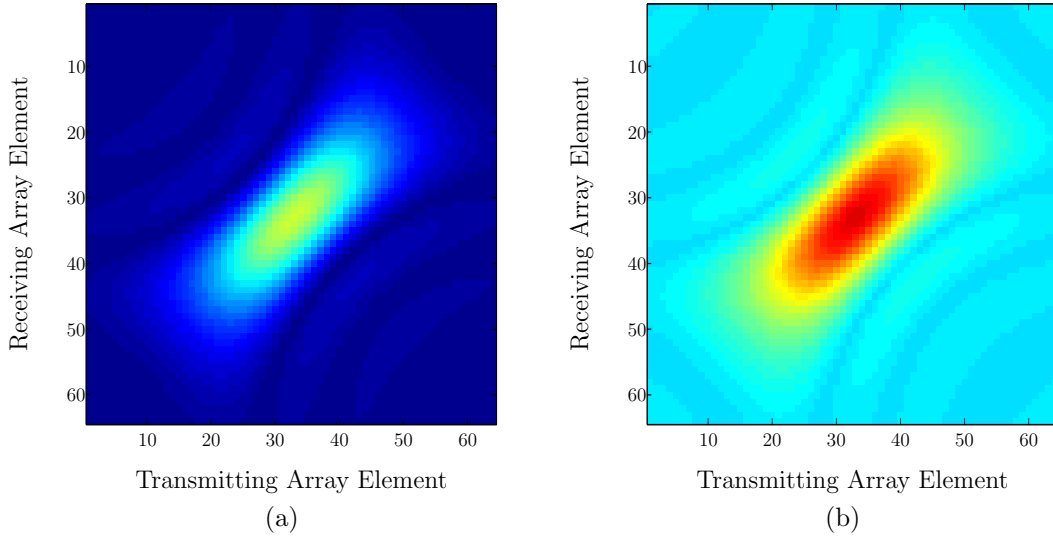


Figure 5.9: Scattering matrices as generated by the Born approximation arising from (a) gated continuous wave excitation and (b) linear chirp insonification.

Gaussian functions, σ_a , varies in time-order space, with the narrowing of the function being synonymous with an increase in maximum amplitude. Hence, it is concluded that the optimal value of a at which to employ the FrFT is the value at which the minimum σ_a occurs. As the chirp rate m increases, this maximum peak (at $\min \sigma_a$) moves further away from the frequency domain. This is explained schematically in Figures 5.10 and 5.11. The black line in Figure 5.10 represents a continuous wave (where $m = 0$) and hence results in a single value on the frequency axis. As the gradient is increased (see the red and blue lines), the breadth of the frequency spectrum increases. The curves in Figure 5.11 demonstrate how the width of the Gaussian changes in the fractional Fourier domain (of course, the Gaussian is infinite but here the width is approximated by $6\sigma_a$ as 99.73% of the signal lies within this interval). The fractional order which exhibits the widest Gaussian support is orthogonal to the order with the narrowest support and the

two are separated by order 1. It then follows that, as the bandwidth of the chirp decreases, the order at which the narrowest Gaussian support occurs, approaches the frequency domain. This can be seen in the time-order plots as shown in Figure 5.12 which arise from Gaussian modulated linear chirps with parameters (a) $m = 0.1\text{Hz}$, $t_1 = 0\text{s}$, $\sigma_0 = 8\mu\text{s}$, $f_1 = 0.1\text{Hz}$ and (b) $m = 5\text{Hz}$, $t_1 = 0\text{s}$, $\sigma_0 = 8\mu\text{s}$, $f_1 = 0.1\text{Hz}$. Plotting the rate of frequency change with respect to time of the linear

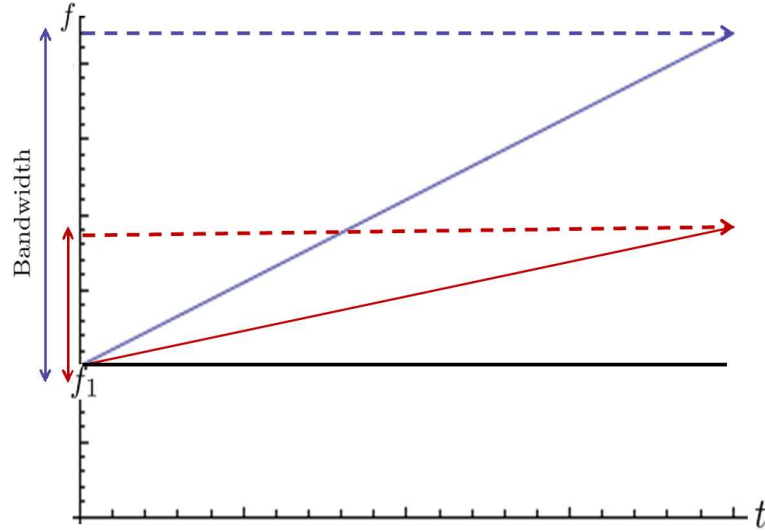


Figure 5.10: Schematic demonstrating the increase in bandwidth with the increase of chirp rate m .

chirp results in the plot as seen in Figure 5.13. The angle made with the frequency axis can thus be calculated $\alpha = \tan^{-1}(1/2f_1m)$. This provides the optimum angle at which to take the FrFT [73] and translates to order $a = 2 \tan^{-1}(1/2f_1m)/\pi$. These values have been marked by the dashed lines on the plots shown in Figure 5.12 and it can be seen that the predicted optimal order includes the highest amplitude peak. To assess the formula's success in regards to the inhomogeneous solution derived in Section 5.3.2.1, f_a^p (as defined in equation (5.46)) is plotted over orders $-2 \leq a \leq 2$ in Figure 5.14. As the Gaussian function is not centred at zero,

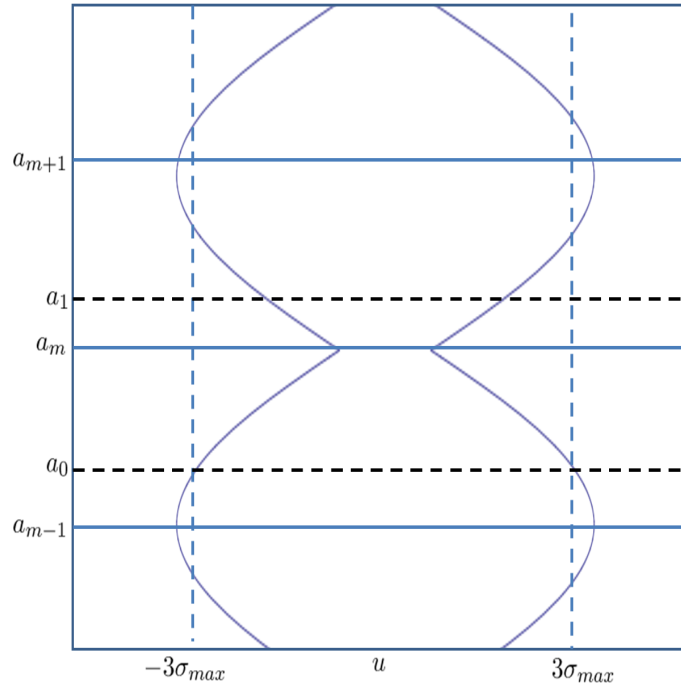


Figure 5.11: Schematic demonstrating the change in σ_a in the fractional Fourier domain [104].

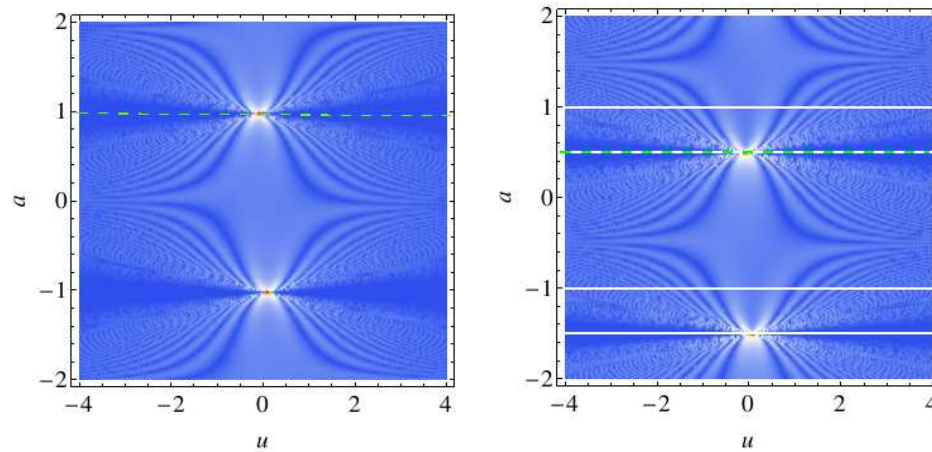


Figure 5.12: Density plots for orders $-2 \leq a \leq 2$ for Gaussian modulated linear chirps with parameters (a) $m = 0.1\text{Hz}$, $f_1 = 0.1\text{Hz}$, $\sigma = 8\mu\text{s}$ and $t_1 = 0$ and (b) $m = 5\text{Hz}$, $f_1 = 0.1\text{Hz}$, $\sigma = 8\mu\text{s}$ and $t_1 = 0$.

the plot is skewed, however the narrowing phenomena can still be observed. Due to the low gradient of the chirp excitation, the point of the minimum σ_a approaches the frequency domain as predicted. However, the simple algebraic formula derived for the optimal order of the fractional domain for the Gaussian windowed linear chirp in [73], exhibits an error in application to the inhomogeneous solution and does not incorporate the maximum amplitude (which is marked in red). However, the error is small (within 0.1 of the order at which the maximum does occur) and the formula could potentially guide the implementation of the discrete FrFT [105, 106], effectively reducing the neighbourhood (and subsequently, the computational expense) over which the FrFT is taken. It is hoped that the general solution as derived in Section 5.3.3 (equation 5.48) will act as a basis for further work on improving the extraction of the optimal order a at which to implement the FrFT for signals which have encountered a defect and been subsequently scattered, thus eventually reducing the time-order space to one dimension for numerical implementations.

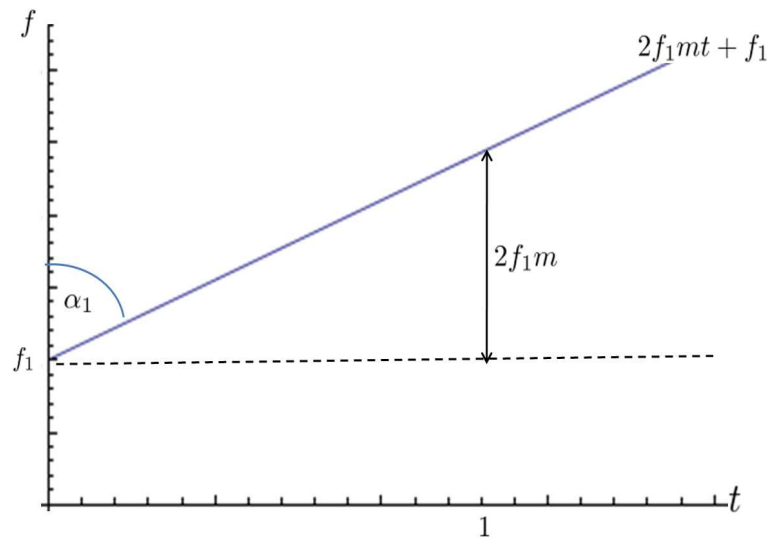


Figure 5.13: The geometrical interpretation of the optimal α at which to take the FrFT, dependent on m and f_1 .

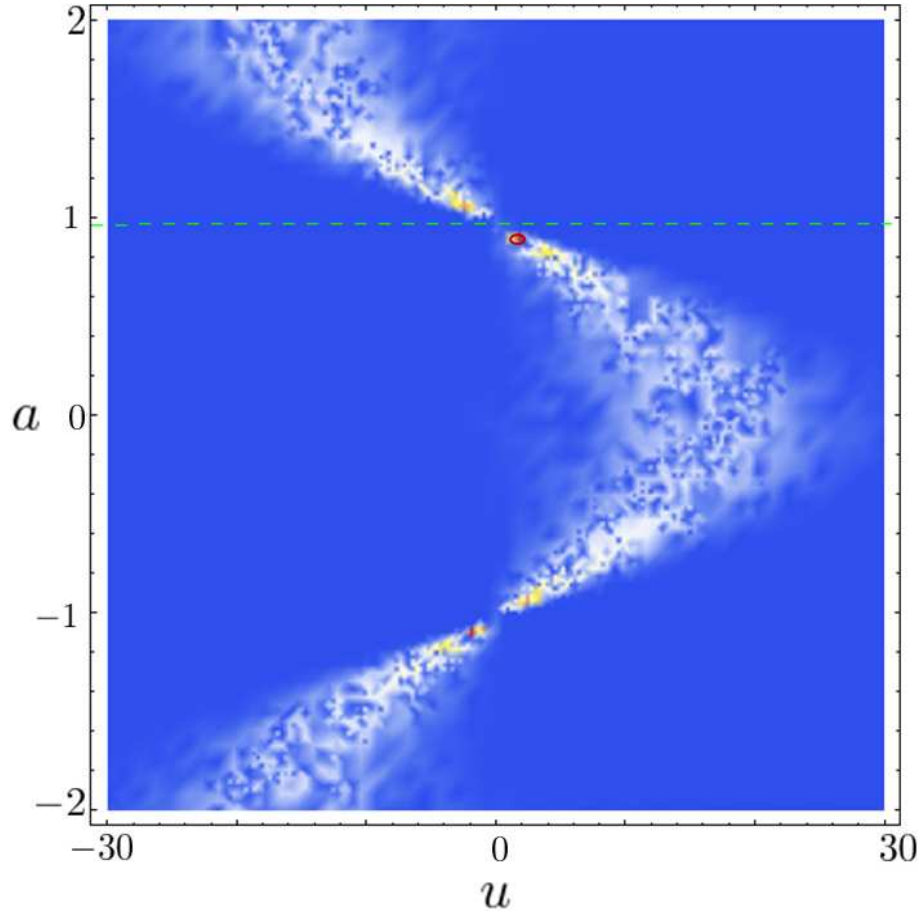


Figure 5.14: The inhomogeneous solution as given by equation (5.46), arising from linear chirp excitation with parameters $m = 0.22\text{Hz}$, $f_1 = 0.1\text{Hz}$, $\sigma = 8\mu\text{s}$ and $t_1 = 20\text{s}$. The dashed line marks the order a at which the formula derived in [73] predicts the optimal value of a should occur. The predicted optimal a does not correspond to the order at which the maximum peak occurs (which is circled in red and emphasised in Figure 5.15).

5.5 Conclusions

A general solution to the inhomogeneous wave equation, and the subsequent scattering by a flaw, in the time-frequency domain, with a Gaussian modulated linear chirp forcing function was derived in Section 5.3.3. This was achieved by taking

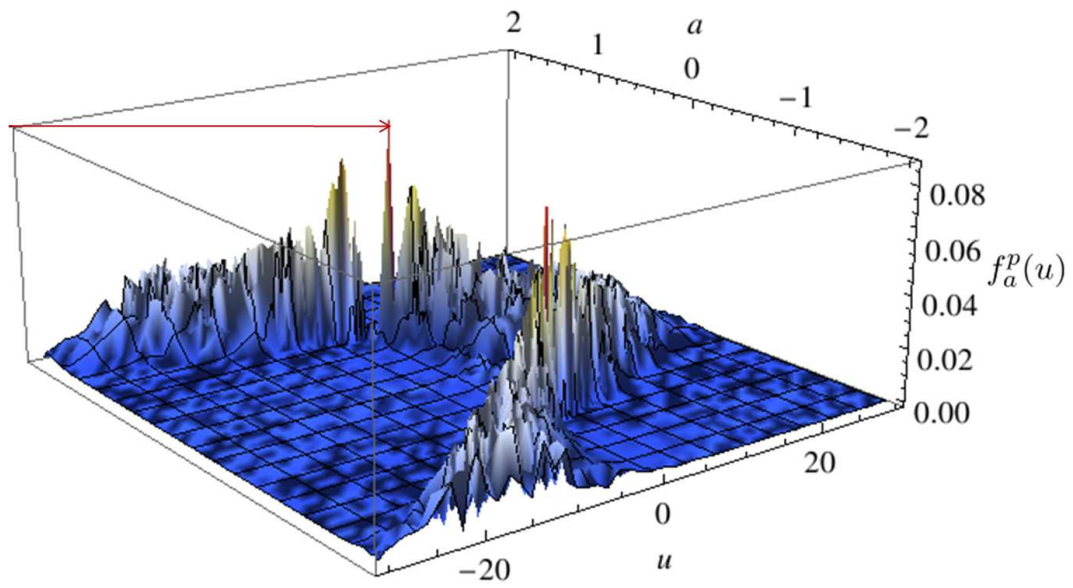


Figure 5.15: The inhomogeneous solution as given by equation (5.46), arising from linear chirp excitation with parameters $m = 0.22\text{Hz}$, $f_1 = 0.1\text{Hz}$, $\sigma = 8\mu\text{s}$ and $t_1 = 20$. The maximum peak (marked by the arrow) occurs at the optimal order at which to implement the FrFT.

the fractional Fourier transform of the inhomogeneous wave equation and finding the homogeneous solution via separation of variables and the Born approximation. The inhomogeneous solution was reached by choosing an ansatz that, once substituted into the inhomogeneous wave equation, resulted in a linear integral equation which could be solved by formulating a Fourier transform pair for a Gaussian modulated linear chirp. As we have seen in previous chapters there is a wealth of information regarding the detection, imaging and sizing of flaws contained within the scattering matrix as constructed by data arising from ultrasonic phased array inspections. Of course, the successful extraction of this information relies on the received data having a reasonable signal to noise ratio (SNR). This chapter examined the use of chirp excitation as a means of improving the SNR by increasing the amplitude of the recovered signal. Since the pulse-echo response at the ultrasonic array's centre element has the highest amplitude (for a zero degrees orientated crack) then it suffices to focus on that component of the scattering matrix. Additionally, since the excitation parameters are exclusively contained in the additive term provided by the inhomogeneous solution then again we need only focus on that term. This single value was plotted in a time-order plot for the cases where the forcing function was set as (a) a gated continuous wave and (b) a Gaussian modulated linear chirp and it was shown that, since the linear chirp contained more energy, there was a marked increase in the scattering amplitude. This was reinforced by plotting and comparing the corresponding scattering matrices for a chosen peak in the time order plot, which further demonstrated the increased amplification provided by the chirp. It is hence anticipated that an improved SNR will result when applied to experimental data. Previous work (carried out in [73, 104]) on the optimal order of a at which to implement the FrFT was

examined but fell short in application to our inhomogeneous solution. It is envisaged that the analytical formulation of the general solution in Section 5.3.3 will allow improved extraction of the optimal a for the more complicated case of a chirp which has been scattered by a defect. The benefit in doing so would be the effective reduction of the time-frequency space to one dimension, thus allowing reduced computational cost of the numerical FrFT.

Chapter 6

Conclusions

6.1 Introduction

Ultrasonic nondestructive testing can be employed to detect and characterise defects which are embedded within a wide range of components and materials, allowing for operators to anticipate failure of individual parts and subsequently implement prevention strategies. It has become increasingly popular in the last decade due to the development of multi-element piezoelectric transducer arrays which allow for greater coverage and improved control over beam directivity. However, mathematical algorithms are required to analyse and take full advantage of the extensive amount of data collected by these devices.

The focus of this thesis has been the development of novel and improved methods for the characterisation of defects using FMC data collected by ultrasonic phased array inspections. The need to reconstruct scatterers from known data has lent itself to mathematics drawn from the fields of inverse problems and scattering theory. An objective approach to crack sizing was realised via the Born

approximation and provided an analytical insight into correlations between the scattering profile of a defect and its size. This was further developed as a basis for a model-based optimisation technique, allowing for successful implementation to experimental data. Finally, the use of coded excitations and the fractional Fourier transform were explored and allowed a forward model of the scattering of a linear chirp in the time-frequency domain to be derived.

6.2 Results

Existing techniques for the detection and characterisation of defects by analysis of data arising from ultrasonic phased array inspections were examined in Chapter 2. Results by the Total Focussing Method and the Factorisation Method were displayed and compared. A disadvantage common to them both was the need for subjective thresholding of the resulting images. This weakness acted as a catalyst for the work shown in Chapters 3 and 4. In Chapter 3 an objective, model-based crack sizing algorithm was formulated using scattering theory. It has previously been shown (empirically [41]) that there exists a correlation between the cracklength and the Half-Width, Half-Maximum (HWHM) of the pulse-echo curve (the diagonal of the scattering matrix). The model based approach as developed in Chapter 3 shows analytically that given the distance between the zeros surrounding the central lobe of the scattering matrix, the crack length can be retrieved. As a result of the analytical formulation, it was possible to draw conclusions on the minimum resolvable crack length and the minimum array length required to capture the full scattering profile of the flaw. An analytical expression for the upper error bound was achieved via a Taylor expansion and allowed for

comment on the effects of array pitch and flaw depth on the accuracy of the algorithm. Finally, these conclusions were reinforced by application to scattering matrices arising from a finite element simulation of the scattering of an ultrasound wave by a crack.

Although the crack sizing algorithm as developed in Chapter 3 proved interesting from a mathematical perspective, providing analytical insight into the effects of array pitch and length, crack length to wavelength ratio, frequency and flaw depth, it was deemed unsuitable for application to experimentally collected data, due to the difficulty of extracting the zeros of the pulse-echo response curve. Hence, it was decided to use the model as a basis for an optimisation technique, which importantly retained the objectivity of the final crack length estimate. Firstly, the orientation of the crack was determined; it had already been ascertained in Chapter 3 that the location of the global maximum along the pulse-echo response was indicative of crack orientation. Next, the sum of the energy beneath the pulse-echo response curve was used to measure the similarity between the scattering matrices generated via the model and those produced by the data at a fixed frequency (typically chosen to be the central operating frequency of the transducer in the experiment). Initial results were poor but it was observed that plotting the pulse-echo response at different frequencies gave rise to a range of recovered values. Hence, a multi-frequency approach was adopted to exploit the information available over the entire bandwidth of the transducer. Unfortunately, due to anomalies caused by the resonance of heterogeneities and the consequences of dealing with experimental equipment (i.e. ring down), using the global minimum over this now two dimensional Objective Sizing matrix, was not always reliable. Therefore, it was decided to extract the minima of each matrix column, and aver-

age over all frequencies. The optimisation over the pulse-echo response was once again executed and produced promising results. However, it was realised that by only considering the N diagonal elements of the $N \times N$ matrix, useful information was being excluded. This observation gave rise to the development of the more effective full matrix optimisation technique. In application to the available experimental data, this provided an excellent objective crack length estimate of 6.2mm with 47° orientation, for an actual crack of length 6mm at 40° orientation.

Of course, any methodology relies on the signal to noise ratio (SNR) of the experimental data being above a certain threshold. In difficult materials, this can prove troublesome and so attention is turned in Chapter 5 to the use of linear chirp excitation as a means of improving SNR. A general solution to the inhomogeneous wave equation in the time-frequency domain with a Gaussian modulated linear chirp forcing function was arrived at in Section 5.3.3. This was achieved by taking the fractional Fourier transform of the inhomogeneous wave equation and finding the homogeneous solution via separation of variables and the Born approximation. The particular solution was reached by choosing an ansatz that, once substituted into the inhomogeneous wave equation, resulted in a linear integral equation which could be solved by formulating a Fourier transform pair for a Gaussian modulated linear chirp. The pulse-echo response from the arrays central element (this is the maximum value in the scattering matrix for a 0° flaw) was plotted in a time-order plot for the cases where the forcing function was set as (a) a gated continuous wave and (b) a Gaussian modulated linear chirp. It was shown that the linear chirp contained more energy and provided a far higher amplitude response. An examination of previous work on the extraction of an optimal a at which to implement the FrFT was examined and, although not precise in the case

where the chirp has encountered a defect and been subsequently scattered, it was concluded that it could guide numerical work on the FrFT, effectively reducing the range of a over which the FrFT is taken.

6.3 Future Work

Further work on improved application of the factorisation method in an NDT setting is ongoing. For example, to improve the contrast between pixels lying within the flaw domain and those lying out with, a null space is created by truncating the SVD of the scattering matrix, thus neglecting the sometimes large contributions made by the smallest eigenvalues and regularising the problem. The feasibility of a multi-frequency approach to the factorisation method is also being examined as a potential direction for future work in this area [88]. Not only would such an approach fully exploit the multi-frequency data made available by the time domain experimental data, but averaging over a range of frequencies would also minimise the contributions of ill-conditioned scattering matrices.

The analytical approach to crack sizing as developed in Chapter 3 proved to be insightful but was unsuitable for implementation to experimental data. If deviations from the smooth pulse-echo response curve could be accounted for, further applications would be possible. This could be achieved by including additional modelling aspects to the flaw scattering as modelled by the Born Approximation. Modelling considerations for future work include: the modification of the input signal by pulsers and cables, the conversion of the electrical signal into mechanical energy and back again by the transducer, the propagation path to and from the flaw, material attenuation, diffraction by scatterers, refraction in layered media,

and transmission losses at the flaw and component faces. The addition of these modelling aspects will lessen the gap between the model based scattering matrices and those generated by experimental data and hence also benefit the model based optimisation technique as developed in Chapter 4.

The work on the fractional Fourier transform shown in this thesis is still in its early stages and there exist several exciting directions in which it could be taken:

1. A natural progression of this work would be the extension of the model to the elastic case, employing the fundamental solution of Navier's equations and the reciprocal theorem for an elastic solid.
2. For application to experimental data, implementation of a numerical FrFT to the resulting FMC data is possible. Due to the analytical formulation of the time-frequency solution to the wave equation with a linear chirp forcing function reached in this work, it may be possible to improve upon the existing analytical expression for the optimal value of a at which to implement the fractional Fourier transform in the case where a chirp has been scattered by a defect. This would reduce the time-frequency space to one dimension and allow for a more efficient implementation of the numerical FrFT to experimental data, negating the need to compute the entire spectrogram.
3. The FrFT can be employed as a filtering tool. The correlation of the time-order representation of a transmitted signal with that of the resulting received signal can be computed. It has been shown (see [59]) that the correlation of the time-order representations allows for improved discrimination between correlated and uncorrelated signals over traditional time-domain correlation and could prove valuable as a signal processing technique within

the ultrasonic nondestructive testing industry.

4. From the results shown in Chapter 5, the use of linear chirps within the NDT industry is advocated as a method for improving SNR. To allow for further analysis of the benefits, a chirp function could be simulated within the PZFlex software before being implemented experimentally. Due to the additive nature of the amplification provided by the use of a chirp, the scattering profile of a defect should be less obscured by the scattering from heterogeneities at certain values of a in the time-frequency domain. If the scattering profile is successfully amplified against the noise, implementation of the model based methods as discussed in Chapters 3 and 4 may be easier.
5. Although chirp parameters were optimised to exploit the bandwidth of the transducer in Chapter 5, this was done in an ad hoc manner. It should be possible to formulate an analytical expression for the optimal m , f_1 and σ , given the bandwidth of the transducer and its central operating frequency.

6.4 Concluding Remarks

This thesis has taken steps towards developing methods for the objective characterisation of defects embedded in steel welds via the application of mathematical modelling and analysis. It is hoped that this work can be furthered to allow for practical implementation within the field of ultrasonic nondestructive testing. In particular, the work concerning the use of the fractional Fourier transform and coded excitations is in its infancy and demonstrates great potential for the improvement of both detection and characterisation of defects within highly heterogeneous media.

Appendix A

Derivation of an Explicit Expression for the Scattered Wave via the Born Approximation

To obtain an explicit expression for the scattered wave for a specific b , the Helmholtz equation

$$\nabla^2 h(\mathbf{x}) + \hat{k}^2 h(\mathbf{x}) = 0 \quad (\text{A.1})$$

where $\hat{k} = b/c$, is solved via the Born approximation. Letting $h = h^{inc} + h^{scatt}$, and assuming an initial pressure wave amplitude h_0 is present at the ultrasonic array, it can be written (from the reciprocal theorem for a fluid, the integral representation theorem [94] and the Sommerfeld radiation condition, equation (2.5)) that

$$\beta_1 h^{scatt} + \beta_2 h^{inc} = \int_{S_f} \left[h(\mathbf{x}_s, b) \frac{\partial G(\mathbf{x}_s, \mathbf{y}, b)}{\partial n(\mathbf{x}_s)} - G(\mathbf{x}_s, \mathbf{y}, b) \frac{\partial h(\mathbf{x}_s, b)}{\partial n(\mathbf{x}_s)} \right] dS(\mathbf{x}_s) \quad (\text{A.2})$$

where \mathbf{n} is the outward facing normal to V_f , the flaw volume (with surface S_f), \mathbf{x}_s is a point on the surface of the scatterer, \mathbf{y} is the point of measurement, $G(\mathbf{x}_s, \mathbf{y}, b)$ is the fundamental solution to the Helmholtz equation and

$$\beta_1 = \begin{cases} 0, & \text{if } \mathbf{y} \text{ is inside } V_f \\ 1/2, & \text{if } \mathbf{y} \text{ is on } S_f \\ 1, & \text{if } \mathbf{y} \text{ is outside } V_f \end{cases} \quad \beta_2 = \begin{cases} -1, & \text{if } \mathbf{y} \text{ is inside } V_f \\ -1/2, & \text{if } \mathbf{y} \text{ is on } S_f \\ 0, & \text{if } \mathbf{y} \text{ is outside } V_f \end{cases} . \quad (\text{A.3})$$

In equation (A.2), h and its derivative are evaluated in the host material (which will now be denoted with a positive superscript). The interface conditions of continuity of pressure and velocity over S_f can be written

$$\begin{aligned} h^+(\mathbf{x}_s, b) &= h^-(\mathbf{x}_s, b) \\ \frac{1}{\rho_0} \frac{\partial h^+(\mathbf{x}_s, b)}{\partial n(\mathbf{x}_s)} &= \frac{1}{\rho_1} \frac{\partial h^-(\mathbf{x}_s, b)}{\partial n(\mathbf{x}_s)}, \end{aligned} \quad (\text{A.4})$$

with the negative superscript indicating evaluation within the flaw medium. Hence, equation (A.2) can now be rewritten

$$\begin{aligned} \beta_1 h^{\text{scatt}}(\mathbf{y}, b) + \beta_2 h^{\text{inc}}(\mathbf{y}, b) &= \\ \int_{S_f} \left[h^-(\mathbf{x}_s, b) \nabla G(\mathbf{x}_s, \mathbf{y}, b) - \frac{\rho_0}{\rho_1} G(\mathbf{x}_s, \mathbf{y}, b) \nabla h^-(\mathbf{x}_s, b) \right] \cdot \mathbf{n}(\mathbf{x}_s) dS(\mathbf{x}_s). \end{aligned} \quad (\text{A.5})$$

By Gauss's theorem, a volume integral can be obtained

$$\begin{aligned} \beta_1 h^{\text{scatt}}(\mathbf{y}, b) + \beta_2 h^{\text{inc}}(\mathbf{y}, b) &= \\ \int_{V_f} \left[\nabla \cdot [h^-(\mathbf{x}, b) \nabla G(\mathbf{x}, \mathbf{y}, b)] - \nabla \cdot \left[\frac{\rho_0}{\rho_1} G(\mathbf{x}, \mathbf{y}, b) \nabla h^-(\mathbf{x}, b) \right] \right] dV(\mathbf{x}), \end{aligned} \quad (\text{A.6})$$

where \mathbf{x} is now any point in V_f . Using the vector identity

$$\nabla \cdot (\phi \nabla \psi) = \phi \nabla^2 \psi + \nabla \phi \cdot \nabla \psi \quad (\text{A.7})$$

it follows that

$$\nabla \cdot (h^- \nabla G) = h^- \nabla^2 G + \nabla h^- \cdot \nabla G \quad (\text{A.8})$$

and

$$\nabla \cdot \left[\left(\frac{\rho_0}{\rho_1} \nabla h^- \right) G \right] = \nabla \cdot \left(\frac{\rho_0}{\rho_1} \nabla h^- \right) G + \left(\frac{\rho_0}{\rho_1} \nabla h^- \right) \cdot \nabla G. \quad (\text{A.9})$$

Since G is the fundamental solution to the Helmholtz equation then, outside V_f ,

$$\nabla^2 G + \frac{b^2}{c_0^2} G = -\delta(\mathbf{x} - \mathbf{y}). \quad (\text{A.10})$$

From equation (A.1), it can also be seen that within the flaw

$$\nabla \cdot \left(\frac{\rho_0}{\rho_1} \nabla h^- \right) = -\frac{\rho_0}{\rho_1} \frac{b^2}{c_1^2} h^-. \quad (\text{A.11})$$

Returning to the physical scenario, if \mathbf{y} is the point of reception at the array (see Figure A.1), $\mathbf{y} \notin V_f$ and hence $\alpha = 1$, $\beta = 0$ (equation (A.3)) and $\delta(\mathbf{x} - \mathbf{y}) = 0$ by the sampling property. It then follows from equations (A.6), (A.7)-(A.11) that

$$\begin{aligned} h^{\text{scatt}}(\mathbf{y}, b) &= \int_{V_f} \left(1 - \frac{\rho_0}{\rho_1} \right) \nabla h^- \cdot \nabla G - \left(\frac{b^2}{c_0^2} - \frac{\rho_0}{\rho_1} \frac{b^2}{c_1^2} \right) G h^- dV_f \\ &= \int_{V_f} \left(1 - \frac{\rho_0}{\rho_1} \right) \nabla h^- \cdot \nabla G - \frac{b^2}{c_0^2} \left(1 - \frac{\lambda_0}{\lambda_1} \right) G h^- dV_f \\ &= \int_{V_f} \gamma_\rho \nabla h^- \cdot \nabla G - \frac{b^2}{c_0^2} \gamma_\lambda G h^- dV_f \end{aligned} \quad (\text{A.12})$$

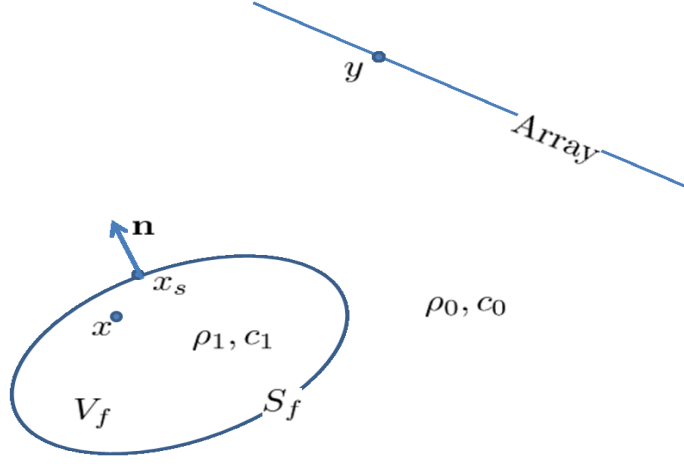


Figure A.1: V_f is a volumetric flaw in the far field of the ultrasonic transducer. The ultrasonic array has transmitting and receiving elements at position $y \notin V_f$ on the array. ρ and c are the density and pressure wave velocity respectively, where the subscript 0 indicates they are measured in the host medium and the subscript 1 indicates they are measured in the flaw.

where $c_i^2 = \lambda_i/\rho_i$, with λ_i the bulk modulus and ρ_i the material density, $\gamma_\rho = 1 - \rho_0/\rho_1$ and $\gamma_\lambda = 1 - \lambda_0/\lambda_1$. The far field approximations (when $|\mathbf{y}| \gg |\mathbf{x}|$) of G and its derivatives are given by [94]

$$G = \frac{e^{ikr_s}}{4\pi r_s} e^{-i\hat{\mathbf{k}}\mathbf{x}\cdot\mathbf{e}_s}$$

$$\frac{\partial G}{\partial x_m} = -i\hat{k}e_{sm} \frac{e^{ikr_s}}{4\pi r_s} e^{-i\hat{\mathbf{k}}\mathbf{x}\cdot\mathbf{e}_s}, \quad (\text{A.13})$$

where $\hat{k}_0 = b/c_0$, $\mathbf{e}_s = \hat{\mathbf{y}}$ is the scattered wave direction and $r_s = |\mathbf{y}|$ is the distance of the receiving element on the ultrasonic array from the flaw. Substituting these into equation (A.12) gives

$$h^{scatt}(\mathbf{y}, b) = \frac{e^{i\hat{k}_0 r_s}}{4\pi r_s} \int_{V_f} \left[-i\hat{k}_0 \gamma_\rho (\mathbf{e}_s \cdot \nabla h^-) - \hat{k}_0^2 \gamma_\lambda h^- \right] \exp(-i\hat{k}_0 \mathbf{e}_s \cdot \mathbf{x}) dV \quad (\text{A.14})$$

The scattered wave can also be written in the form [94]

$$h^{scatt}(\mathbf{y}, b) = h_0 A(\mathbf{e}_i; \mathbf{e}_s) \frac{e^{i\hat{k}_0 r_s}}{r_s}, \quad (\text{A.15})$$

where h_0 is the initial pressure amplitude and $A(\mathbf{e}_i; \mathbf{e}_s)$ is the far field scattering amplitude (where \mathbf{e}_i and \mathbf{e}_s are the incident and scattered wave directions respectively). Letting $\tilde{h} = h^-/h_0$, it follows that

$$A(\mathbf{e}_i; \mathbf{e}_s) = -\frac{1}{4\pi} \int_{V_f} \left[i\hat{k}_0 \gamma_\rho (\mathbf{e}_s \cdot \nabla \tilde{h}) + \hat{k}_0^2 \gamma_\lambda \tilde{h} \right] \exp(-i\hat{k}_0 \mathbf{e}_s \cdot \mathbf{x}) dV \quad (\text{A.16})$$

To obtain an explicit expression an approximation is introduced. It is assumed in the Born approximation that the material properties of the host and flaw media are similar, and so the pressure field \tilde{h} and its derivatives can be obtained from their values due to the incident wave only, and hence it is assumed that

$$\tilde{h} = \exp(i\hat{k}_0 \mathbf{e}_i \cdot \mathbf{x})$$

and

$$\nabla \tilde{h} = i\hat{k}_0 \mathbf{e}_i \exp(i\hat{k}_0 \mathbf{e}_i \cdot \mathbf{x}). \quad (\text{A.17})$$

Assuming that the flaw is of a homogeneous nature (so that ρ_1 and λ_1 are constant), then

$$A(\mathbf{e}_i; \mathbf{e}_s) = -\frac{\hat{k}_0^2 [\gamma_\lambda - \gamma_\rho (\mathbf{e}_i \cdot \mathbf{e}_s)]}{4\pi} \int_{V_f} \exp[i\hat{k}_0 (\mathbf{e}_i - \mathbf{e}_s) \cdot \mathbf{x}] dV(\mathbf{x}). \quad (\text{A.18})$$

The integral in equation (A.18) is of course related to the geometry of the flaw via V_f . To make further analytical headway it is assumed that the flaw is an

ellipsoid with axes lengths given by a_1 , a_2 and a_3 . Using the stretched coordinates $\mathbf{y} = (a_1x_1, a_2x_2, a_3x_3)$ then converts the flaw volume to that of a sphere. Let us define the unit vector in the direction of $\mathbf{e}_i - \mathbf{e}_s$ as

$$\mathbf{e}_q = \frac{\mathbf{e}_i - \mathbf{e}_s}{|\mathbf{e}_i - \mathbf{e}_s|}. \quad (\text{A.19})$$

Expressing this vector using the basis vectors \mathbf{u} that are aligned with the main axes of the ellipsoid gives

$$\begin{aligned} (\mathbf{e}_i - \mathbf{e}_s) \cdot \mathbf{x} &= |\mathbf{e}_i - \mathbf{e}_s| \mathbf{e}_q \cdot \mathbf{x} \\ &= |\mathbf{e}_i - \mathbf{e}_s| \mathbf{r}_e \cdot \mathbf{y} \end{aligned} \quad (\text{A.20})$$

where

$$\mathbf{r}_e = a_1(\mathbf{e}_q \cdot \mathbf{u}_1)\mathbf{u}_1 + a_2(\mathbf{e}_q \cdot \mathbf{u}_2)\mathbf{u}_2 + a_3(\mathbf{e}_q \cdot \mathbf{u}_3)\mathbf{u}_3. \quad (\text{A.21})$$

Substituting this into equation (A.18) the integral term $S(\mathbf{e}_i; \mathbf{e}_s, b)$ becomes

$$S(\mathbf{e}_i; \mathbf{e}_s, b) = a_1 a_2 a_3 \int_{V'} \exp[i\hat{k}_0 |\mathbf{e}_i - \mathbf{e}_s| \mathbf{r}_e \cdot \mathbf{y}] dy_1 dy_2 dy_3 \quad (\text{A.22})$$

where V' is a unit radius sphere. Using a spherical coordinate system with the z -axis lying along the effective radius of the flaw \mathbf{r}_e , this can be written

$$\begin{aligned} S(\mathbf{e}_i; \mathbf{e}_s, b) &= a_1 a_2 a_3 \int_{r=0}^{r=1} \int_{\theta=0}^{\theta=\pi} \int_{\phi=0}^{\phi=2\pi} \exp\left(i\hat{k}_0 |\mathbf{e}_i - \mathbf{e}_s| r_e r \cos\theta\right) r^2 \sin\theta d\phi d\theta dr \\ &= 2\pi a_1 a_2 a_3 \int_{r=0}^{r=1} \int_{\theta=0}^{\theta=\pi} \exp\left(i\hat{k}_0 |\mathbf{e}_i - \mathbf{e}_s| r_e r \cos\theta\right) r^2 \sin\theta d\theta dr \end{aligned} \quad (\text{A.23})$$

Letting $u = \cos \theta$ and $du = -\sin \theta d\theta$, it follows

$$\begin{aligned} S(\mathbf{e}_i; \mathbf{e}_s, b) &= 2\pi a_1 a_2 a_3 \int_{r=0}^{r=1} \int_{u=-1}^{u=1} \exp(i\hat{k}_0 |\mathbf{e}_i - \mathbf{e}_s| r_e r u) r^2 du dr \\ &= \frac{4\pi a_1 a_2 a_3}{\hat{k}_0 |\mathbf{e}_i - \mathbf{e}_s| r_e} \int_0^1 r \sin(\hat{k}_0 |\mathbf{e}_i - \mathbf{e}_s| r_e r) dr. \end{aligned} \quad (\text{A.24})$$

Using integration by parts gives

$$S(\mathbf{e}_i; \mathbf{e}_s, b) = \frac{4\pi a_1 a_2 a_3}{\hat{k}_0 |\mathbf{e}_i - \mathbf{e}_s| r_e} \left[\frac{\sin(\hat{k}_0 |\mathbf{e}_i - \mathbf{e}_s| r_e) - \hat{k}_0 |\mathbf{e}_i - \mathbf{e}_s| r_e \cos(\hat{k}_0 |\mathbf{e}_i - \mathbf{e}_s| r_e)}{(\hat{k}_0 |\mathbf{e}_i - \mathbf{e}_s| r_e)^2} \right]. \quad (\text{A.25})$$

By combining equations (A.15), (A.18) and (A.25), the scattered pressure wave can now be written explicitly as

$$\begin{aligned} h(\mathbf{y}, b) &= h_0 \frac{e^{i\hat{k}_0 r_s}}{r_s} \\ &\times \frac{a_1 a_2 a_3 (\gamma_\lambda - \gamma_\rho (\mathbf{e}_i \cdot \mathbf{e}_s))}{|\mathbf{e}_i - \mathbf{e}_s|^2 r_e^2} \left(\frac{\sin(\hat{k}_0 |\mathbf{e}_i - \mathbf{e}_s| r_e) - \hat{k}_0 |\mathbf{e}_i - \mathbf{e}_s| r_e \cos(\hat{k}_0 |\mathbf{e}_i - \mathbf{e}_s| r_e)}{\hat{k}_0 |\mathbf{e}_i - \mathbf{e}_s| r_e} \right). \end{aligned} \quad (\text{A.26})$$

For the purposes of Chapter 5 it is enough to only consider the pulse-echo case (where $\mathbf{e}_i = -\mathbf{e}_s$) and so equation (A.26) becomes

$$h(\mathbf{y}, b) = h_0 \frac{e^{i\hat{k}_0 r_s}}{r_s} \frac{a_1 a_2 a_3 [\gamma_\lambda + \gamma_\rho]}{4r_e^2} \left[\frac{\sin(2\hat{k}_0 r_e) - 2\hat{k}_0 r_e \cos(2\hat{k}_0 r_e)}{2\hat{k}_0 r_e} \right], \quad (\text{A.27})$$

which supplies the spatial component of the homogeneous solution in equation (5.14)

Appendix B

Finite Element Data as Simulated in the Software Package PZFlex

One method used in this thesis to model the array system and material properties of a weld is the finite element method. This was implemented using the software package PZFlex [107]. This model allows for consideration of both homogeneous and inhomogeneous host materials. The inhomogeneous case incorporates experimentally obtained electron back scatter diffraction (EBSD) measurements of the internal microstructure of an austenitic steel weld [108] allowing for a more accurate realisation of the problem. The simulation also includes the transmit and receive effects of a linear array (with parameters as listed in the tables below) situated directly above the weld (see Figure B). For the homogeneous case, the transducer effects are still incorporated but the microstructure is ‘switched off’ to simulate a perfectly homogeneous medium. Within both geometries, a series of flaws have been inserted into the simulations including side drilled holes of varying size and zero volume flaws (cracks) at differing locations and orientations. This

large library of simulations is an excellent test bed for the development and implementation of imaging algorithms. Figure B depicts a schematic of the PZFlex finite element simulation. The array is placed directly above the weld, with an absorbing water layer at the back wall. The white disc represents a simulated flaw within the weld. The weld consists of a single material (Inconel) which is anisotropic and, due to thermal effects as the weld is forming, forms a spatially heterogeneous structure due to local fluctuations in the orientation of each crystal. Each colour within the weld represents a different orientation of grain, creating the inhomogeneous nature of the medium [108].

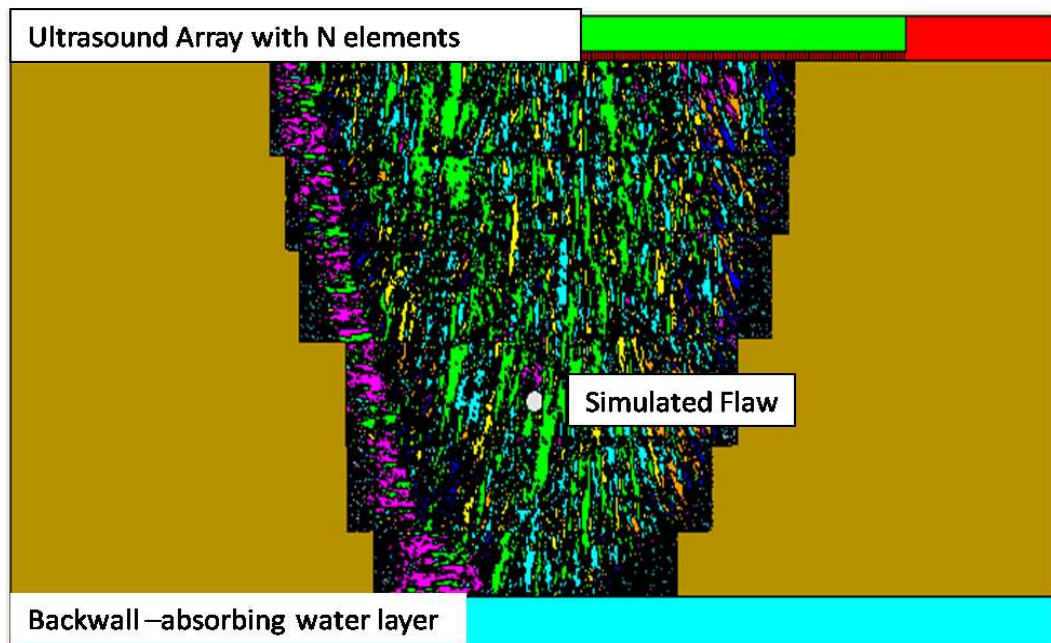


Figure B.1: Internal microstructure of an austenitic steel weld as input into the finite element model implemented in the software package PZFlex. The different colours signify the grain structure in the material where each colour represents a particular grain orientation.

| Ultrasonic Transducer Array Parameter | Value | Unit |
|------------------------------------------------------|--------|-------------------|
| Number of Array Elements | 64 | - |
| Pitch | 2 | mm |
| Array Element Width | 1.5 | mm |
| Transducer Centre Frequency | 1.5 | MHz |
| Density of Host Material | 8280 | kg/m ³ |
| Pressure Wave Velocity in Host Material (c_{P0}) | 7400 | m/s |
| Shear Wave Velocity in Host Material(c_{s0}) | 3000 | m/s |
| Flaw type | crack | - |
| Flaw radius | 2.5 | mm |
| Flaw Orientation | 0 - 40 | ° |
| Distance of Flaw from Array | 50 | mm |
| Depth of Sample | 76.8 | mm |

Table B.1: Data A1 - Zero Volume Flaw in Homogeneous Medium

| Ultrasonic Transducer Array Parameter | Value | Unit |
|------------------------------------------------------|--------|-------------------|
| Number of Array Elements | 64 | - |
| Pitch | 2 | mm |
| Array Element Width | 1.5 | mm |
| Transducer Centre Frequency | 1.5 | MHz |
| Density of Host Material | 8280 | kg/m ³ |
| Pressure Wave Velocity in Host Material (c_{P0}) | 5700 | m/s |
| Shear Wave Velocity in Host Material(c_{s0}) | 3000 | m/s |
| Flaw type | crack | - |
| Flaw radius | 2.5 | mm |
| Flaw Orientation | 0 - 40 | ° |
| Distance of Flaw from Array | 50 | mm |
| Depth of Sample | 76.8 | mm |

Table B.2: Data A2 - Zero Volume Flaw in Inhomogeneous Medium (Inconel)

Appendix C

Experimentally Collected Data

Through collaboration with the industrial sponsors of this project - Amec, NNL, Rolls Royce, Shell and Weidlinger, and staff at the Centre of Ultrasonic Engineering in the department of Electronic and Electrical Engineering at the University of Strathclyde, I have had access to experimentally collected ultrasonic data from sample materials with defects embedded within. The tables below detail the experimental parameters used for each experimental dataset referred to throughout this thesis.

| Ultrasonic Transducer Array Parameter | Value | Unit |
|------------------------------------------------------|-------|-------------------|
| Number of Array Elements | 45 | - |
| Pitch | 0.7 | mm |
| Array Element Width | 1.5 | mm |
| Transducer Centre Frequency | 5 | MHz |
| Density of Host Material | 8280 | kg/m ³ |
| Pressure Wave Velocity in Host Material (c_{P0}) | 5700 | m/s |
| Shear Wave Velocity in Host Material(c_{s0}) | 3000 | m/s |
| Flaw type | crack | - |
| Flaw radius | 6 | mm |
| Flaw Orientation | 90 | ° |
| Distance of Flaw from Array | 35 | mm |
| Depth of Sample | 85 | mm |

Table C.1: Data B1 - Zero Volume Flaw Embedded in an Inconel Weld

| Ultrasonic Transducer Array Parameter | Value | Unit |
|------------------------------------------------------|-------|-------------------|
| Number of Array Elements | 128 | - |
| Pitch | 0.7 | mm |
| Array Element Width | 1.5 | mm |
| Transducer Centre Frequency | 5 | MHz |
| Density of Host Material | 7830 | kg/m ³ |
| Pressure Wave Velocity in Host Material (c_{P0}) | 5820 | m/s |
| Shear Wave Velocity in Host Material(c_{s0}) | 3100 | m/s |
| Flaw type | crack | - |
| Flaw radius | 3 | mm |
| Flaw Orientation | 40 | ° |
| Distance of Flaw from Array | 16 | mm |
| Depth of Sample | 22 | mm |

Table C.2: Data B2 - Zero Volume Lack of Fusion Flaw in Stainless Steel

Bibliography

- [1] B. Chassignole, D. Villard, M. Dubuget, J.C. Baboux, and R. El Guerjouma. Characterization of Austenitic Stainless Steel Welds for Ultrasonic NDT. *Review of Progress in Quantitative Nondestructive Evaluation*, 19:1325–1332, 2000.
- [2] J.P. Charlesworth and J.A.G. Temple. *Engineering Applications of Ultrasonic Time-of-Flight-Diffraction*. Research Studies Press, Baldock, Hertfordshire, 2001.
- [3] B.W. Drinkwater and P.D. Wilcox. Ultrasonic Arrays for Non-destructive Evaluation: A Review. *NDT & E Int*, 39(7):525–541, 2006.
- [4] O. Oralkan, A.S. Ergun, J.A. Johnson, M. Karaman, U. Demirci, K. Kaviani, T.H. Lee, and B.T. Khuri-Yakub. Capacitive Micromachined Ultrasonic Transducers: Next-generation Arrays for Acoustic Imaging? *IEEE TUFFC*, 49(11):1596–1610, 2002.
- [5] J.F.C. Windmill, J.C. Jackson, E.J. Tuck, and D. Robert. Keeping Up with Bats: Dynamic Auditory Tuning in a Moth. *Current Biology*, 16(24):2418–2423, 2006.

- [6] D.R. Griffin, F.A Webster, and C.R. Michael. The Echolocation of Flying Insects by Bats. *Animal Behaviour*, 8(3):141–154, 1960.
- [7] W.W.L Au, P.W.B. Moore, and D.A. Pawloski. Detection of Complex Echoes in Noise by an Echolocating Dolphin. *JASA*, 83(2):662–668, 1988.
- [8] R. Hershkovitz, E. Sheiner, and M. Mazor. Ultrasound in Obstetrics: A Review of Safety. *European Journal of Obstetrics & Gynecology and Reproductive Biology*, 101(1):15–18, 2002.
- [9] K.R. Erikson, F.J. Fry, and J.P. Jones. Ultrasound in Medicine: A Review. *IEEE Transactions on Sonics and Ultrasonics*, 21(3):144–170, 1974.
- [10] A. Fenster and D.B. Downey. 3-D Ultrasound Imaging: A Review. *Engineering in Medicine and Biology Magazine, IEEE*, 15(6):41–51, 1996.
- [11] J. Webster. *Wiley Encyclopedia of Electrical and Electronics Engineering*. John Wiley & Sons, Inc, 1999.
- [12] C.F. Brockelsby. Some Applications of Ultrasonics. *Journal of Scientific Instruments*, 40(4):153, 1963.
- [13] Peter J Shull. *Nondestructive Evaluation: Theory, Techniques, and Applications*. CRC press, 2002.
- [14] J.R. Wait. Review of Electromagnetic Methods in Nondestructive Testing of Wire Ropes. *Proceedings of the IEEE*, 67(6):892–903, 1979.
- [15] G.Y. Tian, L. Cheng, Y. Cheng, and F. Yang. Electromagnetic Non-Destructive Evaluation for Safety Critical Components and Material. In

2013 21st International Conference on Nuclear Engineering. American Society of Mechanical Engineers, 2013.

- [16] M. Reiter, B. Harrer, C. Heinzl, D. Salaberger, C. Gusenbauer, C. Kuhn, and J. Kastner. Simulation Aided Study for Optimising Industrial X-ray CT Scan Parameters for Non-Destructive Testing and Materials Characterisation. *Proc. Int. Symp. on Digital Ind. Radiology and CT, CD-ROM*, 6:20–22, 2011.
- [17] V. Vavilov. Noise-limited Thermal/Infrared Nondestructive Testing. *NDT & E Int*, 61:16–23, 2014.
- [18] B. Yang and D. Sun. Testing, Inspecting and Monitoring Technologies for Wind Turbine Blades: A Survey. *Renewable and Sustainable Energy Reviews*, 22:515–526, 2013.
- [19] M. Cherfaoui. Innovative Techniques in Non-Destructive Testing and Industrial Applications on Pressure Equipment. *Procedia Engineering*, 46:266–278, 2012.
- [20] H.W. Liu, S.P. Zhan, Y.H. Du, and P. Zhang. Study on Pulsed Eddy Current Nondestructive Testing Technology for Pipeline Corrosion Defects Based on Finite Element Method. *Applied Mechanics and Materials*, 120:36–41, 2012.
- [21] J.W. Fan and F.T. Tan. Analysis of Major Defects and Nondestructive Testing Methods for Solid Rocket Motor. *Applied Mechanics and Materials*, 365:618–622, 2013.
- [22] H. Jaffe and D.A. Berlincourt. Piezoelectric Transducer Materials. *Proceedings of the IEEE*, 53(10):1372–1386, 1965.

- [23] K.K. Shung and M Zippuro. Ultrasonic Transducers and Arrays. *Engineering in Medicine and Biology Magazine, IEEE*, 15(6):20–30, 1996.
- [24] C. Holmes, B.W. Drinkwater, and P.D. Wilcox. Post Processing of the Full Matrix of Ultrasonic Transmit Receive Array Data for Non Destructive Evaluation. *NDT & E Int*, 38(8):701–711, 2005.
- [25] J. Davies, F. Simonetti, M. Lowe, and P. Cawley. Review of Synthetically Focused Guided Wave Imaging Techniques with Application to Defect Sizing. *AIP Conf. Proc.*, 820:142–149, 2006.
- [26] J. Lambert, A. Pedron, G. Gens, F. Bimbard, L. Lacassagne, and E. Iakovleva. Performance Evaluation of Total Focusing Method on GPP and GPU. *Conference on Design and Architectures for Signal and Image Processing (DASIP)*, pages 1–8, 2012.
- [27] C. Li, D. Pain, B.W. Drinkwater, and P.D. Wilcox. Imaging Composite Material Using Ultrasonic Arrays. *NDT & E Int*, 53:8–17, 2013.
- [28] J. Zhang, B.W. Drinkwater, P.D. Wilcox, and A.J. Hunter. Defect Detection Using Ultrasonic Arrays: The Multi-Mode Total Focusing Method. *NDT & E Int*, 43(2):123–133, 2009.
- [29] L. Borcea, G. Papanicolaou, and C. Tsogka. Interferometric Array Imaging in Clutter. *Inverse Problems*, 21:1419–1560, 2005.
- [30] L. Borcea, G. Papanicolaou, and C. Tsogka. Coherent Interferometric Imaging in Clutter. *Geophysics*, 71(4):165–175, 2006.

- [31] L. Borcea, G. Papanicolaou, and C. Tsogka. Adaptive Time-Frequency Detection and Filtering for Imaging in Heavy Clutter. *SIAM Journal on Imaging Sciences*, 54(8):1541–1550, 2007.
- [32] L. Borcea, J. Garnier, G. Papanicolaou, and C. Tsogka. Coherent Interferometric Imaging, Time Gating and Beamforming. *Inverse Problems*, 27(6):065008, 2011.
- [33] L. Borcea, G. Papanicolaou, and C. Tsogka. Adaptive Interferometric Imaging in Clutter and Optimal Illumination. *Inverse Problems*, 22:1405–1436, 2006.
- [34] J. Camacho, M. Parrilla, and C. Fritsch. Phase Coherence Imaging. *IEEE TUFFC*, 56(5):958–974, 2009.
- [35] J. Zhang, B.W. Drinkwater, and P.D. Wilcox. Comparison of Ultrasonic Array Imaging Algorithms for Nondestructive Evaluation. *IEEE TUFFC*, 60(8):1732–1745, 2013.
- [36] A. Kirsch and N. Grinberg. *The Factorisation Method for Inverse Problems*. Oxford University Press, Oxford, 2008.
- [37] D. Colton and A. Kirsch. A Simple Method for Solving Inverse Problems in the Resonance Region. *Inverse Problems*, 12:383–393, 1996.
- [38] M. Ikehata. Reconstruction of the Shape of the Inclusion by Boundary Measurements. *Commun. Partial Differ. Equations*, 23:1459–1474, 1998.

- [39] R. Potthast. Stability Estimates and Reconstructions in Inverse Acoustic Scattering Using Singular Sources. *J. Comput. Appl. Math*, 114:247–274, 2000.
- [40] J. Zhang, B.W. Drinkwater, and P.D. Wilcox. Defect Characterization Using an Ultrasonic Array to Measure the Scattering Coefficient Matrix. *IEEE TUFFC*, 55(10):2254–2265, 2008.
- [41] J. Zhang, B.W. Drinkwater, and P.D. Wilcox. The Use of Ultrasonic Arrays to Characterize Crack-like Defects. *J NDE*, 29(4):222–232, 2010.
- [42] G.D. Connolly, M.J.S. Lowe, J.A.G. Temple, and S.I. Rokhlin. Correction of Ultrasonic Array Images to Improve Reflector Sizing and Location in Inhomogeneous Materials Using a Ray-Tracing Model. *JASA*, 127(5):2802–2812, 2010.
- [43] S.D Sharples, M. Clark, and M.G. Somekh. Spatially Resolved Acoustic Spectroscopy for Fast Noncontact Imaging of Material Microstructure. *Optics Express*, 14(22):10435–10440, 2006.
- [44] W. Li, S.D. Sharples, R.J. Smith, M. Clark, and M.G. Somekh. Determination of Crystallographic Orientation of Large Grain Metals with Surface Acoustic Waves. *JASA*, 132(2):738–745, 2012.
- [45] A.J. Schwartz, M. Kumar, B.L. Adams, and D.P. Field. *Electron Backscatter Diffraction in Materials Science*, volume 2. Springer, 2009.
- [46] J. Zhang, A. Hunter, B.W. Drinkwater, and P.D. Wilcox. Monte Carlo Inversion of Ultrasonic Array Data to Map Anisotropic Weld Properties. *IEEE TUFFC*, 59(11):2487–2497, 2012.

- [47] O. Nowers, D.J. Duxbury, J. Zhang, and B.W. Drinkwater. Novel Ray-Tracing Algorithms in NDE: Application of Dijkstra and A* Algorithms to the Inspection of an Anisotropic Weld. *NDT & E Int*, 61:58–66, 2014.
- [48] K.A. Woodbury. *Inverse Engineering Handbook*. CRC Press, Florida, 2003.
- [49] A. Kirsch. *An Introduction to the Mathematical Theory of Inverse Problems*. Springer, 2010.
- [50] M. Pastorino and A. Randazzo. Buried Object Detection by an Inexact Newton Method Applied to Nonlinear Inverse Scattering. *International Journal of Microwave Science and Technology*, 2012, 2012.
- [51] Y. Alvarez, J.A. Martinez-Lorenzo, F. Las-Heras, and C.M. Rappaport. An Inverse Fast Multipole Method for Geometry Reconstruction Using Scattered Field Information. *Antennas and Propagation, IEEE Transactions on*, 60(7):3351–3360, 2012.
- [52] P. Rocca, M. Carlin, and A. Massa. Imaging Weak Scatterers by Means of an Innovative Inverse Scattering Technique Based on the Interval Analysis. In *Antennas and Propagation (EUCAP), 2012 6th European Conference on*, pages 1139–1140. IEEE, 2012.
- [53] A.B. Ruffin, J. Decker, L. Sanchez-Palencia, L. Le Hors, J.F. Whitaker, T.B. Norris, and J.V. Rudd. Time Reversal and Object Reconstruction with Single-Cycle Pulses. *Optics letters*, 26(10):681–683, 2001.
- [54] S.I. Kabanikhin. *Inverse and Ill-posed Problems: Theory and Applications*, volume 55. Walter De Gruyter, 2011.

- [55] D. Colton and R. Kress. *Inverse Acoustic and Electromagnetic Scattering Theory*. Springer-Verlag, 1992.
- [56] F. Al-Badour, M. Sunar, and L. Cheded. Vibration Analysis of Rotating Machinery Using Time–Frequency Analysis and Wavelet Techniques. *Mechanical Systems and Signal Processing*, 25(6):2083–2101, 2011.
- [57] W.L. Lai, T. Kind, and H. Wiggenhauser. Using Ground Penetrating Radar and Time–Frequency Analysis to Characterize Construction Materials. *NDT & E International*, 44(1):111–120, 2011.
- [58] G. Kaiser. *A Friendly Guide to Wavelets*. Birkhäuser Boston, 2010.
- [59] H.M. Ozaktas, Z. Zalevsky, and M.A. Kutay. *The Fractional Fourier Transform with Applications in Optics and Signal Processing*. John Wiley & Sons Ltd., Chichester, 2001.
- [60] V. Namias. The Fractional Order Fourier Transform and its Applications to Quantum Mechanics. *J. Inst. Maths Applics*, 25:241–264, 1980.
- [61] A.C. McBride and F.H. Kerr. On Namias’s Fractional Fourier Transform. *IMA Journal of Applied Mathematics*, 39:159–175, 1987.
- [62] F.H. Kerr. Namias’ Fractional Fourier Transforms on L^2 and Applications to Differential Equations. *Journal of Mathematical Analysis and Applications*, 139:404–418, 1987.
- [63] E. Sejdić, I. Djurović, and L. Stanković. Fractional Fourier Transform as a Signal Processing Tool: An Overview of Recent Developments. *Signal Processing*, 91:1351–1369, 2011.

- [64] M. O'Donnell. Coded Excitation System for Improving the Penetration of Real-Time Phased-Array Imaging Systems. *IEEE TUFFC*, 39:341–351, 1992.
- [65] X. Hao R.Y. Chiao. Coded Excitation for Diagnostic Ultrasound: A System Developer's Perspective. *IEEE TUFFC*, 52:160–170, 2005.
- [66] T. X. Misaridis, K. Gammelmark, C. H. Jørgensen, N. Lindberg, A.H. Thomsen, M.H. Pedersen, and J. A. Jensen. Potential of Coded Excitation in Medical Ultrasound Imaging. *Ultrasonics*, 38(1):183–189, 2000.
- [67] L.R. LeBlanc, L. Mayer, M. Rufino, S.G. Schock, and J. King. Marine Sediment Classification Using the Chirp Sonar. *The Journal of the Acoustical Society of America*, 91(1):107–115, 1992.
- [68] Steven G Schock. A Method for Estimating the Physical and Acoustic Properties of the Sea Bed Using Chirp Sonar Data. *Oceanic Engineering, IEEE Journal of*, 29(4):1200–1217, 2004.
- [69] C.E. Cook. Pulse Compression-Key to More Efficient Radar Transmission. *Proceedings of the IRE*, 48(3):310–316, 1960.
- [70] E.C. Farnett and G.H. Stevens. *Radar Handbook*. McGraw-Hill, 1990.
- [71] R. Mulaveesala, J.S. Vaddi, and P. Singh. Pulse Compression Approach to Infrared Nondestructive Characterization. *Review of Scientific Instruments*, 79(9):094901, 2008.

- [72] S. Cong, T. Gang, J. Zhang, and C. Sheng. Parameter Design of Linear Frequency Modulated Excitation Waveform for Ultrasonic Nondestructive Testing of Metallic Materials. *J NDE*, 33(4):684–693, 2014.
- [73] C. Capus, Y. Rzhanov, and L. Linnett. The Analysis of Multiple Linear Chirp Signals. In *IEEE Symposium on Time-Scale and Time-Frequency Analysis and Applications*, pages 1–7. IEEE, 2000.
- [74] M. Bennet, S. McLaughlin, T. Anderson, and N. McDicken. Filtering of Chirped Ultrasound Echo Signals with the Fractional Fourier Transform. *Proceedings of the IEEE Int. UFFC Joint 50th Anniversary Conference*, pages 2036–2040, 2004.
- [75] M. Bennet, S. McLaughlin, T. Anderson, and N. McDicken. The Use of the Fractional Fourier Transform with Coded Excitation in Ultrasound Imaging. *IEEE Trans. BioMed. Eng.*, pages 754–756, 2006.
- [76] A. Akhavan, A. Mahloojifar, and S. Hashemi-Berenjabad. Detection and Separation of Chirp Echoes in Coded Excitation Ultrasound Imaging Using Fractional Fourier Transform. *Proceedings of the 18th Iranian Conference on BioMedical Engineering*, pages 185–190, 2011.
- [77] D. Duxbury, J. Russell, and M. Lowe. The Effect of Variation in Phased Array Element Performance for Non-Destructive Evaluation (NDE). *Ultrasonics*, 53(6):1065–1078, 2013.
- [78] P.D Wilcox, C. Holmes, and B.W. Drinkwater. Advanced Reflector Characterisation with Ultrasonic Phased Arrays in NDE Applications. *IEEE TUFFC*, 54(8):1541–1549, 2007.

- [79] R. Hidalgo-Gato, J.R. Andrés, J.M. López-Higuera, and F.J. Madruga. Quantification by Signal to Noise Ratio of Active Infrared Thermography Data Processing Techniques. *Optics and Photonics Journal*, 3:20, 2013.
- [80] R. Potthast. A Survey on Sampling and Probe Methods for Inverse Problems. *Inverse Problems*, 22(2):R1, 2006.
- [81] E. Kerbrat, C. Prada, D. Cassereau, and M. Fink. Ultrasonic Nondestructive Testing of Scattering Media Using the Decomposition of the Time-Reversal Operator. *TUFFC*, 49(8):1103–1113, 2002.
- [82] A. Aubry and A. Derode. Singular Value Distribution of the Propagation Matrix in Random Scattering Media. *Waves in Random and Complex Media*, 20(3):333–363, 2010.
- [83] A.J. Devaney. Super-resolution Processing of Multi-static Data using Time Reversal and MUSIC. *Inverse Problems*, 15(2):413–429, 1999.
- [84] A. Kirsch. The MUSIC Algorithm and the Factorization Method in Inverse Scattering Theory for Inhomogenous Media. *Inverse Problems*, 18(4):1025–1040, 2002.
- [85] F. Foroozan and S. ShahbazPanahi. MUSIC-based Array Imaging in Multimodal Ultrasonic Non-destructive Testing. In *Sensor Array and Multichannel Signal Processing Workshop (SAM), 2012 IEEE 7th*, pages 529–532. IEEE, 2012.
- [86] L. Bourgeois and E. Luneville. On the Use of Sampling Methods to Identify Cracks in Acoustic Waveguides. *Inverse Problems*, 28(10):105011, 2012.

- [87] N.I. Grinberg. The Operator Factorization Method in Inverse Obstacle Scattering. *Integral Equations Oper. Theory*, 54:333–348, 2006.
- [88] B.B. Guzina, F. Cakoni, and C. Bellis. On the Multi-frequency Obstacle Reconstruction via the Linear Sampling Method. *Inverse Problems*, 26(12):125005, 2010.
- [89] H. Ammari, S. Moskow, and M. S. Vogelius. Boundary Integral Formulae for the Reconstruction of Electric and Electromagnetic Inhomogeneities of Small Volume. *ESAIM: Control, Optimisation and Calculus of Variations*, 9:49–66, 2003.
- [90] H. Ammari and H. Kang. Properties of the Generalized Polarization Tensors. *Multiscale Modeling & Simulation*, 1(2):335–348, 2003.
- [91] H. Ammari. *Mathematical Modeling in Biomedical Imaging*. Springer, 2009.
- [92] P.M. Morse and K.U. Ingard. *Theoretical Acoustics*. Princeton University Press, New Jersey, 1968.
- [93] H. Sato and M. Fehler. *Seismic Wave Propagation and Scattering in the Heterogeneous Earth*. Springer-Verlag, Berlin, 2012.
- [94] L.W. Schmerr. *Fundamentals of Ultrasonic Nondestructive Evaluation: A Modelling Approach*. Plenum Press, New York, 1998.
- [95] J.L. Rose. *Ultrasonic Waves in Solid Media*. Cambridge University Press, Cambridge, 1999.

- [96] J.E. Gubernatis, E. Domany, J.A. Krumhansl, and M. Huberman. The Born Approximation in the Theory of the Scattering of Elastic Waves by Flaws. *Journal of Applied Physics*, 48(7):2812–2819, 1977.
- [97] D.K. Hsu, J.H. Rose, and D.O. Thompson. Reconstruction of Inclusions in Solids Using Ultrasonic Born Inversion. *Journal of applied physics*, 55(1):162–168, 1984.
- [98] J.H. Rose. Elastic Wave Inverse Scattering in Nondestructive Evaluation. In *Scattering and Attenuation of Seismic Waves, Part II*, pages 715–739. Springer, 1989.
- [99] J.W. Hunt, M. Arditi, and F.S. Foster. Ultrasound Transducers for Pulse-Echo Medical Imaging. *IEEE TBME*, BME-30(8):453–481, 1983.
- [100] J.A. Jensen and N.B. Svendsen. Calculation of Pressure Fields from Arbitrarily Shaped, Apodized, and Excited Ultrasound Transducers. *IEEE TUFFC*, 39(2):262–267, 1992.
- [101] A.V. Alejos, M.G. Snchez, I. Cuias, and M. Dawood. *Wideband Noise Radar based in Phase Coded Sequences, Radar Technology*. InTech, 2010.
- [102] C. Hopper, S. Assous, P.B. Wilkinson, D.A. Gunn, P.R. Jackson, J.G. Rees, R.L. O’Leary, and M.A. Lovell. Bioinspired Low-frequency Material Characterisation. *Advances in Acoustics and Vibration*, 2012.
- [103] F.H. Kerr. *Fractional Powers of Integral Transforms for Classical and Generalised Functions*. PhD thesis, The University of Strathclyde, 1988.

- [104] C. Capus and K. Brown. Fractional Fourier Transform of the Gaussian and Fractional Domain Signal Support. *IEEE Proceedings-Vision, Image and Signal Processing*, 150(2):99–106, 2003.
- [105] R. Saxena and K. Singh. Fractional Fourier Transform: A Novel Tool for Signal Processing. *Journal of the Indian Institute of Science*, 85(1):11, 2013.
- [106] E. Barlow. *An Investigation into the Response of a Bubble and an Ultrasound Contrast Agent Under Chirp Excitation*. PhD thesis, The University of Strathclyde, 2009.
- [107] PZFlex Weidlinger Associates Inc. 399 West El Camino Real Mountain View CA 94040-2607.
- [108] G. Harvey, A. Tweedie, C. Carpentier, and P. Reynolds. Finite Element Analysis of Ultrasonic Phased Array Inspections on Anisotropic Welds. In *AIP Conf. Proc.*, volume 1335, pages 827–834, 2010.